Department of Micro- and Nanosciences

Fabrication and characterization of graphene-based electronic devices

Wonjae Kim

Aalto University

DOCTORAL DISSERTATIONS

Aalto University publication series
DOCTORAL DISSERTATIONS 108/2015

Fabrication and characterization of graphene-based electronic devices

Wonjae Kim

A doctoral dissertation completed for the degree of Doctor of Science (Technology) to be defended, with the permission of the Aalto University School of Electrical Engineering, at a public examination held at the Large Seminar Hall of Micronova (Tietotie 3, Espoo) on 28th of August 2015 at 12:00.

Aalto University
School of Electrical Engineering
Department of Micro- and Nanosciences
Nanotechnology group

Supervising professor
Harri Lipsanen

Thesis advisor
Dr. Juha Riikonen

Preliminary examiners
Professor Monica Craciun, University of Exeter, UK
Professor Markus Ahlskog, University of Jyväskylä, Finland

Opponents
Professor Max Lemme, University of Siegen, Germany
Group of Graphene-based Nanotechnology

Aalto University publication series
DOCTORAL DISSERTATIONS 108/2015

ISBN 978-952-60-6317-1 (printed)
ISBN 978-952-60-6318-8 (pdf)
ISSN-L 1799-4934
ISSN 1799-4934 (printed)
ISSN 1799-4942 (pdf)
http://urn.fi/URN:ISBN:978-952-60-6318-8

Unigrafia Oy
Helsinki 2015

Finland

441 697
Printed matter

Aalto University

Abstract

Aalto University, P.O. Box 11000, FI-00076 Aalto www.aalto.fi

Author
Wonjae Kim

Name of the doctoral dissertation
Fabrication and characterization of graphene-based electronic devices

Publisher School of Electrical Engineering

Unit Department of Micro- and Nanosciences

Series Aalto University publication series DOCTORAL DISSERTATIONS 108/2015

Field of research Micro- and nanosciences / Mikro- ja nanotekniikka

Manuscript submitted 23 April 2015 **Date of the defence** 28 August 2015

Permission to publish granted (date) 16 June 2015 **Language** English

☐ **Monograph** ☒ **Article dissertation (summary + original articles)**

Abstract

Graphene, a two-dimensional hexagonal carbon lattice, is a promising material for future electronics. High carrier mobility is viable through the two-dimensional plane and the true atomic thick layer enables to be transparency and flexiblility. The property is unique and never found before in other materials. A sp^2-hybridized bonding in a lattice leads graphene to have physical strength that is about 100 times higher than steel. Its physical property is sustained while graphene is deformed. This is the reason why the graphene has been most attractive for electronics since it discovered in 2004.

In this thesis, several different sources of graphene are introduced and investigated towards device applications. Among the sources ever known, graphene prepared on transition metal by chemical vapor deposition (CVD) is most popular since the method yields a uniform singlelayer without a size limit. For fast and cost-effective synthesis of graphene, photo-thermal CVD (PTCVD) was further developed by investigating the process conditions and parameters, such as, the flow rate of precursor gases, pressure, time, and temperature. Particularly, influence of growth temperature on the graphene quality was further examined. As a result, synthesis of high quality single-layer graphene was achieved on copper at 935-950 °C in about 60 s. The quality of graphene was preliminarily determined by scanning electron microscopy and Raman spectroscopy.

Employing the CVD graphene, field-effect devices were fabricated and characterized at room temperature. With the control of the gate, highly tunable and switchable devices performing as a rectifier and an inverter were demonstrated. Remarkably, the device exhibiting full-wave rectification for 100 kHz of the AC input was presented utilizing three-terminal T-branch junction (TBJ). By applying the same CVD graphene layer to the gate electrode, transparent functionality through the device structure was additionally achieved. The experimental results are comparable to the previously reported TBJs having efficiency of 5-12% as the CVD graphene based TBJs shown here exhibits rectification with efficiency of 18%. As an inverter in the TBJ device, the highest voltage gain was observed to 2.4 at V_D= 4 V. Finally, a cascaded two TBJ device structure where the output of the first TBJ was utilized as a gate input for thesecond TBJ was demonstrated. The output of the cascaded structure was displayed as clear rectification without any external gate. This is a significant step to realize the possibility of layer-by-layer device architecture for graphene-based monolithic integrated circuit, overcoming a zero-bandgap limit.

Keywords graphene, transistor, FET, rectifier, inverter, Raman

ISBN (printed) 978-952-60-6317-1 **ISBN (pdf)** 978-952-60-6318-8

ISSN-L 1799-4934 **ISSN (printed)** 1799-4934 **ISSN (pdf)** 1799-4942

Location of publisher Helsinki **Location of printing** Helsinki **Year** 2015

Pages 155 **urn** http://urn.fi/URN:ISBN:978-952-60-6318-8

Preface

The work presented in this thesis was carried out in the Nanotechnology group of the Department of Micro- and Nanosciences at Aalto University (formerly Helsinki University of Technology). 'Graphene' the main topic of this study was very new when I started in 2008 but becomes now familiar as a most enjoyable material. This was possible thanks to the great help and support of my supervisor and colleagues in the department. Micronova was the excellent place to perform a graphene research: all tools and equipments for the experiment are in a straight line from growth to device analysis. It was a great chance for me working at Micronova. First of all, I would like to express my sincere gratitude to Prof. Harri Lipsanen for the chance and his support with the thoughtful supervision during the study. Dr. Juha Riikonen has given me careful guidance for the academic research and study as an instructor. I sincerely thank him for valuable discussions, suggestions and pieces of advice for my doctoral study to be completed.

The graphene study related to this thesis was initiated as a part of the project collaborating with several other groups in Aalto University, leading by Nokia Research Center. It was the very valuable time for me to learn 'graphene'. I thank Dr. Pirjo Pasanen for giving me motivation for the study of 'nonlinear behavior' on graphene. I also want to thank Prof. Pertti Hakonen for fruitful discussions about the TTJ/TBJ device operations.

CVD graphene on copper was achieved by photo-thermal CVD in 2011. I thank Dr. Sanna Arpiainen at VTT for helping me to develop the CVD process and sharing many ideas related to graphene technology. I thank Olli Svensk for his support with handling the RTP when developing the process. Changfeng Li was one of the key supporters by operating the RTP reactor to produce graphene. Many thanks for his many contributions to this work. For SiC graphene, Dr. Sergey Novikov provided me many samples with meaningful discussions. I thank him and his former student Erkki Vesapuisto for the work. I thank Dr. Pekka Kuivalainen, a former professor of the Electron Physics group, for fruitful theoretical discussions about the device operation. A pre-examination of the as-grown graphene surface before device fabrication

was demanded. I also thank Dr. Antti Säynätjoki and Dr. Lasse Karvonen for AFM and multi-photon analysis of the graphene layer.

Field-effect transistor was the main frame of this study. A critical point in device architecture was the dielectric layer. I especially want to thank Dr. Alexander Perros for giving me inspiration for deposition of the dielectric alumina layer on graphene. I had the pleasure to share ideas and have discussions with him in the same office. I also thank Maria Berdova for sharing knowledge and enjoyable collaboration for the study of a graphene-alumina membrane.

Device fabrication in cleanroom was a key task for this study. All those working at Micronova Aalto nanofab are gratefully thanked for their help for the device fabrication. I want to extend my gratitude to Dr. Matthias Meschke, Dr. Tommy Holmqvist, Antti Peltonen, Dr. Victor Ovchinnikov, Dr. Nikolai Chekurov, and Pasi Kostamo. I also thank Paula Heikkilä and Paula Kettula for a great support for the cleanroom work.

Analysis and characterization of the devices were the most significant step to understand the role of graphene. Many thanks to Pasi Kostamo and Dr. Nikolai Chekurov for guiding me DC and AC analysis for the devices. I also want to thank Johanna Anteroinen, Dr. Kari Stadius, and Prof. Jussi Ryynänen of the Circuit Design group for close collaboration for several years, giving me inspiration for the RF device operation.

I also wish to thank all of our graphene team members, Susoma Janatul, Joonas Mäkinen, Maria Grigoreva, and Petri Mustonen, for their supports and joyful work collaborations.

Finally, I want to extend my gratitude to those of the Korean community in Finland, my best neighbors Myungsik Seo, Kanghun Lee, Byungjin Cho, Choo Paul, Jeahyuk Choi, Donguk Lee, and Dr. Younghun Kim, the best debater Dr. Kyunghyun Cho and Sungin Cho, the considerate young giants Sol beak, Daeun Kim, and Sunjin Hwang, especially, Prof. Jungjoo Lee, Seyoung Kim, Yeona Hong, and all other KOSAFI and KOSES members for sharing emotions and culture. Heedo Lee, Byungkuk Na, Inje Oh, and all members of our team BOARS are especially thanked for the memorable baseball games. I also thank Dr. Hyunjin Kim for an emotional support at the beginning.

Lastly, I wish to thank my mother J. Suh and brothers and sister Myeongok, Byungha, Byunggyu, Byungmin for their support and love.

Espoo, 11 August 2015

Wonjae Kim

Contents

List of Abbreviations

AES	Auger electron spectroscopy
AFM	atomic force microscope
ALD	atomic layer deposition
Al_2O_3	aluminum oxide
BLG	bilayer graphene
BP	band pass
BZ	Brillouin zone
CNP	charge neutrality point
CVD	chemical vapor deposition
DOS	density of state
DR	double resonance
EG	exfoliated graphene
EPG	epitaxial graphene
FET	field-effect transistor
FWHM	full-width at half maximum
GFET	graphene field-effect transistor
GND	ground
IC	integrated circuit
ITO	indium tin oxide
iTA	in-plane transverse acoustic phonon
iTO	in-plane transverse optical phonon
LA	longitudinal acoustic phonon

LO	longitudinal optical phonon
ML	multilayer
MPM	multi-photon microscope
PMMA	poly-methyl methacrylate
PTCVD	photo-thermal chemical vapor deposition
RGB	red, green, blue
RTP	rapid thermal processing
SEM	scanning electron microscope
SHG	second-harmonic generation
SiC	silicon carbide
Si_3N_4	silicon nitride
SiO_2	silicon dioxide
SLG	single-layer graphene
TBJ	three-terminal branch junction
TEM	transmission electron microscope
THG	third-harmonic generation
TLM	transfer length method
TR	triple resonance
TTJ	three-terminal junction
2-DEG	two-dimensional electron gas

List of Symbols

A	voltage gain
a	lattice constant
c	speed of light
d	contact space in 2-probe (channel length)
E(k)	electron energy dispersion
E_F	Fermi energy
E_{ph}	scattering phonon energy
E_1	incident photon energy
E_2	scattering photon energy
e	electron charge
h	Planck constant
$\hbar$	reduced Planck constant
$\mathbf{k}$	electron wave vector
L_T	transfer length
l	mean free path
l_m	effective coupling length
n	carrier concentration
n_{ind}	induced carrier concentration
n_o	intrinsic carrier concentration
P	transmission probability
$\mathbf{q}$	phonon wave vector
R_C	contact resistance

R_{CC}	contact resistance of center terminal
R_{CL}	contact resistance of left terminal
R_{CR}	contact resistance of right terminal
R_{gC}	resistance of center channel
R_{gL}	resistance of left channel
R_{gR}	resistance of right channel
R_{sh}	sheet resistance
R_{total}	total resistance
r	switching parameter
T	temperature
t	thickness
V	electro-chemical potential originated by external electric field
V_{BG}	backgate voltage
V_C	voltage at the center branch
V_{DD}	power supply voltage for inverter operation
V_{Dirac}	gate voltage at the Dirac point
V_{DS}	potential difference between drain to source
$V_{eff,L}$	effective gate voltage for the left terminal
$V_{eff,R}$	effective gate voltage for the right terminal
V_G	gate voltage
V_{GS}	potential difference between gate to source
V_{IN}	input voltage
V_{OUT}	output voltage
V_{TG}	topgate voltage
V_o	input voltage in push-pull application
v_F	Fermi velocity
W_G	work function of graphene
W	channel width
Z	width of metal contact

γ	hopping energy
ΔE_{FM}	Fermi energy shift of graphene by metal contact
ΔV	potential step at metal-graphene contact
δ	distance of carbon-carbon atom
ε_o	permittivity of free space
ε_r	permittivity of medium
η	metal-graphene coupling length
λ	wave length of light
μ	carrier mobility
ν	frequency
ρ	resistivity
ρ_C	contact resistivity
σ	conductivity
τ	mean free time

List of Publications

This doctoral dissertation consists of a summary and of the following publications which are referred to in the text by their numerals

1. Kim, Wonjae; Li, Changfeng; Chekurov, Nikolai; Arpiainen, Sanna; Akinwande, Deji; Lipsanen, Harri; Riikonen, Juha. 2015. All-Graphene Three-Terminal Junction Field-Effect Devices as Rectifier and Inverter. American Chemical Society. **ACS Nano,** volume 9, issue 6, pages 5666-5674. DOI: 10.1021/nn507199n

2. Kim, Wonjae; Riikonen, Juha; Li, Changfeng; Chen, Ya; Lipsanen, Harri. 2013. Highly tunable local gate controlled complementary graphene device performing as inverter and voltage controlled resistor. IOP Publishing. **Nanotechnology**, volume 24, issue 39, pages 395202-1-5. DOI:10.1088/0957 -4484/24/39/395202.

3. Kim, Wonjae; Pasanen, Pirjo; Riikonen, Juha; Lipsanen, Harri. 2012. Nonlinear behavior of three-terminal graphene junctions at room temperature. IOP Publishing. **Nanotechnology**, volume 23, issue 11, pages 115201-1-6. DOI:10.1088/0957-4484/23/11/115201.

4. Riikonen, Juha; Kim, Wonjae; Li, Changfeng; Olli Svensk; Arpiainen, Sanna; Kainlauri, Markku; Lipsanen, Harri. 2013. Photo-thermal chemical vapor deposition of graphene on copper. Pergamon. **Carbon**, volume 62, pages 43-50. DOI:10.1016/j.carbon.2013.05.050.

5. Berdova, Maria; Perros, P. Alexander; Kim, Wonjae; Riikonen, Juha; Ylitalo, Tuomo; Heino, Jouni; Li, Changfeng; Kassamakov, Ivan; Hæggström, Edward; Lipsanen, Harri; Franssila, Sami. 2014. Exceptionally strong and robust millimeter-scale graphene-alumina composite membrane. IOP Publish-

ing. **Nanotechnology**, volume 25, issue 35, pages 355701-1-7. DOI:10.1088/0957-4484/25/35/355701.

6. Säynätjoki, Antti; Karvonen, Lasse; Riikonen, Juha; Kim, Wonjae; Mehravar, Soroush; Norwood, A. Robert; Peyghambarian, Nasser; Lipsanen, Harri; Kieu, Khanh. 2013. Rapid large-area multi-photon microscopy for characterization of graphene. American Chemical Society. IOP Publishing. **ACS Nano**, volume 7, issue 10, pages 8441-8446. DOI: 10.1021/nn404290.

7. Vesapuisto, Erkki; Kim, Wonjae; Novikov, Sergey; Lipsanen, Harri; Kuivalainen, Pekka. 2011. Growth temperature dependence of the electrical and structural properties of epitaxial graphene on SiC(0001). WILEY-VCH Verlag. **physica status solidi (b)**, volume 248, issue 8, pages 1908-1914. DOI: 10.1002/pssb.201046368.

Author's Contribution

Publication 1: All-Graphene Three-Terminal Junction Field-Effect Devices as Rectifier and Inverter

The author organized the manuscript, designed experiment, and fabricated devices. In experiment, the author performed Raman spectroscope for graphene film characterization, measured devices, and characterized device operations.

Publication 2: Highly tunable local gate controlled complementary graphene device performing as inverter and voltage controlled resistor

The author organized the manuscript, designed experiment, and fabricated devices. In experiment, the author measured devices and characterized inverter operations.

Publication 3: Nonlinear behavior of three-terminal graphene junctions at room temperature

The author organized the manuscript, designed experiment, and fabricated devices. In experiment, the author prepared the graphene samples by mechanical exfoliation, measured devices, and characterized device operations.

Publication 4: Photo-thermal chemical vapor deposition of graphene on copper

The author contributed to write the manuscript, designed experiment, and fabricated TLM structures. The author developed the PTCVD process for graphene growth on the copper foil. In experiment, the author performed Raman for graphene characterization and analyzed the mapping data. The author measured TLM/FET structures and extracted parameters.

Publication 5: Exceptionally strong and robust millimeter-scale graphene-alumina composite membrane

The author prepared graphene onto the alumina membrane by transferring from the copper foil. In experiment, the author performed Raman spectroscope for

graphene film characterization. The author contributed to manuscript finalization.

Publication 6: Rapid large-area multi-photon microscopy for characterization of graphene

The author prepared the graphene samples by mechanical exfoliation and performed Raman spectroscope for graphene layer identification. The author contributed to manuscript finalization.

Publication 7: Growth temperature dependence of the electrical and structural properties of epitaxial graphene on SiC(0001)

The author performed Raman spectroscope to confirm existence of graphene as a reference for AES measurement.

1. Introduction

Since its discovery in 2004 [1], graphene, a two-dimensional (2D) hexagonal lattice, has drawn enormous attention due to its extraordinary physical properties. Electrons propagating in honeycomb lattice of graphene lose their effective mass through interaction with the periodic potential of the lattice and, consequently, behave like massless Dirac fermions. The massless quasi-particles move with the speed of ~ 10^6 m/s which is the *Fermi velocity* V_F. Electron waves confined in the 2D plane experience less scattering, which enables electrons to travel with a longer mean-free path. As a result of massless carrier and suppressed scattering, carrier mobility in graphene can rise up to 10^5 cm^2/Vs at room temperature [2]. The exceptional property is attractive for applications in high-speed electronic devices.

Due to the atomic thick crystal, graphene is presented as a transparent plane where transmittance reaches ~98% in visible light [3]. In addition, a tight sp^2-hybridized bonding of carbon atoms in graphene yields the most robust structure [4]. Graphene has a physical strength that is about 100 times higher than steel [5] and retains its unique properties while it is deformed or folded [6]. This is further useful for the applications in functional micromechanical systems as well as transparent-flexible electronics.

In carbon-based electronic devices, graphene field-effect transistors (GFETs) [7] are among the most investigated structures. Recently, the state-of-the-art GFET structures have surpassed the gigahertz limit not only on conventional rigid substrates like Si [8] but even on flexible substrates [9], [10]. However, the GFET performance as a logic device is undermined due to a nature of the zero bandgap in graphene. Nevertheless, graphene is an intriguing material for a component in integrated circuits (ICs) since it can be easily doped by chemicals [11] or an external electric field [12], [13]. With the electrostatic doping, the charge carrier type can even be switched to p- or n-type and, consequently, graphene can be applied in various tunable devices. Exploiting the behavior, a gra-

phene device performing as an inverter [14]–[23] or a voltage-controlled resistor based on CMOS technology has been recently demonstrated.

Regardless of the bandgap limit, graphene is also spotlighted as a material for two-dimensional electron gas (2-DEG) owing to its feature of the conducting 2D crystal. Charge carrier transport in a 2-DEG is interested due to the possible nonlinear behavior [24]–[35] which typically arises in the 2D ballistic regime. This is a notable phenomenon because it displays as an electrical rectification. Recently, the nonlinearities on graphene have been demonstrated [36]–[41]. The studies have confirmed that graphene has an ability to perform as the 2-DEG rectifying device. The rectification is contributed to the conductance difference along the channel when two terminals, *i.e.* source and drain, are biased anti-symmetrically. Therefore, three-terminal structure which are typically fabricated through the T-branch junction (TBJ) is widely utilized for the rectifying device because the signal of rectification can be conveniently obtained at the center terminal. The level of the rectification relies on the carrier type and density: a positive output is typically observed in hole region and a negative output in the electron region and the stronger rectification arises with higher carrier mobility. The behavior enables graphene to be applied for a tunable or switchable rectifier. This is a significant difference from the conventional III-V semiconductor based TBJ devices [29]–[32] showing only negative rectifications as they have only electrons as a major charge carrier. So far, the TBJs have been fabricated in nanoscale (channel width ~50-300 nm) to utilize the ballistic effect. However, the large scale device should be considered for practical applications to be free from the strict ballistic limit in a size. Thanks to recent technology development for large scale synthesis, the graphene-based monolithic ICs in a wafer is to be viable. Therefore, it is worth to investigate the FET or TBJ devices fabricated utilizing large scale graphene which is available, for example, through chemical vapor deposition (CVD) [42]–[44].

This study examines the characteristics of graphene-based field-effect devices which specifically play as a rectifier and an inverter. For practical use, all devices fabricated are characterized at room temperature. In this thesis, after reviewing fundamental graphene properties in Chapter 2, the methods for preparation and synthesis of graphene are presented in Chapter 3. A growth of graphene on transition metal by CVD is intensively focused in the review. Chapter 4 introduces tools and techniques for graphene layer characterization, including the evaluation methods. Among the techniques, Raman spectroscopy is overviewed in detail. The experimental results of the graphene growth on the copper foil accomplished by photo-thermal CVD are presented in Chapter 5. Afterward, characteristics of the devices fabricated utilizing the CVD graphene

are finally presented in Chapter 6. The summary of this study and outlook for graphene technology are followed in Chapter 7.

2. Electrical properties of graphene

In history the concept of graphene has been well understood [45]–[47] but real 2-dimensional status had not been expected to exist for the past 70 years due to thermodynamically unstable atomic configuration in ambient condition. During the period, on the other hand, carbon nanostructures were discovered, which attracted great attention as 0- to 2-dimensional structures were realized. The 0-dimensional allotrope of C_{60} [48], known as a fullerene, brought new insight to understand allotrope structures since some hexagonal chains could be replaced by pentagons, which finally forms a carbon sphere resembling a football. A 1-dimensional architecture as a tubular carbon structure which is an exactly graphene sheet rolled up, the so-called *carbon nanotube*, was reported in 1991 by Sumio Iijima [49]. This sparked the studies regarding device physics [50] because it was the first observed perfect crystal independent from the bulk graphite. The fundamental studies have continuously boosted the research for graphene up since physical properties between two materials are almost identical [51]. The studies have confirmed that the carbon atoms are configured to the hexagonal honeycomb lattice formed by a sp^2-hybridized atomic bond, where electrons behave as massless Dirac fermions, which never happens in the 3-dimensional space.

In this chapter, electrical properties of graphene are overviewed. By reviewing electronic band structure, unique property of graphene including ambipolar behavior in field-effect region is presented. In addition, potential applications for electronics or functional devices are discussed in brief.

2.1 Background of graphene

Carbon forms many different structures maintaining the same physical state, which are the so-called *allotropes*. The allotropes of carbon include diamond, graphite (graphene), fullerenes, and nanotubes. Graphite (shown in Figure 1(a))

is the most well-known carbon allotrope, which was discovered in a mine in the 16th century. Due to its softness and dark color, the graphite was popular to use for drawing or marking for a notice. Therefore, it was named to "graphite" whose term was originated from the Greek word "graphein" meaning to draw or write. The graphite is utilized, for example, to a core of pencil mixing with a clay and is composed with the stack of an individual atomic layer as shown in Figure 1(b). An individual atomic layer is called *graphene*. Atoms in graphene are bonded covalently while each of the layers is connected by the van der Waals interaction, meaning that interlayer bonding is much weaker than interatomic bonding. The distance of inter layer is roughly 0.34 nm. Therefore, when the graphite is scratched, for example, over the paper, a stack of graphene sheets are exfoliated from the bulk graphite and stick to the target surface.

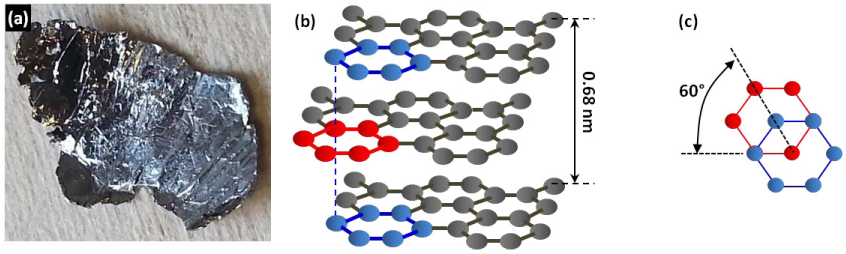

Figure 1. (a) Optical image of natural graphite. (b) Schematic of ABA stacked graphite and (c) twisting angle of AB stacked graphite: the atoms in the upper and lower layers are denoted by the blue and red color, respectively.

In natural graphite, the graphene layers are stacked with misorientation of 60° as seen in Figure (b) and (c), which is called *AB* or *Bernal* stacking. The AB stacking crystal is the most often structure in a nature [52]. In the case of turbostratic graphite, a stacking configuration is random, which makes the electrical property different from the AB stacking. The stacking configuration plays a significant role determining electronic band structure in bilayer (or trilayer) graphene. For example, the AB stacked bilayer has a unique parabolic band structure (to be discussed in the section 2.2) while the turbostratic bilayer is considered as a composition of two individual single-layers which may have a linear band structure.

2.2 Electronic structure

In the atomic ground state, carbon has 6 electrons configured as $1s^2$, $2s^2$ and $2p^2$, where 2 electrons fill the inner shell and 4 electrons occupy the outer shell of 2*s* and 2*p* ($2p_x$, $2p_y$, $2p_z$) orbitals. However, when other neighboring carbon

atoms are placed together, it is favorable to excite one electron from the 2*s* to the 2*p* (2p_z) orbital to form covalent bonds with the other atoms. In this excited state, there are four equivalent quantum-mechanical states, $|2s\rangle$, $|2p_x\rangle$, $|2p_y\rangle$, and $|2p_z\rangle$ in orbitals. A superposition of $|2s\rangle$ with $n|2p_j\rangle$ states is defined as sp^n hybridization. Graphitic materials such as carbon nanotubes and graphene are well known for sp^2 hybridization: 2*s* is superposed with two 2p orbitals (2p_x and 2p_y) and they are oriented in the *xy*-plane with mutual 120° angles. This results in each atom to have a strong covalent bond with the nearest three atoms (σ-bond), eventually forming hexagonal lattice through the *xy*-plane. Carbon-carbon bond length (=lattice constant *a*) is estimated to be 1.42 Å [53]. The remaining unhybridized 2p_z orbital is perpendicular to the plane (π-electron). Thus, there are six σ-bonds and three π-bonds in an atom with three neighbors in graphene. The electron associated to π-bond determines the electronic properties of graphene at low energy as the π electrons are much closer to the Fermi surface than σ electrons. Hence, the energy dispersion of π electrons is only considered here for electronic band structure of graphene.

The hexagonal honeycomb lattice can be expressed with two sub lattices, the so-called *triangular Bravais lattices* [54] with a basis of two atoms per unit cell, as seen in Figure 2(a). In *x*, *y* coordinate system, the unit cell vectors, $\mathbf{a}_1$ and $\mathbf{a}_2$, are expressed as

$$\mathbf{a}_1 = \left(\frac{3}{2}a,\ \frac{\sqrt{3}}{2}a\right),\ \mathbf{a}_2 = \left(\frac{3}{2}a, -\frac{\sqrt{3}}{2}a\right) \tag{2.1}$$

where *a* is the lattice constant (inter-atom distance).

The corresponding reciprocal lattice vectors shown in Figure 2(b), $\mathbf{b}_1$ and $\mathbf{b}_2$, which are rotated by 30° from the vectors of $\mathbf{a}_1$ and $\mathbf{a}_2$ are also given by

$$\mathbf{b}_1 = \left(\frac{2\pi}{3a},\ \frac{2\pi\sqrt{3}}{3a}\right),\ \mathbf{b}_2 = \left(\frac{2\pi}{3a}, -\frac{2\pi\sqrt{3}}{3a}\right) \tag{2.2}$$

The first Brillouin zone (BZ) for the honeycomb lattice with its center *Γ* and the two inequivalent corners *K* and *K'* (which are called the Dirac points) is shown in Figure 2(b). The two points are given by

$$K = \left(\frac{2\pi}{3a},\ \frac{2\pi}{3\sqrt{3}a}\right),\ K' = \left(\frac{2\pi}{3a}, -\frac{2\pi}{3\sqrt{3}a}\right) \tag{2.3}$$

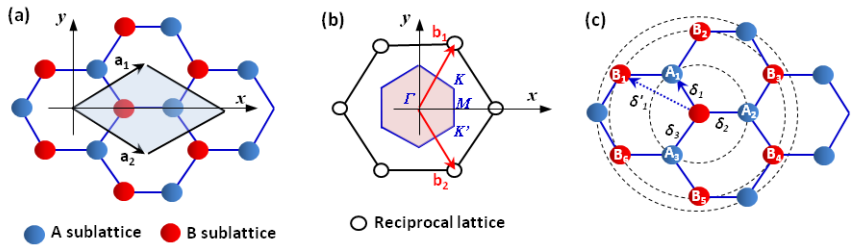

Figure 2. (a) Schematic of hexagonal lattice of graphene. The unit cell is expressed by two sublattices (A and B). $\mathbf{a_1}$ and $\mathbf{a_2}$ are the unit vectors. (b) Reciprocal lattice with Brillouin zone (BZ). $\mathbf{b_1}$ and $\mathbf{b_2}$ are the reciprocal vectors. (c) The first- ($\mathbf{A_1}$ - $\mathbf{A_3}$), second- ($\mathbf{B_1}$-$\mathbf{B_6}$), and third-nearest atoms are indicated by the dotted circles. $\boldsymbol{\delta_i}$ (= a) and $\boldsymbol{\delta'_i}$ denote the distance for the first- and second-nearest atoms, respectively.

The vectors for three nearest-neighbor atoms (A_1 - A_3 atoms in Figure 2(c)) are expressed

$$\delta_1 = \left(\frac{1}{2}a, \frac{\sqrt{3}}{2}a\right),\ \delta_2 = (a, 0),\ \delta_3 = \left(\frac{1}{2}a, -\frac{\sqrt{3}}{2}a\right) \tag{2.4}$$

While the six second-nearest neighbors are equivalent to the vectors for the unit cell as

$$\delta'_i = \pm a_i \tag{2.5}$$

The electronic state can be estimated with zone folding approximation. This approximation can be obtained from a tight binding calculation with considering only the energy dispersion of π electrons [45], [54], [55]. The energy dispersion for the triangle with vertices, Γ, K and M shown in Figure 2(b), can be expressed using tight binding model [45], [56]–[58], by considering the nearest (γ_0) and the next nearest hopping energy (γ_1) [59] as

$$E^{\pm}(k) = \pm\gamma_0\sqrt{3 + f(k)} - \gamma_1 f(k) \tag{2.6}$$

$$f(k) = 4cos\left(\frac{\sqrt{3}k_y a}{2}\right)cos\left(\frac{3k_x a}{2}\right) + 2cos\left(\sqrt{3}k_y a\right) \tag{2.7}$$

where k is the wave vector and a the lattice constant (≈ 1.42 Å). E^+ and E^- correspond to the conduction (π*) and valence (π) energy bands.

Due to the second-nearest hopping energy (with finite values of γ_1), the electron-hole symmetry is broken in high energy regime and, consequently, π and π* bands becomes asymmetric [56]. However, the hopping energy γ_0 is more significant ($\gamma_0 >> \gamma_1$), thus, the model in Equation (2.6) can be simplified by ignoring

γ_1 and the spectrum becomes symmetric by the zero energy as shown in Figure 3. Here, γ_0 = 2.7 eV is applied [56], [59].

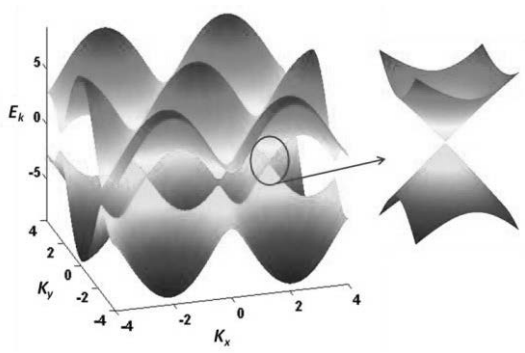

Figure 3. Energy spectrum in BZ derived from Equation (2.6). (right inset) E(k) spectrum in low energy band showing conical linear dispersion at *K* (or *K'*) point.

The dispersion in low energy exhibits as linear structure with the valence and conduction band touching at *K* or *K'* point in BZ, showing a zero bandgap in energy dispersion. The linear dispersion in low energy can be further described by expanding the full band structure of Equation (2.7) close to *K* (or *K'*) vector given in Equation (2.3) for $k = K+q$ ($|q|<<|K|$) [59], [60] by

$$E^{\pm}(q) \approx \pm\hbar v_F|q| + O(q/k)^2 \qquad (2.8)$$

where q is the 2D wave vector of the Dirac point (momentum measured relatively to the Dirac point) and v_F (~c/300 = 1×10^6 m/s) the Fermi velocity.
Incidentally, the linear energy dispersion in Equation (2.8) resembles that of ultra-relativistic particles behaving as massless Dirac fermions which travel with the speed of v_F. Thus, the point of *K* or *K'* in BZ is called the *Dirac point*. This indicates that the interaction of electrons with the periodic potential of graphene's honeycomb lattice gives rise to new massless charge-carrying quasi-particles [61]. This relativistic process particularly also relates to a chiral tunneling where an incoming electron penetrates through a potential barrier (in case its height is larger than electron's kinetic energy). In the process, the transmission probability *P* weakly depends on the barrier height, the so-called *Klein paradox* or *Klein tunneling,* in stark contrast to the conventional non-relativistic tunneling where the *P* exponentially decays with increasing the barrier height. For an electron in diffusive conductor, *P* through the system depends strongly on the distribution of scatters while for massless Dirac fermions *P* is constant but depends on the carrier incident angle [62].

Bilayer graphene (BLG), AB stacked two graphene layers, has a totally different electronic structure from single-layer graphene. Due to two single-layers weakly coupled by electron hopping between the layers, the electronic structure of the bilayer in low energy is described [59], [60] by

$$E^{\pm}(q) = \sqrt{V^2 + \hbar v_F^2 q^2 + \frac{\gamma_\perp^2}{2} \pm \left(4V^2\hbar^2 v_F^2 q^2 + \gamma_\perp^2 \hbar^2 v_F^2 q^2 + \frac{\gamma_\perp^4}{4}\right)^{\frac{1}{2}}} \quad (2.9)$$

where V is the shift in inter-layer electro-chemical potential originated from the external electric field and $\gamma_\perp$(≈ 0.4 eV) the effective interlayer hopping energy.

From the relation in Eq. (2.9), i) for V≠ 0, the BLG has a certain bandgap of Δ= $2V$-($4V^3/\gamma_\perp^2$) at q= $\sqrt{2}V/(\hbar v_F)$ and ii) for V=0, the BLG is a gapless semiconductor with a parabolic dispersion relation [60] as

$$E^{\pm}(q) \approx \hbar^2 \frac{v_F^2 q^2}{\gamma_\perp} = \hbar^2 q^2/(2m) \quad (2.10)$$

where $m = \gamma_\perp/(2v_F^2)$ for small q satisfying $\hbar v_F q \ll \gamma_\perp$.

For high values of q ($\hbar v_F q > \gamma_\perp$), corresponding to the carrier densities larger than 5×10^{12} cm^{-2} [60], a linear dispersion relation $E^{\pm}(q) \approx \hbar v_F q$is exhibited, identical to that of the single layer. Therefore, graphitic system becomes gradually metallic with increasing the number of layers.

2.3 Ambipolar field effect in graphene

A distinguished feature for graphene is a gapless semiconducting (or semimetallic) nature where the only electron or hole carriers are presented. In a 2D system of graphene, the Fermi energy can be modulated by employing an external electric-field, which allows controlling charge carrier concentration as well as switching a type of the carriers crossing over the Dirac point. By applying the gate voltage (V_G), the carrier concentration (n) in graphene can be determined by the classical capacitor model as

$$C = \frac{Q}{V_G} = \frac{\varepsilon_0 \varepsilon_r A}{t} \quad (2.11)$$

$$n \approx \frac{\varepsilon_0 \varepsilon_r V_G}{te} = \alpha V_G \quad (2.12)$$

where C is the capacity, Q (= enA) the capacitor charge, A the area, ε_o and ε_r the permittivity of free space and insulator, respectively, t the thickness of insulator, e the electron charge, and α the coefficient.

A schematic of graphene with a gate is shown in Figure 4(a), which corresponds to the concept of GFET.

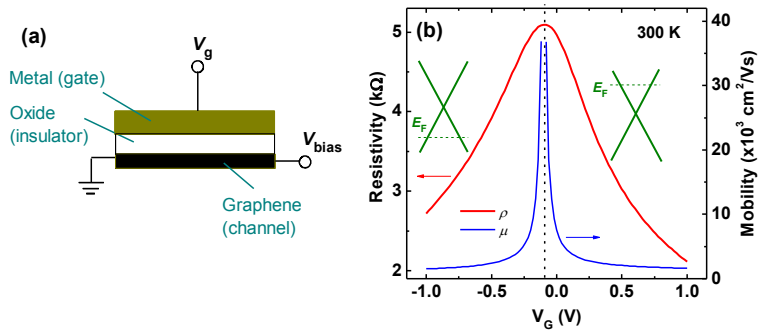

Figure 4. (a) Schematic of the GFET. (b) Resistivity (ρ, red curve) as a function of the gate voltage (V_G) observed at 300 K and mobility (μ, blue curve) calculated by applying the coefficient $\alpha = 1.7\times10^{12}$ cm^{-2}/V and a dielectric thickness t = 30 nm. The insets denote low-energy spectrum $E(k)$ with the Fermi level at a certain region of V_G.

Figure 4(b) shows resistivity (ρ, red curve) as a function of V_G observed at 300 K when the channel bias (V_{bias}) is applied to the graphene channel, where the 30 nm of aluminum oxide (Al_2O_3) is placed in between graphene and metal. This observation shows that the positive (negative) gate voltage leads to accumulation of electrons (holes) in graphene, resulting in lowering ρ by increasing n in electrons or holes: *ambipolar* behavior. With the gate the E_F level is up-shifted or down-shifted over the Dirac point. The insets of Figure 4(b) show its conical low-energy spectrum $E(k)$ with the position of E_F corresponding to the region of the gate voltage. This also implies the fact that carriers are vanished when the E_F is positioned precisely at the Dirac point at T = 0 K, *i.e.* electrons completely occupy the valence band while states in the conduction band are empty. This indicates that electrons and holes are degenerate at the Dirac point (E_F = 0) in which, eventually, the conductivity (σ) of graphene is expected to be nearly zero. However, the actual results show a finite minimum conductivity of the order of ~$4e^2/h$ at the Dirac point even at low temperature [1], [2]. This is because the carriers in graphene are significantly affected by long-range Coulomb scattering and surface charged impurities, which results in creating a finite density of state (DOS) and, hence, a finite charge carrier density even at the Dirac point [59], [60], [63]. This is the so-called *intrinsic carrier concentration* (n_o) and affects electrical properties of graphene. Therefore, in pristine graphene (typically n_o~

10^{11} cm^{-2}) extremely high mobility (μ) can be observed, exceeding ~10^4 cm^2/Vs even at ambient condition [1], [2]. The μ is related to the carrier concentration as $\mu = \sigma/ne$ and, thus, can be expressed from Equation (2.12). Figure 4(b) presents the μ (blue curve) as function of V_G, corresponding to the curve of ρ, when ignoring n_o and contact resistance. Here, $A = 4 \times 28$ μm^2, $\varepsilon_o = 8.854 \times 10^{-12}$ F/m and $\varepsilon_r = 9.34$ for Al_2O_3, $t = 30$ nm, and $e = 1.602 \times 10^{-19}$ C are applied. Thus, α is ~1.7×10^{12} cm^{-2}/V. It clarifies that the μ can reach over 10^4 cm^2/Vs at 300 K. When the more impurities are associated to the graphene surface, resulting in the n_o increased not to be negligible, the μ will be significantly decreased since the n is determined as $n = (n_o^2 + n_{ind}^2)^{1/2}$, where n_{ind} is the carrier density induced by the gate, which is determined by the Equation (2.12). Thus, the μ can be further improved even up to ~10^5 cm^2/Vs when the extremely clean surface of graphene is preserved. This enables electrons in graphene to travel with the submicrometer mean free path in graphene [2].

2.4 Potential applications

High mobility in III-V compound semiconductors is observed only in nearly undoped condition or very low carrier concentration while in graphene it remains even at high carrier concentration. Moreover, mobility is theoretically almost independent from temperature in graphene [2], indicating that the ballistic-oriented-transport may be possible even on submicrometer scale at 300 K. This is the most distinguished difference from conventional semiconductors. The high carrier mobility, for instance, reduces the response time in switching, which is desired for the device operating at high frequency. As a consequent, graphene transistors performing at few hundred GHz have been demonstrated [64], [65]. The zero bandgap limit degrading transistor switching capability may be compromised with applying the ultra-thin dielectric layer [21] as well as hetero-structure of graphene-semiconductor [66]–[71].

In addition to a role as an active component, graphene is the most promising for a transparent conductive electrode which is essentially required in the display. Indium tin oxide (ITO) is a widely adopted material for a transparent electrode nowadays. However, indium is relatively rare with its abundance in the earth and, thus, its material cost can be high. With respect to optoelectronics, graphene, eventually, can be a powerful source to replace ITO since it is efficiently synthesized through very simple process. Single-layer graphene is a substance having ~97% of transmittance in visible light [3] and has the sheet resistance as low as 70-80 Ω/sq [72], [73] which is close to the demanding level

of industry as ITO exhibits (~50 Ω/sq). Moreover, graphene is a strong candidate for flexible electronic devices due to its strongest and most elastic nature ever found. Graphene sustains conducting property while its layer is deformed or folded [6] although the conductivity is slightly varied.

The conductance sensitivity for the morphological deformation can be further exploited for a mechanical sensors [4], [74] or microphone/speakers [75]. So far, a relatively small window of graphene membrane has been presented due to its difficulties in realization of the large-scale suspended membrane. When the graphene is supported with an extra reinforced material, for example, a thin Al_2O_3, the window can scale up to millimeter size which will dramatically enhance the sensitivity in conductance difference (this is discussed more in Chapter 4). Multilayer graphene is also interested for other functioning applications, for example, a wearable device which requires a flexible-robust conducting material.

In particular, graphene based biosensors detecting such biomolecules, proteins, or DNA are emerging for promising future biotechnology applications [76]. The easy doping with biomaterials enables to increase sensor capability.

3. Preparation and synthesis of graphene

As characteristics of the electronic device fabricated on graphene is strongly dependent on its surface condition, preparation of the high quality layer is most important. For example, carrier mobility is sensitive to the defects or impurities on the surface of graphene. A highly crystallized grain with minimized structural defects as well as a clean surface without contaminations are favorably desired for the best device performance. Hence, a proper method for preparation of graphene should be selected for the purpose. There are three different methods widely used: i) mechanical exfoliation by an adhesive tape, ii) epitaxial growth on silicon carbide (SiC) by thermal decomposition, and iii) growth on transition metal by chemical vapor deposition. Although all prepared by different methods have a similar feature of sp^2 hybridized hexagonal lattice, their physical properties are not exactly identical. In this chapter, the three different methods are presented and compared. Particularly, mechanisms for the epitaxial growth on silicon carbide and for the growth on transition metal by chemical vapor deposition are reviewed in more detail.

3.1 Exfoliated graphene (EG)

The bonding energy of interlayer in graphite is about 0.4 eV which is much lower than that of interatoms, 2.7~2.9 eV [59], [60]. This weak interlayer bonding enables an individual layer to be peeled off from the bulk graphite by an adhesive medium [1], *e.g*. *Scotch* tape. The layer which is mechanically exfoliated is typically referred as *exfoliated graphene* (EG). It is pristine when the ambient contaminations and some from the tape are ignored since the bulk graphite is naturally composed with crystallized grains. Typically, devices fabricated on EG shows better performance with higher mobility than those on other graphene sources. EG is obtained in the simple process but it has a size limit by few tens of (or a hundred) micrometers. Therefore, EG is popular for a reference

when characterizing other graphene sources, playing a role as a fundamental standard graphene. Figure 5 (a-e) shows the preparation process for the EG: few graphite flakes are placed on the adhesive tape (a), layers of the flake are peeled off by another tape (b), peeling off is repeated until the tape is occupied with many exfoliated flakes (c-d). During the process, large grains in the flake turn to thin-small grains on the tape. Finally, the target substrate is placed by facing to the tape to transfer graphene layers (e).

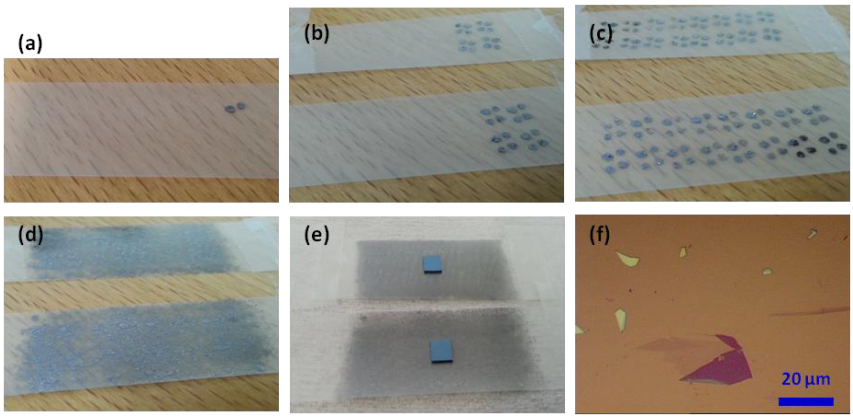

Figure 5. Mechanical exfoliation of graphene. (a-d) Exfoliation of graphene layer(s) from graphite flakes with an adhesive tape. (e) SiO_2/Si substrates placed on the tapes to transfer the graphene flakes exfoliated. (f) Optical image of graphene flakes transferred.

Many graphene flakes having the different number of layers are typically transferred on the substrate with large amount of glue residue. The residue can be removed through acetone treatment followed by isopropanol and deionized water rinsing process. The optical microscopic image of the graphene flakes including single-layer placed on SiO_2/Si substrate is shown in Figure 5(f). When about 300 nm of SiO_2 is deposited on Si, single-layer graphene can be identified through the optical microscope due to visible contrast between two materials. In Figure 5(f) the area of light-pink in the flake presents the single-layer and the dark-pink multi-layer graphene (details for characterization of the flake in Chapter 4).

3.2 Epitaxial graphene (EPG) on SiC

A graphene film can be epitaxially grown by thermal decomposition of SiC [77]–[79], [Publication 7], which is the so-called *epitaxial graphene* (EPG). SiC is a IV-IV compound semiconductor and has tetrahedron crystal structure. The

carbon atom is positioned at the center of tetragonal structure, which is favorable for the crystal to desorb the silicon atoms only. The schematic of the tetrahedron structure of SiC is shown in Figure 6(a) and (b). There are many different crystal structures of SiC, *polytypes*. Although there are more than 200 known polytypes, they are basically consisted with same chemical composition: 50% of carbon atoms bonded to 50% of silicon atoms [80], [81]. For graphene growth, the polytypes 3C-SiC, 4H-SiC, and 6H-SiC are typically utilized due to the behavior of thermal decomposition occurring along the periodic stacking direction. The stacking orders of the three different polytypes are shown in Figure 6(c-e). The 3C-, 4H- and 6H-SiC are the SiC polytypes having the 3 layers, 4 layers, and 6 layers per period along the stacking direction, respectively [80].

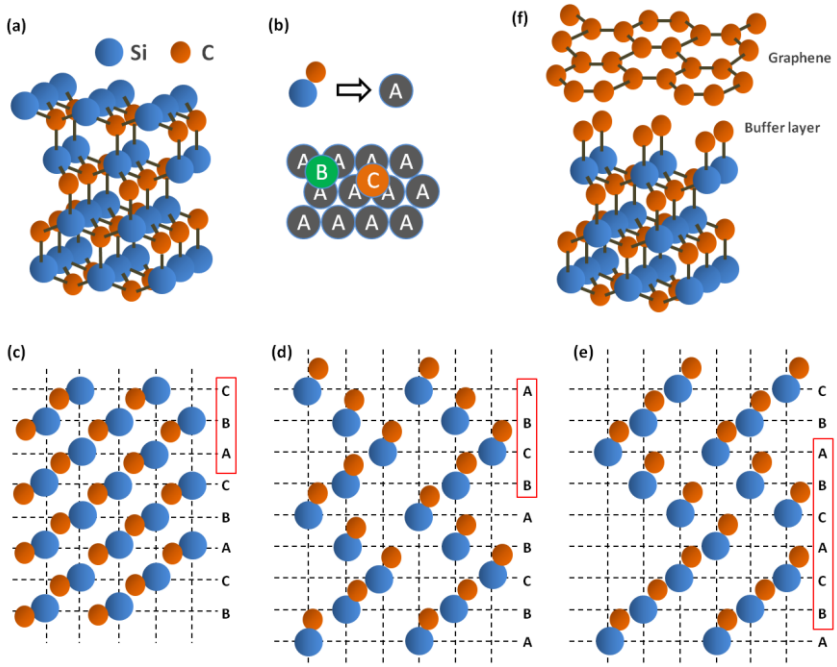

Figure 6. (a) Tetrahedron crystal structure of SiC. Carbon atoms bond with four nearest silicon neighbors. (b) Top-view of crystal structure of SiC where the pack of Si-C atom is denoted to the ball "A" as a component of the first layer. "B" and "C" are the second and the third layer, respectively. (c-e) Three most common polytypes of SiC: (c) 3C-SiC with 3 layer period, (d) 4H-SiC with 4 layer period, and (e) 6H-SiC with 6 layer period along the stacking direction. (f) Schematic of graphene/SiC interface formed by thermal decomposition of SiC. The buffer layer, also known as 'layer 0', is placed in between the first graphene layer and the bulk SiC.

The growth of graphene is achieved by graphitization through annealing the SiC at a temperature where Si atoms are desorbed and C atoms are remain on the surface. Typical process temperature is around 1300 – 1700 °C. In general, Si face 4H- and 6H-SiC are preferred in graphene growth because the decomposition on Si-face SiC is slow and it process terminates in a short time. This is an

advantage for the process to grow the ultra-thin layer. In contrast, the process on C-terminated SiC does not self-terminate, resulting in the formation of thick layers (up to 100 layers) [79]. Due to the behavior of epitaxial growth, ultra-thin crystal graphene can be synthesized on SiC without the size-limit (the graphene size is determined by the wafer scale). Moreover, different from EG or deposited by CVD (which will be discussed in the next section), the graphene film on SiC can be utilized without the transfer process, implying that external contaminations induced from the extra process can be minimized. As a consequence, epitaxial graphene has typically higher carrier mobility [79], [82], [83] when compared to other graphene sources synthesized. Therefore, SiC is an promising material realizing a wafer scale high-speed graphene ICs [82] . However, SiC is a semiconducting material so that only a wide bandgap type of SiC which acts as an insulator can be utilized. This is also the reason that 4H- and 6H-SiC are often selected for epitaxial graphene synthesis [81].

3.2.1 Experimental for epitaxial graphene (EPG)

Figure 7(a) shows an atomic force microscopic (AFM) image of epitaxial graphene grown on Si-terminated 4H-SiC. In the process the SiC substrate was annealed at 1620 ºC for 5 min in argon ambient at atmospheric pressure to desorb the Si atoms. Due to the mis-cut of the SiC wafer, the step-like terraces are exhibited after thermal treatment as seen in Figure 7(a) and (b). Raman spectra in Figure 7(c) identify that epitaxial graphene is formed on the SiC surface as the D-, G-, and 2D-peak arise (details about Raman for graphene are discussed in Chapter 4).

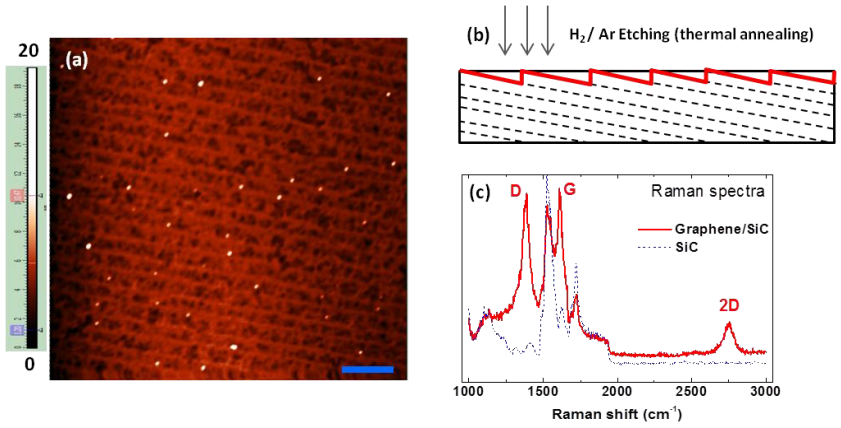

Figure 7. Characteristics of graphene grown at 1620 °C on 4H-SiC. (a) AFM image and (b) schematic of the cross-sectional profile of the SiC surface after thermal annealing

in a H_2/Ar ambient. (c) Raman spectra for SiC (dotted line) before and (solid line) after growth of graphene.

It is important for EPG to control the number of layers during the growth since single- or double-layer graphene are desired for a device to utilize the unique 2-dimensional transport effect. Among the parameters, temperature is the most significant in determining the graphene crystal as well as the number of layers. Therefore, to obtain the crystallized ultra-thin layer (< 3 layers), temperature-dependent growth behavior should be understood. Table 1 shows properties of the graphene layers grown at different temperatures [Publication 7].

Table 1. The measured mobilities, carrier densities and the number of layers for the samples grown at different temperatures. Data is reproduced from [Publication 7]. Hall measurement and AES were performed by E. Vesapuisto and S. Novikov.

Growth temperature (°C)	Average Hall mobility (cm^2/Vs)	Average sheet carrier density (cm^2)	Average number of graphene layers
1520	-	-	0
1540	81	7.72×10^{12}	0.56
1590	126	4.06×10^{12}	0.95
1650	361	3.02×10^{13}	1.45
1710	77	2.84×10^{14}	1.64

The results show that graphene starts to grow at about 1550 °C and its thickness is optimized to ~1 layer in 1590-1650 °C. The mobility and carrier concentration were further obtained by Hall measurement and the number of layers was determined by Auger electron spectroscopy (AES). Mobilities shown in the Table 1 are relatively low although the higher mobility is typically expected on EPG. Carrier concentrations in the samples are unexpectedly high, indicating that high density of impurities or defects in graphene are associated. Figure 8 shows the Raman spectra for the samples, which indicates that the carbon layer begins to form at 1590 °C and its crystallinity appears at the sample grown at 1650 °C. The high intensities of the D-peak (at ~1350 cm^{-1}) are also observed in the samples grown above 1650 °C, implying that the graphene layers contain a certain amount of crystal defects. This results in lowering the carrier mobility (as shown in Table 1).

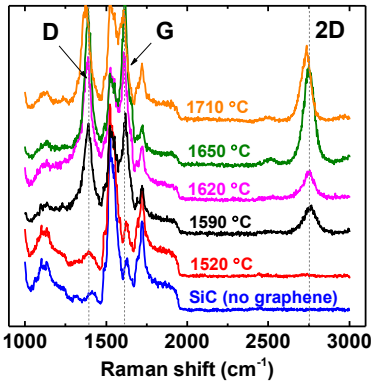

Figure 8. Raman spectra of EPG samples fabricated at different temperatures, corresponding to the samples shown in Table 1. The dotted lines indicate the positions assigned to D- (~ 1350 cm^{-1}), G- (~1580 cm^{-1}), and 2D-band (~ 2700 cm^{-1}) for graphene.

3.3 Chemical vapor deposition of graphene on transition metals

Although epitaxial graphene on SiC consists of high quality graphene in large scale [79], [83], the cost for its production is very high due to the expensive SiC wafer. In alternative, synthesis by CVD on transition metals has been proposed owing to its simple and cost effective process. The transition metals utilized as a catalyst for the CVD have non-filled *d*-shells that enable them to interact with hydrocarbons and absorb carbon sources very efficiently [84]. Various catalytic metals, such as, titanium (Ti), hafnium (Hf), tantalum (Ta), tungsten (W), rhenium (Re), ruthenium (Ru), cobalt (Co), rhodium (Rh), iridium (Ir), nickel (Ni), palladium (Pd), platinum (Pt), copper (Cu), silver (Ag) and gold (Au), have been used for the graphitic layer growth through CVD [85]. Among the materials, Ni and Cu are most widely selected for the graphene growth due to stability for the formation of sp^2-hybridized graphitic structure [86]. Those are abundant in the earth and easily handled in etching process. However, growth mechanisms of graphene for these two metals in CVD are clearly different. At high temperature the dissociated carbon atoms at the Ni surface typically diffuse into the bulk and at low temperature they preferentially diffuse out to the surface (Co and Fe show similar catalytic behavior). On the other hand, due to very low solubility of carbon to the bulk, the film formation on Cu is activated only through the surface reaction [42], [87]. This behavior is very useful for the production of uniform single-layer graphene in large scale.

3.3.1 Growth behavior on Ni and Cu

When hydrocarbon (C_XH_X) gas molecule contacts the heated metal surface, it decomposes to meta-stable carbon. On Ni, above ~800 °C at low pressure, the decomposed carbon atoms are preferred to diffuse into the bulk. This is *surface segregation*. The solubility of carbon in Ni is strongly dependent on the temperature: high solubility in high temperature and low solubility in low temperature. This allows the carbon atoms to diffuse out from bulk to the surface when the substrate cools down from high temperature. This process is called *precipitation* [87], [88]. The previous studies [89], [90] have been revealed that the carbon preferentially precipitates out through the grain boundaries of Ni, which results in thicker graphitic layer formation at the grain boundaries. Consequently, the thickness of the graphene layer on Ni can be dominantly determined by the cooling rate. The schematic of the precipitation process on Ni is depicted in Figure 9(a).

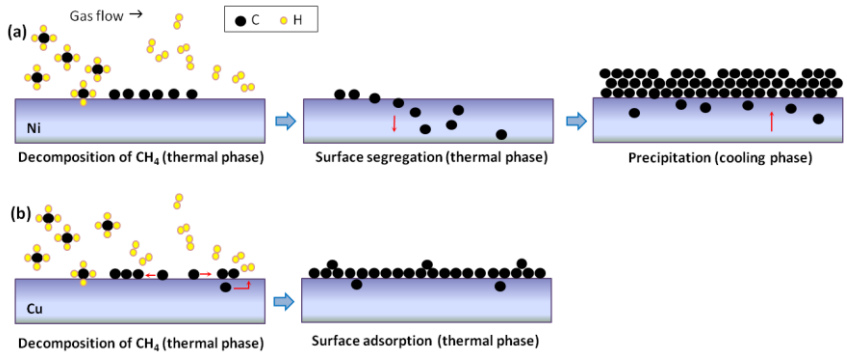

Figure 9. Schematic of the CVD process for graphene (a) on Ni and (b) Cu.

Due to the growth process, non-uniform multilayer graphene is typically grown on Ni substrate and, thus, a very accurate control of the cooling rate is demanded for preparation of uniform single-layer graphene. Graphene layer formed on Ni is strongly bonded to metal with the smallest distance (2.1-2.2 Å) since graphene lattice is well matched to that of Ni [85]. For the crystallized graphitic film on Ni, the CVD process is implemented at 900 – 1000 °C [88], [91]–[93]. A cooling rate of about 10 °C/s has been suggested for the ultra-thin layer in precipitation [88].

In contrast to Ni, the growth process on Cu is dominantly controlled by the surface reaction due to very low solubility of carbon atoms into the bulk. Thus, the graphene film is formed along the surface by the adsorption of decomposed carbon atoms in a thermal phase and, consequently, its process almost inde-

pendent from a cooling. The surface adsorption process is schematically depicted in Figure 9 (b). This behavior allows the growth process to be self-terminated when the metal surface is fully covered by very first single-layer graphene. In addition, the interaction between graphene and Cu is week [85] and this further allows graphene to expand over the Cu grains more easily [42], [86], meaning that the determination of graphene crystallinity is not strongly relied on Cu grain but related to the surface reaction and the density of the nucleation site.

When the decomposed individual carbon atoms, *monomers*, are preferentially adsorbed in the surface sites (energetically allowed states in Cu(111) are further discussed in detail in ref. [94]), they spontaneously form carbon-carbon bonds (C_2), *dimers*, since the dimers are energetically stable. The dimers are easily assembled into larger graphitic units because the dimers are persistent and mobile through the low migration barrier in the Cu(111) surface [94]. Back-dissociation of dimer to monomer is considerable but a reaction of the mobile dimer-chain is dominant since the much higher energy requires to dissociate the dimer than to migrate. Therefore, the dimer plays a key role to form and expend the carbon chains along the Cu surface. Figure 10(a) schematically depicts the process of the first stage of nucleation on the Cu(111) surface. After the nucleation is completed, the carbon chains grow rapidly by merging with other monomers, dimers, and fragments (which are also mainly contributed to the dimers).

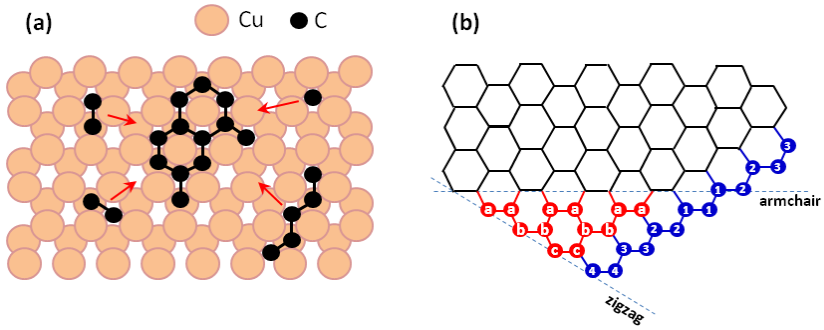

Figure 10. Schematic of (a) nucleation process for graphene on Cu (111) and (b) converting process from armchair to zigzag (atoms in red) and spreading process towards zigzag direction (atoms in blue). Alphabet (or Arabic number) pair denote the dimer.

The dimers (or small fraction of monomers) further contribute to expansion of the graphene layer through creating the zigzag edge [95]. The armchair edge is converted to the zigzag by energetically preferred bonding. The process of the edge expansion with the dimer attachment is shown in Figure 10(b). The alphabetic order from **a** to **c** (or the Arabic numbering order from **1** to **4**) is a sequence of attachment which exhibits the process converting from the armchair

to the zigzag edge (or expansion of the zigzag edge). The expansion of graphene layer easily cross over the Cu grain and terminates when the grains originated from each nucleation meet each other. It results in the graphene film on Cu to be a polycrystalline with the boundaries (which act as a structural defects [96]–[99]). Therefore, the grain size is strongly dependent on the density of nucleation. Fewer population of nucleation sites is desired in CVD toward the larger grain of graphene.

The crystallinity of the film is also affected by the process temperature. The carbon film can be grown at about 700 °C but it is almost amorphous. The crystallinity can evolve from amorphous to a crystal by increasing temperature [100], [Publication 4] (temperature dependent growth behavior is discussed more in Chapter 5).

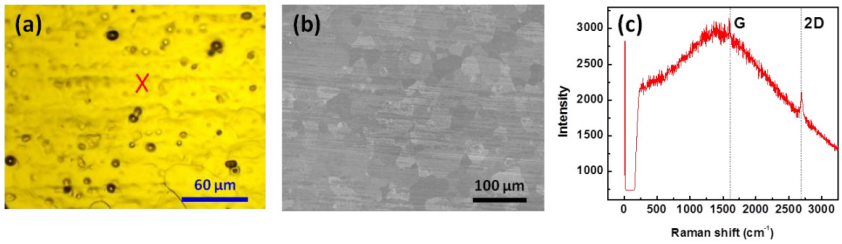

Figure 11. (a) Optical and (b) SEM image of the graphene film grown on Cu. (c) Raman spectrum obtained at the point 'X' marked in (a).

Figure 11 shows the graphene film on Cu grown at 935 °C by photo-thermal CVD (photo-thermal CVD is introduced in Chapter 5). As seen in the scanning electron microscope (SEM) image in Figure 11(b), the Cu grain is restructured as a polycrystal after annealing above 900 °C although intrinsic structural defects still remain (small dots seen in Figure 11(a)). Fully covered single-layer graphene on Cu is hardly identified on optical microscope and SEM due to the strong metal background reflection. For clear observation, the graphene film on metal needs to be transferred to a proper substrate, such as SiO_2/Si substrate. Nevertheless, Raman can detect graphene although amount of fluorescence signal arises from the Cu as shown in Figure 11(c) (characterization techniques and tools are discussed more in Chapter 4).

3.3.2 Transfer

Different from EPG on SiC, the film synthesized by CVD on metal needs to be separated from the substrate for further characterization as well as fabrication to

electronic devices. Graphene grown on Cu is typically a single-layer and, thus, is mechanically fragile as well as chemically vulnerable for external doping. Ambient impurities like a moisture or contaminations incorporated during the transfer process can change the doping level significantly. Therefore, a transfer without damages and contaminations is the key for maintaining pristine properties of graphene.

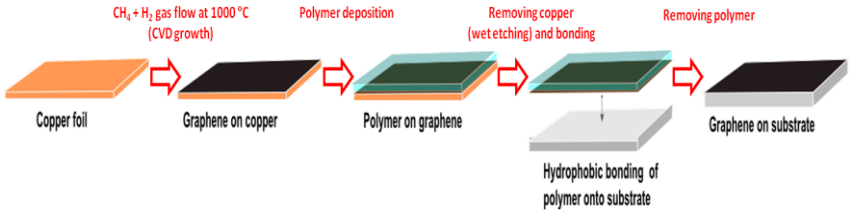

Figure 12. Schematic of the transfer process for graphene grown on the Cu foil.

Although such transfer free methods (direct etching for metal on substrate without transfer) [44], [101], [102] or electrochemical delamination [103] have been proposed, so far the polymer-based transfer technique is widely used due to simple and reliable process. Poly-methyl methacrylate (PMMA) is commonly utilized as a transfer medium. The schematic of the process transferring the graphene film to target substrate by the polymer is shown in Figure 12. In the transfer, as-grown graphene on the Cu foil is first coated with PMMA followed by removing Cu, for example, by etching in ferric chloride ($FeCl_3$) or ammonium persulfate ($(NH_4)SO_4$). During etching the Cu foil is floating on the solution. Once etching is completed, the polymer with graphene remains floating on the solution. The polymer/graphene film is moved onto deionized water (DIW) for rinsing and finally transferred onto the target substrate. The very thin polymer/graphene film is bonded to the substrate through the van der Waals force. The bonding can be enhanced with a baking in 120 ~ 150 °C in ambient (or vacuum) by reflowing the PMMA. In the final step, the PMMA is stripped in acetone.

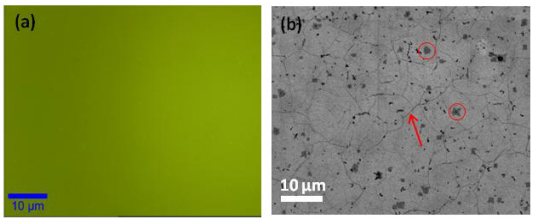

Figure 13. (a) Optical and SEM image for CVD graphene transferred on SiO_2/Si substrate. Red arrow and circles in (b) indicates the wrinkle and the few layer flake, respectively.

Figure 13 shows images of graphene transferred onto a SiO_2/Si substrate. The optical and SEM images are focused to the same position. In optical microscopy, graphene is hardly recognized due to its transparency while in SEM graphene is clearly identified, containing wrinkles (red arrow) and few-layer flakes (red circles). The wrinkles and few layer flakes are generally considered as structural parasitic defects. The wrinkles are considered to form during cooling after the growth process performed at about 1000 °C due to the difference in thermal-expansion coefficient between graphene and Cu. The origin of the few-layer (or adlayer) flakes is unclear yet but is expected to be related to precipitation of small portion of carbon atoms which are diffused into Cu.

4. Characterization of graphene

Before a device is fabricated, the graphene layer needs to be characterized to identify the quality. Number of layers, crystallinity, and the density of defects are the critical factors determining device performance. For example, best carrier mobility is displayed at the crystallized single-layer. Crystal defects such as voids, dislocations, vacancies or substitutional impurities [104] lead the degradation of carrier transport, resulting in eventually decay of device performance. SEM provides very clear surface morphology identifying the areas with the different number of layers, voids, and wrinkles. Tunnelling electron microscope (TEM) is an excellent tool to clarify an atomic structure of lattice. The crystal defects can be directly observed in TEM. Among the known techniques, Raman spectroscopy is considered as the most powerful one to characterize carbon-related materials as crystallinity and the number of layers can be confirmed very efficiently [105].

The physical properties of graphene can be directly examined by electrical measurement. Hall measurement is considered as a standard to indentify electrical properties owing to reliable parameter acquisition, which has been so far utilized widely for semiconductor analysis. The transfer-length method (TLM) is also well-established for analysis of contact resistance which is created when two different materials contact each other. TLM is straightforward to confirm contact resistance only from I-V characteristics obtained from 2-probe measurement. Mechanical properties of graphene can be characterized by deforming the membrane with a pressure [4], for example, a bulging test.

In this chapter, characterizing tools and techniques for a graphene layer are presented. Tools for morphological characterization, such as, an optical microscope, a scanning electron microscope, multi-photon microscope, and a tunnelling electron microscope are introduced in brief. Raman spectroscopy is overviewed in detail, including a review of the Raman scattering process. In addition, TLM and bulge experiment for a graphene layer are presented.

4.1 Surface morphology

The optical microscopy is a simple, rapid, and non-destructive method for characterization of graphene. Although 98% of the light transmits (opacity: ~2.3%) [106], the graphene is visible in optics when a transparent medium with a certain thickness (t) is incorporated between graphene and the substrate. Silicon dioxide (SiO_2), aluminium oxide (Al_2O_3), or silicon nitride (Si_3N_4) are well-known media for graphene observation. A contrast difference between two materials, graphene and medium, enables graphene to be visible even in a white light. This can be explained by the Snell's law and Fresnel theory. The experimental results has revealed that the contrast for graphene is highest when t= 300 nm for SiO_2 [107], t= 72 nm for Al_2O_3 [108], and t= 64 nm for Si_3N_4 [109]. The contrast is also strongly dependent on co-relation between the wavelength (λ) of the incident light and the thickness of the medium (t). For instance, the contrast is maximized when λ= 560 nm at t= 300 nm and λ= 410 nm at t= 200 nm for SiO_2 [106]. This behavior is utilized to indentify the number of layers as Figure 5(f) shows that the layer feature of graphene flakes placed on 300 nm of SiO_2 are clearly discriminated by the color. However, it is not satisfied for CVD graphene where the layer is homogeneous in large scale as seen in Figure 13(a). Moreover, the optical microscopy does not provide detailed crystal information of graphene.

SEM is a tool widely used to characterize the graphene layer. As it utilizes the backscattering energy of the electrons at the surface, the graphene morphology can be monitored regardless of the substrate type, for example, identifying micrometer scale flake and a wrinkles as shown in Figure 13(b). The excited energy of electrons typically selected to 1-20 kV to avoid the possible damage from the electron bombardments. The microscopic scale in SEM can be down to few nanometers but the resolution is not sufficient to observe the crystalline structure in atomic scale.

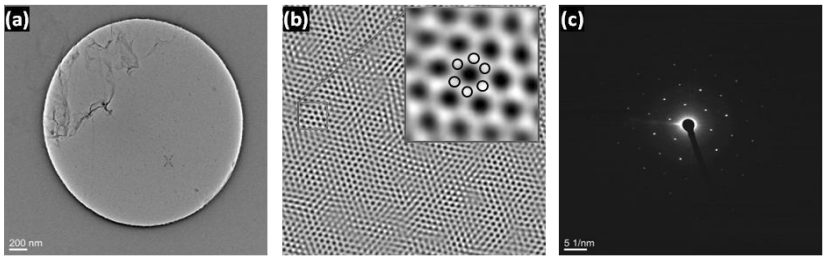

Figure 14. (a-b) TEM images. (b) Magnified image for the area marked 'x' in (a). The inset in (b) is the image enlarged for the area indicated by the solid box. The black circles in the inset denote the carbon atoms in hexagonal ring. (c) Diffraction pattern taken from a region in (a). The images taken by J. Huang of Aalto University.

In alternative, TEM is adopted for analyzing the atomic scale. TEM is a technique in which the electron beams transmitted through the ultra thin membrane are collected through a detector. The beam interacted with the specimen can be magnified to atomic scale. Based on the atomic-resolution characteristics, crystal structure including configuration of atoms as well as structural defects like grain boundaries [96] can be clearly examined. Figure 14 (a-b) shows the TEM images for suspended single-layer CVD graphene. The image in Figure 14(b), magnifying the area marked by 'x' in (a), demonstrates the hexagonal lattice of graphene. The circles marked in the inset of Figure 14(b) denote the positions of atoms in the hexagonal lattice. When considering the few-angstrom-thick single-layer graphene, the atoms in the membrane act as a diffraction grating to the electron beams. The electrons passing the membrane are treated as wave-like, rather than particle-like, due to extremely narrow wavelength of ($\sim 10^{-12}$ m) electrons at the high energy (accelerated by few hundred kV). This behavior additionally exhibits a series of spots in the image, the so-called *diffraction pattern*. Figure 14 (c) shows the diffraction pattern taken from a region in (a) and further indentifies a hexagonal lattice configuration, demonstrating that each atom is configured by rotating 60 degree to the neighbors. The diffraction pattern is also useful to verify not only the number of layers (single to few layers) but stacking configuration of multilayer by measuring a misorientation angle [110].

4.2 Raman spectroscopy

Raman spectroscope is a popular and widely used tool for characterization of graphene due to the fast, accurate, and reliable non-contact process. The Raman spectroscopy utilizes emission of vibrating phonons which dissipate the initial incident energy of photons during back scattering. This is called *Raman scattering* which was discovered by Sir Chandrasekhara Raman in 1928. It plays an important role in characterization of graphene as spectra obtained from Raman scattering contain information of the crystal structure, the number of layers, the stacking configuration as well as the doping level. Therefore, Raman spectroscopy is preferentially adopted for the examination of the graphene quality.

4.2.1 Raman scattering

When a monochromatic beam of the light such as a laser is incident on the surface of a material, most of photons are elastically scattered back. This is

called *Rayleigh scattering*. During the scattering, however, a small fraction of the light, approximately 1 in 10^7 photons, is dissipated to vibration of atoms (or molecules), generating phonons. It results in an inelastic scattering process, called *Raman scattering*. Therefore, the difference in energy between the incident photons (E_1=$h\nu_1$) and elastically scattered photons (E_2= $h\nu_2$) is equal to the energy of the scattering phonons (E_{ph}= $h\nu_{ph}$). The h and ν are a Planck constant and frequency, respectively. The Raman process based on the first-order principle is schematically depicted in Figure 15(a).

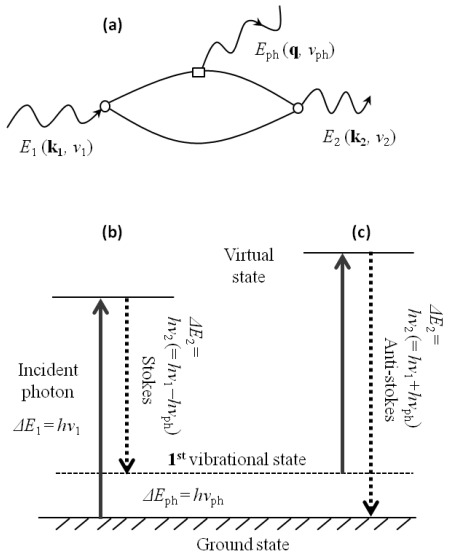

Figure 15. (a) Diagram of a first –order Raman process. (b-c) Energy level diagram for Raman scattering: (b) Stokes Raman scattering and (c) anti-Stoles Raman scattering. ΔE_1 and ΔE_2 are the energy of incident and scattering photons, respectively, and ΔE_{ph} is the energy of scattering phonons.

In the process of first-order Raman, the incoming photon E_1 excites an electron and the excited electron is finally recombined with a hole, emitting an elastically scattered photon with the energy E_2. During recombination, an atomic vibration arise, which results in emitting phonons with the energy E_{ph} (Figure 15(a)). When the initial state is a ground state, the scattering photon has lower energy, called *Stoke scattering*, while when atoms or molecules are in already exited state, the scattering photon has higher energy than that of the incident photon by leaving the atoms in the ground state, called *anti-Stokes scattering*. The Stoke and anti-Stoke process are schematically depicted in Figure 15 (b-c). Therefore, the wavenumber of the scattering light in Stokes is smaller while that in the anti-Stokes process is larger than the that of the incident light. The energy difference can also be described as wavenumbers or the so-called *Raman shift* as:

$$Raman\ shift = \frac{1}{\lambda_{incident}} - \frac{1}{\lambda_{\text{scattered}}} \quad (4.1)$$

where $\lambda_{incident}$ and $\lambda_{scattered}$ are the wave length of the incident and back scattering photons, respectively.

The Raman shift in a certain material is unique since Raman scattering arises from the excited energy of molecules and transition energies through crystal structure. Consequently, the components (or molecules) of material and its structure can be identified with the Raman shift of the peaks appearing in the spectrum.

4.2.2 Experimental: Raman spectroscopy in graphene

In graphene, there are the six phonon dispersion curves along the high symmetry ΓM and ΓK in Brillouin zone (BZ), assigned to longitudinal optical phonon (LO), in-plane transverse optical phonon (iTO), out-of-plane transverse optical phonon (oTO), longitudinal acoustic phonon (LA), in-plane transverse acoustic phonon, and in-plane transverse acoustic phonon (iTA) [111]. Each of the 6 phonon modes play a role in Raman spectrum for graphene. Figure 16 shows an example of Raman spectrum for single-layer graphene obtained by 2.33 eV of laser excitation (532 nm Nd-YAG green laser). Three most prominent peaks which are assigned to D-, G-, and 2D-band appear in between 1200 – 3000 cm^{-1}.

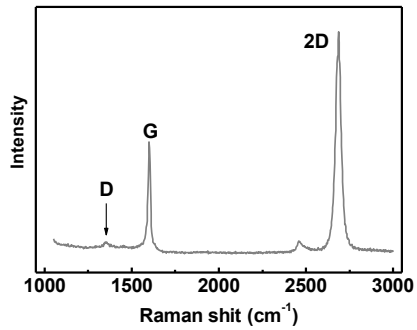

Figure 16. Raman spectrum of single-layer graphene.

The G-band is, in fact, associated with the first-order Raman scattering process in graphene. Figure 17(a) depicts the process of the first-order process (which was also described in Figure 15) with the energy band diagram. The G-peak appearing at ~1590 cm^{-1} is a result of inelastic scattering of light associated with two phonons (iTO and LO). On the other hand, the D- and 2D-band appearing at ~1350 cm^{-1} and ~2690 cm^{-1}, respectively, are considered to originate from a

second-order process. The D-band is known as a disordered induced band and the 2D is called since its frequency is approximately double from the D-band ($\nu_{2D} \sim 2\ \nu_D$). When an electron with the wave-vector **k** absorbs an incident photon energy E_l, the electron is inelastically scattered by a phonon (or a defect) of the energy E_{ph} with wave-vector **q** around *K* point (wave-vector **k** and **q** are denoted in Figure 15(a)). The electron wave (**k**+**q**) is further dispersed to the point of the band around *K'* and the excited electron is scattered back to a **k** state with emitting a photon by recombining with a hole at a **k** state (in *K* point). This is the so-called *double resonance* (DR) process [111]. Figure 17(b-c) show the DR process schematically. The D-band is associated with one defect and one iTO phonon, which, consequently, consist of one elastic scattering by the defect of crystal and on inelastic scattering by emitting or absorbing a phonon (Figure 17(b)). The 2D-band is involved with two phonon-related processes (two iTO phonons) contributed to only the inelastic scattering process (Figure 17(c)).

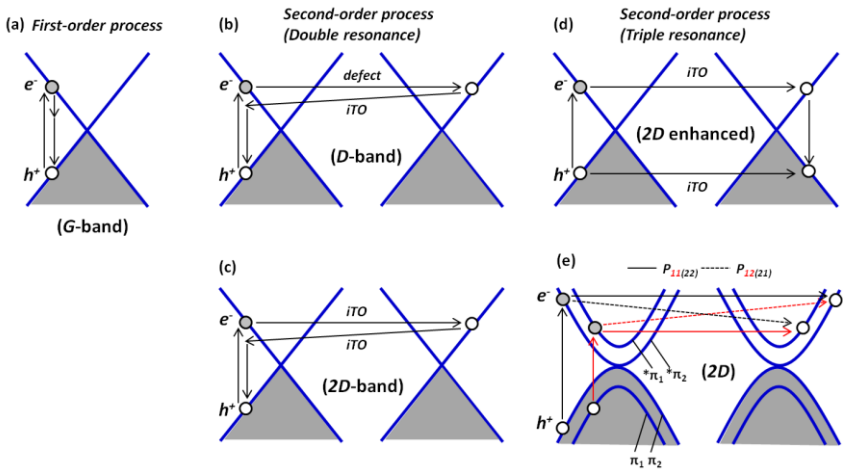

Figure 17. Raman process in graphene. (a) First-order process, (b-c) Double resonance process: (b) one-phonon second-order process associated with defect for D-band and (c) two-phonon second-order process for 2D-band, (d) Triple resonance: electron and hole resonant scattering process (2D-band enhancement), (e) Four double-resonance processes in AB stacking bi-layer.

In the DR process, two resonance processes can be explained by three scattering events with only the electron. However, in graphene Raman process can also occur by a hole scattering. This arises because the energy bands are in linear E(*k*) dispersion, namely, the valence and conduction bands are almost mirror by the Fermi energy. The linear energy dispersion can lead an important effect that the hole near K point will be scattered by a phonon wave-vector **q** (here can assume the wave-vector **−q** for a backscattered electron in DR process). In this case, both the electron and hole scattering processes resonantly occur and finally the

electron-hole recombination at the K' point will also occur in resonance state. This is the so-called the *triple resonance* (TR) process [111]. The TR process significantly enhance the 2D-band, resulting in a larger intensity relative to the G-band (as seen in Figure 16). This is very remarkable for single-layer graphene since the TR is a unique process for all sp^2 carbons due to the linear dispersion. Therefore, a single-layer can be simply confirmed by comparing the intensity of the G- and 2-D peaks. Both are single Lorentzian peaks in single-layer graphene.

In the case of bilayer graphene, the Raman process is strongly involved with the inter-band process. For AB-stacked two-layer graphene, the electron and phonon bands split into two components with special symmetries, corresponding two parabolic E(k) dispersion energy bands. Figure 17(e) shows the split bilayer graphene energy band structures where inner (outer) valence and conduction band are labeled with π_1 (π_2) and $*\pi_1$ ($*\pi_2$). The arrows in Figure 17(e) denote the second order processes which indicates that four different DR process arise in a conduction band as P11, P12, P21, and P22. Consequently, these four different Raman scattering give rise to four Lorentzian peaks in the 2D-band. Figure 18 shows Raman 2D-band for bi-layer graphene probed with 2.33 eV of laser excitation.

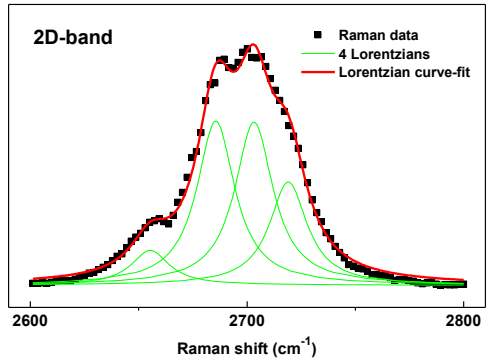

Figure 18. (black dots) Raman signals and (red-solid line) curve fitted with 4 Lorentzian sub-bands for 2D-band.

The Raman peak denoted by solid line with the black dots corresponds to the curve-fit with 4 different sub-bands (green) each with a full width half maximum (FWHM) of ~22 cm^{-1}. The measurement is well matched to the theoretical assumption described in Figure 17(e). The number of allowed Raman peaks of the 2D-band for AB stacking tri-layer graphene is fifteen [111], indicating that 15 different DR processes can occur. However, in energy transitions many are very close to each other and, as a result, the minimum number of peaks appears in experiment, *i.e.* typically ~6 peaks are observed [111]. When increasing the number of layers (>> 4 layers), then the high frequency side of the sub-peaks of

the 2D-band has a larger intensity than that for the fewer graphene layers. This results in the peak position of 2D-band is shifted towards the high-frequency region in experiment. Accordingly, it is very difficult to estimate the number of layers by Raman when graphene has more than 3-4 layers [112]–[114].

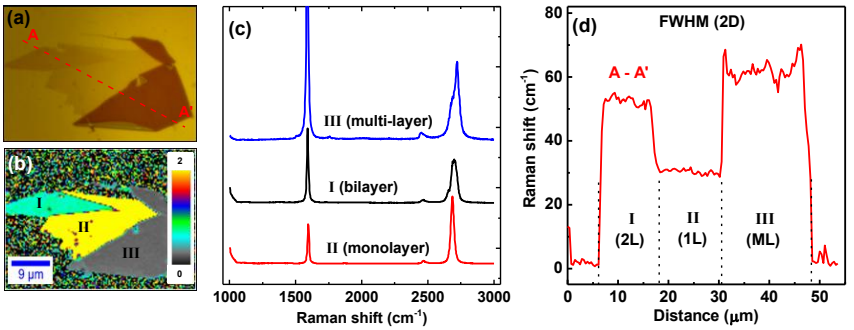

Figure 19. (a) Optical and (b) Raman I_{2D}/I_G mapping image for an exfoliated graphene flake. In the Raman map, the area in yellow denotes a single-layer (II), in cyan a bi-layer (I), and in dark grey a multilayer (III). (c) Raman spectra for the area I-III marked in (b). (d) Profile of FWHM for the 2D band along the A-A' line in (a).

Figure 19 shows Raman measurements for a graphene flake (shown also in Figure 5(f)) prepared by mechanical exfoliation, which is composed of three different regions having the different number of layers. Comparing to the optical image, the Raman mapping image of the ratio of 2D- to G-band intensities (I_{2D}/I_G) clearly displays three different regions: area I for the bi-layer, II for the single-layer, and III for the multi-layer as shown in Figure 19(b). The peaks in Figure 19(c) further verifies that the area I and III are in AB stacking. The peak of 2D-band for the area I is fitted with 4-different Lorentizians (as seen in Figure 18) and for the are II with a single Lorentzian, which are agreed to a nature of the bi-layer and the single-layer, respectively. Another significant feature in Raman for graphene is the full width half maximum (FWHM) of 2D-band. By more DR processes involved through the inter-band transitions, the FWHM becomes larger as the number of layer is increased. The Figure 19(d) shows the FWHM profile along the line A-A' in Figure 19(a). The FWHM for the area I is in ~50-53 cm^{-1}, for II ~31 cm^{-1}, and for III ~60-70 cm^{-1} at 2.33 eV of laser excitation. The levels exactly correspond to the number of layers determined by the I_{2D}/I_G analysis. The D-band, on the other hand, can be utilized for structure analysis, particularly for the defects (or disorders). In principle no D-peak arises in case the lattice is perfectly formed by the crystal. Therefore, it preferentially appears at the edge of graphene due to the possible imperfection of lattice. Figure 20 shows the Raman mapping of the D-band for the flake shown in Figure

19, presenting that the edge of the flake or the borders of grains (= the areas in the different numbers of layers).

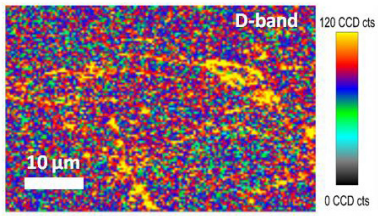

Figure 20. Raman mapping image filtered by D-band for the sample shown in Figure 19(a).

4.2.3 Raman overtone and combination modes

In multilayer graphene, the stacking configuration can be characterized utilizing the Raman bands appearing in the range of 1690-2150 cm^{-1}. Particularly, the band observed at about 1750 cm^{-1}, which is the overtone of the out-of-plane transverse optical (2oTO) phonon and is assigned as the *M-band*, is valuable in determining the number of layers as well as in confirming the stacking order for multilayer graphene. The M-band appears only in AB-stacked multilayer graphene but not in either the single-layer or turbostratic multilayers [115], [116]. Therefore, the M-band starts to appear in the bi-layer (2L) area and its intensity becomes stronger in the multilayer region as shown in Figure 21. In addition, other significant features of the combination modes are found at ~1890 cm^{-1}, the combination of iTA+LO, and ~2020 cm^{-1}, the combination of iTO+LA [117]. The peak at ~1890 cm^{-1} (2020 cm^{-1}) becomes weaker (stronger) as the number of layers increase as seen in Figure 21. All three peaks are also blue-shifted with an increasing the number of layers. The spectra in Figure 21 contain a significant sign regarding the layer stacking: the area I and III (which correspond to those in Figure 19) are consisted with AB-stacked bi- or many layers. This can be proved with the M-band as no peak arises in the area II but in I and III. The blue-shifted M-band in the area III also indicates that the area is consisted with many AB-stacked layers. The results are also well agreed to the results obtained by examinations through the intensity ratio (I_{2D}/I_G), the curve-fit with Lorentzain(s), and the FWHM of 2D-band.

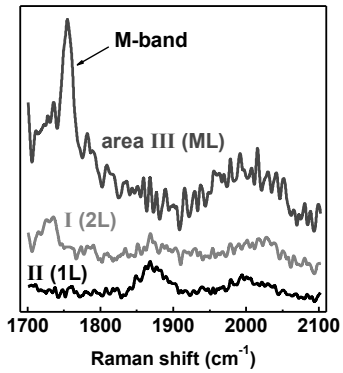

Figure 21. Raman spectra appearing in the range of 1700-2100 cm^{-1} for the areas I-III shown in Figure 19(b) with the laser excitation of 2.33 eV. 1L, 2L, and ML denote a single-, bi-, and multi-layer, respectively.

4.2.4 Raman fingerprint for doping

The doping status of graphene can also be examined through Raman spectroscopy. When either electron or hole concentration is increased, the position of the G-band is up-shifted and its FWHM is decreased [118]–[120]. In the second-order process, an electron in the valence band is excited to the conduction band by absorbing a phonon (created by the first-order process), which creates an electron-hole pair. The electron is recombined to a hole, thus, emitting a phonon. The electron-phonon interaction is most effective at $E_F = 0$ (the Dirac point). Consequently, when the Fermi energy is changed, there is a reduction in the electron-phonon interactions. The interaction is only allowed when the G-band phonon energy (E_{ph}) is larger than $2|E_F|$. Therefore, if the Fermi level is increased to be higher than $E_{ph}/2$, there is a blockage of phonon decay into electron-hole pairs, which leads to a change of the G-band position as well as its FWHM [111]. However, this Raman fingerprint is acceptable for pure crystal graphene only. In case of disordered graphene with defects which is analogous to appearance of the significant D-band, the correlation between the position and FWHM of the G-band behaves differently for the doping: the position is up-shifted with the broadening peak (the FWHM is also increased). For the 2D-band, on the other hand, its position is also slightly affected when the graphene layer is doped. The direction of the shift is dependent on the doping type as an upshift is occurred by the hole doping and a downshift by the electron doping [120].

4.3 Multi-photon spectroscopy

Raman spectroscopy is powerful for characterizing graphene but is not fully satisfactory for large area probing due to the low scanning speed for mapping. In alternative, multi-photon microscope (MPM) can allow mapping of large scale graphene rapidly. Utilizing nonlinear optical response, such as, second-harmonic generation (SHG), third-harmonic generation (THG), or fluorescence induced by multi-photon adsorption, the graphene layers can be examined [Publication 6].

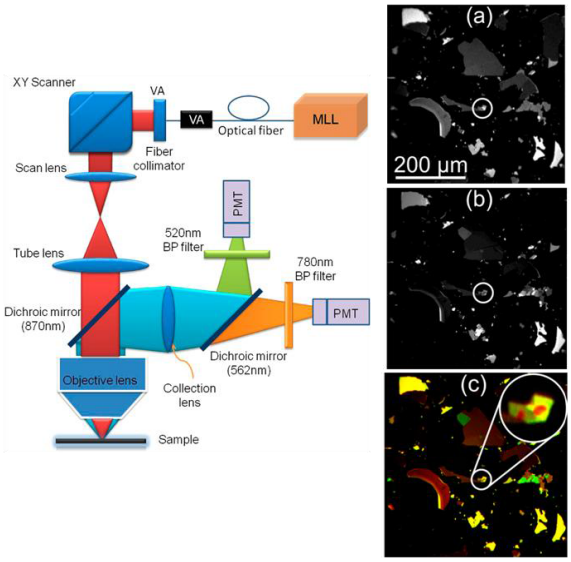

Figure 22. (left panel) Schematic of multiphoton microscope. MLL: mode-locked fiber laser. PMT: photomultiplier tube. VA: Variable attenuator. BP: band-pass filter. (a-c) Multiphoton microscopic images: (a) fluorescence, (b) THG signal, and (c) merged RGB image using fluorescence (red) and THG (green) signal [Publication 6].

A femtosecond (10^{-15} s) pulsed laser beam is used and a dual-axis mirror system for *xy*-plane scanning in the MPM. When the laser is incident to the sample surface through the optics, the backscattered light is split into two branches through a long-pass dichroic mirror which cuts off at 562 nm. Specifically, the second- and third-harmonic emission from the sample can be measured through a 780 ±10 nm and a 520±10 nm bandpass (BP) filter, respectively. Fluorescence arising from two or three phonon excitation can be detected just using the dichroic long-pass filter without the 780 nm BP filter [Publication 6]. A schematic of the MPM and images taken from the MPM for exfoliated graphene on SiO_2/Si are shown in Figure 22. Figure 22(a) and (b) are the images produced by measuring the fluorescence and third-harmonic signals, respectively. Figure 22(c) exhibits the merged RGB image using fluorescence (red) and third-harmonic

signals (green). The area of 450 × 450 μm² scanned in about 5 s. All the graphene (or graphitic) flakes on the sample are clearly visible in the images. A thickness of the layer is identified with the different contrast and colors (as seen in Figure 22(c)). For comparison of characteristics to optical and Raman spectroscopy, the area indicated with a white-circle in Figure 22(c) is focused for further analysis with the THG signal. Figure 23 (a)-(c) show the optical, Raman (FWHM of 2D), and THG image of the MPM for the area indicated. Optical and Raman analysis obviously confirm that the flake is consisted of the regions with the different number of layers.

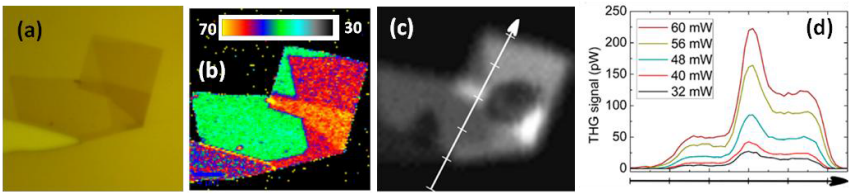

Figure 23. (a) Optical, (b) Raman (FWHM of 2D), and (c) multiphoton of THG images for the graphene flake on SiO_2/Si substrate. The flake corresponds to that marked with white circle in Figure 22(c). (d) THG signal along the arrow in (c) with different excitation powers [Publication 6].

Raman mapping in Figure 23(b) confirms that the area in green (where the FWHM is ~50 cm^{-1}) is 2-3 layers of graphene which is the thinnest part in the flake. The THG collected through the 520±10 nm BP filter discriminates the regions by the different contrasts as seen in Figure 23(c), which corresponds to the optical and Raman image. Figure 23(d) presents the THG signal profile along the line marked in Figure 23(c) with different excitation powers, indicating that the signal is stronger in the thicker area and the intensity is exponentially increased for the laser excitation power.

Although the MPM is not as precise as Raman spectroscopy, it is still a promising technique for a rapid characterization. For instance, multi-photon mapping image for the area of 450 × 450 μm² with a resolution of 1024 lines × 1024 points takes about 5 s, whereas Raman mapping for area of 200 × 200 μm² with 150 lines × 150 points takes about 15 min [Publication 6].

4.4 Electrical measurement

Hall-measurement is well-established for extracting parameters, such as, carrier type, density, and mobility [121]. The results are reliable but a magnetic field is needed. As an alternative, *transfer length method* (TLM), originally

proposed by William Shockley, is also widely adopted for characterizing graphene due to simple test structure as well as measurement process (note that *transmission line model* is also abbreviated as TLM but here it only refers to *transfer length method*). It is straightforward to observe metal-graphene contact resistance and sheet resistance of graphene using only 2-probes. When the gate is combined to the TLM structure, a carrier type and mobility can be practically extracted through the calculations utilizing a classical electric-field induced capacitive model (as described in Chapter 2).

4.4.1 Transfer length method (TLM)

The channels with various contact spacings are the fundamental concept for the TLM as shown in Figure 24(a). When two contacts are ohmic, the total resistance can be expressed as

$$R_{total} = \frac{R_{sh}}{Z} + 2R_C \tag{4.1}$$

where R_{total} is total resistance, R_{sh} sheet resistance, Z width of the channel, and R_C contact resistance.

When total resistances for the channels with the spacings (d_1-d_3) are plotted versus contact space (d) as shown in Figure 24(b), contact resistance for 2 probes ($2R_C$) is directly observed at d=0, meaning R_{total}= $2R_C$.

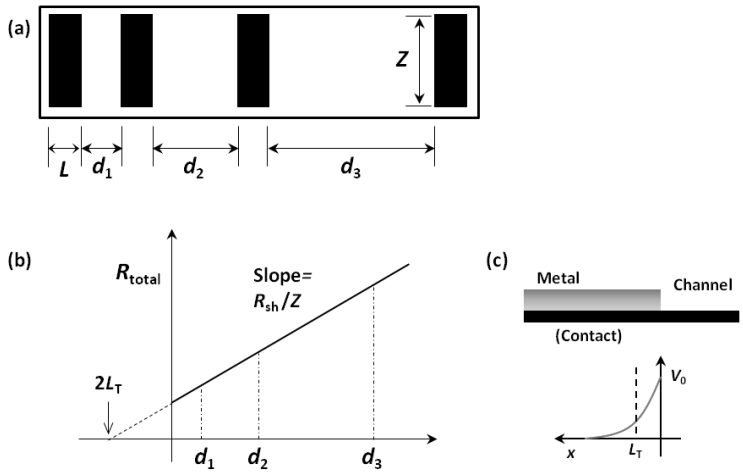

Figure 24. (a) Transfer length method (TLM) test structure and (b) plots (with a trend line) of total resistance as a function of contact space *d*. (c) Schematic of metal-graphene contact and potential distribution along the distance *x*. L_T denotes the transfer length.

With known $2R_C$, the sheet resistance can be extracted by Equation (4.1). Therefore, the slope of the plotted curve also yields the sheet resistance as R_{sh}/Z. The intercept with the extend plot (dotted line in Figure 24) at $R_{total}= 0$ further leads to the so-called *transfer length* (L_T) which is defined as the length over which the most of current transfers from metal to channel or channel to metal. The potential at the contact edge ($x= 0$) is highest and drops nearly exponentially with the distance x as seen in Figure 24(c). Thus, the potential distribution along the x under the contact is expressed as [121], [122]

$$V(x) = V_0 \exp\left(-\frac{x}{L_T}\right) \tag{4.2}$$

$$L_T = \sqrt{\frac{\rho_c}{R_{sh}}} \tag{4.3}$$

where ρ_c is contact resistivity.

Therefore, the "1/e" distance of the potential curve is defined as L_T. The $2L_T$ obtained by TLM (as shown in Figure 24(b)) is valid in a case of conventional semiconductor-metal but not exactly in the graphene-metal contact due to the longer mean free path of graphene and doping effect from metal [122]. Carrier transport in graphene under metal is considered either in ballistic or diffusive. In the diffusive transport limit the mean free path is defined as $l= \pi V_F \tau/2$, where V_F is the Fermi velocity and τ the mean free time. Whereas in ballistic limit the scattering process induced by coupling between metal-graphene only affects the transfer length. The coupling length is described by $l_m = \hbar V_F/\pi\eta$, the so-called *effective coupling length*, where $\hbar$ is the reduced Planck constant and η the metal-graphene coupling strength calculated from Fermi's golden rule [122]. When $l>>l_m$ (ballistic-oriented) and Z is sufficiently long the contact is placed in ideal case due to complete carrier transfer to metal-graphene. In contrast, transmission in metal-graphene is much reduced when $l<<l_m$ (diffusive-oriented). In reality, the transfer length is always in between ballistic and diffusive mode for graphene. Therefore, the effective transfer length can be expressed as $L_{T,\,eff}= \sqrt{l \times l_m}$ [122].

4.4.2 Electric-field capacitive model

When the gate is constructed in the channel of graphene (as depicted in Figure 4(a)), the carrier density and its mobility can be extracted. For simplicity, it is assumed in the model that i) conductivity minimum (σ_{min}) and mobility (μ) are invariable to the drain-source bias, ii) the carrier transport is homogenous

along the channel, and iii) the metal contacts are identical. From Equation (4.1) the total resistance can be expressed $R_{total} = 2R_C + R_{channel}$, where the channel resistance ($R_{channel}$) is calculated using the gate voltage (V_g). Therefore, $R_{channel}$ is derived from Equation (2.11) and (2.12) as

$$R_{channel} = \frac{d}{Z\mu e\sqrt{{n_0}^2+{n_{ind}}^2}} \quad (4.4)$$

where Z is the width, d the length, and n_o the intrinsic carrier concentration, and n_{ind} the induced carrier concentration through the field-effect.
In case, the curve of R_{total} versus V_g is obtained from 2-probe measurement, parameters of n_o, μ and $2R_C$ can be extracted by the data fitting to the model in (4.1) and (4.4) [123].

4.5 Measurement for mechanical property

Single-layer graphene exhibits 1 TPa Young's modulus and 130±10 GPa fracture strength which enables to withstand under the strain exceeding 20% [4], [5]. The exceptional properties is contributed to sp^2 hybridized bonding of carbon atoms in lattice. The robust strength is further useful for applications as a functional component other than electronics, for instance, for an reinforced membrane or a mechanical sensing layer. To utilize the exceptional strength of graphene, however, the layer is demanded to be prepared by free standing with favorably larger scale. Free standing graphene so far have been achieved by few micrometer scale only due to an atomic-thick nature of graphene [4], [74]. In alternative, the membrane can be scaled up to few hundred micrometers when graphene is incorporated to the supporting membrane. The submillimeter scale graphene-alumina membrane have been recently achieved, where a single layer of CVD graphene is embedded to the 100-nm-thick Al_2O_3 layer [Publication 5]. The investigation revealed that the membrane with graphene withstands three times higher differential pressure and twice the strain compared to pure Al_2O_3 membrane. Figure 25 shows the results of a bulge test for two graphene-Al_2O_3 composite membranes comparing with two pure Al_2O_3 membranes. The composite membranes deflects 23-26 μm at 2 bar, corresponding to 0.67-0.69% strain, while the equally thick pure Al_2O_3 membranes destroy already at ~0.6 bar where the deflection reaches 16-20 μm only, corresponding to 0.26% strain. For the composite membranes the effective Young's modulus and the residual stress are in 180 ± 15 GPa and 352 ± 59 MPa, respectively.

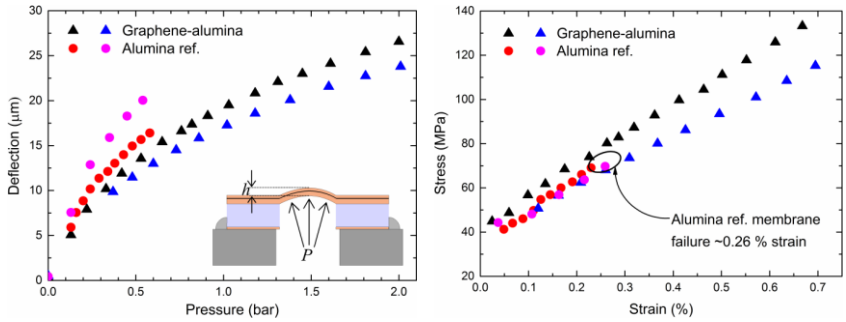

Figure 25. (left) Deflection of set of graphene-alumina composite membranes and pure alumina membranes (reference) versus differential pressure as measured during the bulge test. The composite membranes are intact after being subjected to 2.0 bar whereas the pure alumina membranes are destroyed already at ~0.6 bar. (right) The corresponding stress versus strain for the set of graphene-alumina composite and pure alumina membranes. Figures have been reproduced from [Publication 5].

5. Growth of graphene by rapid photo-thermal CVD

Cost-effective synthesis of graphene in large scale is demanded for industrial purpose. Among the methods known for the synthesis, CVD on Cu is considered as the most promising because it has an ability to produce a uniform single-layer film without size limit [42], [43]. The CVD graphene film is typically synthesized in a tube furnace or thermal reactor with a global heat system. The furnace or reactor utilizing the global heating system results in a longer process due to the slow cooling speed in ambient. In addition, a hot-wall from the global heating in the furnace can introduce contamination into graphene during the growth. Photo-thermal processing, which is also widely utilized for a rapid thermal processing (RTP), has an advantage of the cold-wall process. In the RTP system, a susceptor absorbs incident (infrared) light from the lamps, which is, consequently, heated up, while the side-wall reflects the light. This photo-thermal heat transfer enables the fast heating and cooling cycles due to minimized thermal mass of the susceptor, which significantly reduces the total processing time.

In this chapter, photo-thermal CVD (PTCVD) for graphene synthesis is presented. Using PTCVD, single-layer graphene grown on the Cu foil is demonstrated. The graphene film is characterized by Raman and TLM to identify the quality. The effect of temperature on graphene growth is further discussed by reviewing the experimental results.

5.1 Experimental: growth of graphene on Cu by PTCVD

The furnace for PTCVD was realized by installing an additional gas controlling system (*i.e.* mass flow controllers) to a RTP reactor. Infrared light was utilized as a heat source and a Si wafer was used as a susceptor in the PTCVD process. Prior

to growth, the Cu foil (nominal purity ~ 99.8%) was pretreated with acetic acid to remove copper oxides from the surface followed by annealing at 800 °C for 30 min in a hydrogen (H_2) ambient at atmospheric pressure. The pretreated Cu foil was placed onto a silica plate to prevent the reaction between Cu and the susceptor, *i.e.* the formation of copper silicide. The schematic of the RTP reactor utilized for PTCVD is shown in Figure 26.

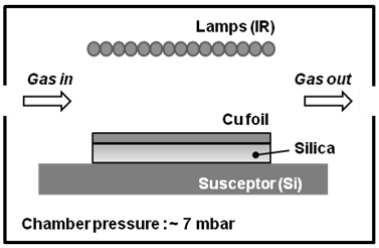

Figure 26. Schematic of the growth setup in the RTP reactor

In the process the Cu foil was pre-annealed for 5 min at 935 °C in hydrogen (H_2) at ~7 mbar to remove any residual oxides on Cu. After annealing, methane (CH_4) was introduced to the reactor to synthesize graphene for 60 s. The flow rate of CH_4/H_2 was 12/3 sccm during the growth and the chamber pressure was kept at ~ 7 mbar. The temperature was controlled by a pyrometer during the whole process (the temperatures mentioned here are the pyrometer readings). To study the effect of temperature on graphene growth, different temperatures (750, 800, 850, 935, and 950 °C) were applied. The highest achievable temperature without deleterious copper evaporation at the process pressure was 950 °C.

For detailed analysis the graphene films synthesized on the Cu foils were transferred onto a thermally oxidized (300 nm) Si substrate using PMMA. The Cu etching was completed in the solution of H_2O_2:HCl:H_2O (1:1:20) (See the section 3.3.2 for the transfer process in detail). The SEM and Raman analysis for all samples are shown in Figure 27. Full coverage of carbon film was identified in all specimens while the wrinkles (red arrows) and few layer flakes (blue squares in Figure 27) which are known as parasitic defects in CVD graphene on Cu were mostly found at the layers grown at 935 °C and 950 °C. The few-layer flakes with the nuclei were also clearly found at those samples (grown at 935 °C and 950 °C) as seen in insets of Figure 27. To evaluate the quality of the films, all the samples were probed by Raman spectroscopy (WITec alpha-300R) using a 532-nm Nd-YAG green laser. The results are shown in Figure 27 (right panel). The Raman spectra of the samples correspond to the SEM images in the left panel of Figure 27.

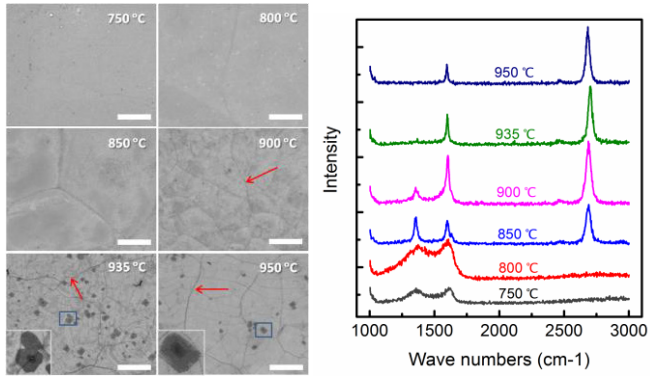

Figure 27. (left panel) SEM images of the transferred graphene layers on the SiO_2/Si substrate. The figures in the images denote the growth temperature for the graphene samples. The red arrows point the wrinkles and the blue squares indicate the few-layer flakes. Enlarged images for each of the few-layer-flakes designated by the blue squares are shown in the low-left of the images for 935 °C and 950 °C. The scale bars are 4 μm. (right panel) Raman spectra corresponding to samples shown in the SEM images.

It is clearly found that the intensity of 2D-band (around 2690 cm^{-1}) is distinctly stronger while that of D-band (around 1350 cm^{-1}) which represents disorder or defects is weaker as the growth temperature is increased. No prominent 2D-peaks were detected in the layers grown at 750 °C and 800 °C, implying that the films are composed with amorphous carbon although the layers were uniform and continuous. The G-band is to be sharpened as the growth temperature is increased, indicating that the amorphous layer evolves to a crystal layer. For further analysis, the samples were scanned by Raman spectroscopy to produce a detail map. The scanning was performed with 120 points × 120 lines for the area of 25 × 25 μm^2. Figure 28 shows Raman mapping images presenting the intensity ratio of 2D to G-band (I_{2D}/I_G) (a-d), D to G-band (I_D/I_G) (e-h) and the full width at half maximum (FWHM) of 2D-band (i-l) for the samples grown at 850 - 950 °C. The images are arranged by the growth temperature in each column. Figure 28(a-d) and (e-h) shows that the level of I_{2D}/I_G is increased while that of I_D/I_G is decreased. Therefore, the quality of the graphene layer is optimized to the defect-less crystallized single-layer when growth temperature approaches 950 °C. Here the crystallized single-layer can be expected when the ratio of I_{2D}/I_G is in 1.5-2.5 and I_D/I_G is less than 0.2 (as discussed in Chapter 4).

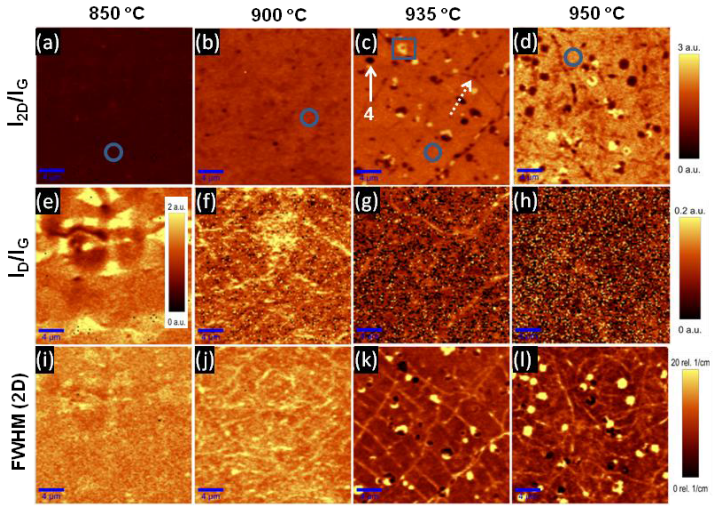

Figure 28. Scanned Raman images for the graphene samples presenting (a-d) intensity of 2D/G-band, (e-h) D/G-band and (i-l) FWHM for 2D-band. The images are arranged by the growth temperature in columns. Image scales in the right apply for the entire row except for (e). The scale bars are 4 μm.

Figure 29 shows statistical histograms of Raman mapping shown in Figure 28. From the analysis, the defect-less single-layer graphene is confirmed to be covered over 90% in the samples grown at 935 °C and 950 °C while the amorphous film is dominantly consisted in the sample grown at 850 °C. The reason that columns of I_D/I_G in the level of 0.2~0.4 for those grown at 935 °C and 950 °C are placed over 50% shown in Fig. 29(b) is due to the wrinkles which accompany the weak D-band. The distributions of FWHM of 2D band in Figure 29(c) also indicate that the graphene films grown at 935 °C and 950 °C having much narrower 2D peaks are consisted with more sp^2 hybridized carbon lattice.

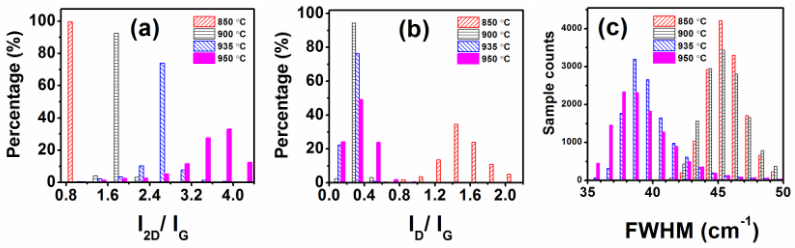

Figure 29. Statistical histogram distributions of (a) intensity ratio of I_{2D}/I_G, (b) I_D/I_G, and (c) FWHM of the 2D-band for the samples grown at 850, 900, 935, and 950 °C. Data was extracted from the Raman area scanning showing in Figure 28.

5.2 Characterization of graphene for electrical properties

To investigate the influence of growth temperature on the electrical properties of graphene, TLM structures were fabricated on the samples shown in Figure 27-29. All patterns in device fabrication were completed using conventional e-beam lithography. The graphene channel was defined by oxygen (O_2) plasma etching and the metal contacts of Ti/Au (3/45 nm) were completed by e-beam evaporation. The fabricated TLM structure is shown in Figure 30 (left panel). Channel width is 10 μm and length of graphene varies from 1 to 8 μm, having a step in the double as 1, 2, 4, and 8 μm, respectively.

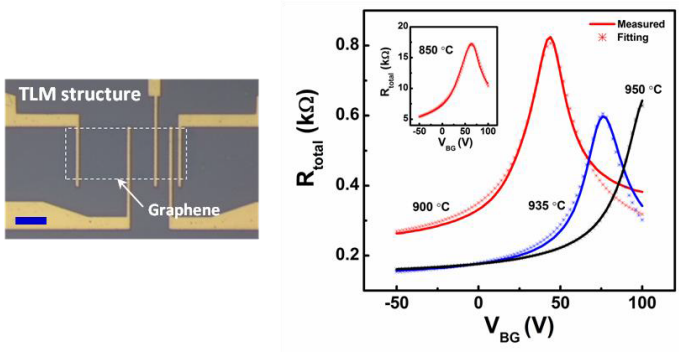

Figure 30. (left panel) Optical image of TLM structure having 4 different channel lengths (1, 2, 4, and 8 μm) with width of 10 μm. The scale bar is 5 μm. (right panel) Measured total resistances of the samples grown at different temperatures as a function of the backgate voltage at room temperature. The plots with symbols denote fitting values. (inset) The samples grown at 850 °C.

For each of the 1 μm channels in the TLM structures, the currents through the channel were first monitored with varying the backgate voltage (V_{BG}). The measured total resistances (R_{total}) as a function of V_{BG} are shown in Figure 30 (right panel). The points of the minimum current flow, *i.e.* the Dirac point (V_{Dirac}), were found between 40 V to 100 V of V_{BG}. The different positions of Dirac points can be placed up to the different condition of doping level and contact resistance. All measurements were carried out using HP 4155A Semiconductor Parameter Analyzer at room temperature.

In device analysis, mobility (μ) and contact resistance (R_C) for all devices were approximated by fitting measured data to the model described in Equation (4.4). Calculation for the induced carrier concentration varied with V_{BG} follows

$$n(V_{BG}) = \frac{\varepsilon_0 \varepsilon_r (V_{BG} - V_{Dirac})}{te} \qquad (5.1)$$

where ε_0 and ε_r is the permittivities of free space and dielectric medium (SiO_2), respectively, V_{Dirac} the gate voltage at the Dirac point, t the thickness of dielectric medium and e the electric charge.

The fit curves are presented as dotted-lines in Figure 30 and the parameters extracted are listed in Table 2. In calculation, ε_r = 3.9 and t= 300 nm were applied.

Table 2. Parameters extracted from the curve-fit using the model of the Equation (4.4) and (5.1)

Growth Temp.	n_0 (10^{11} cm^{-2})	μ (cm^2/V·s)	$2R_C$ (Ω)
800 °C	100	1.5	4×10^4
850 °C	16.5	252	251
900 °C	8.34	1224	194
935 °C	7.07	1805	116
950 °C	6.81	1843	130

The results in Table 2 show that higher mobility is exhibited with higher temperature in growth. The extracted values by the fitting method for the carbon films grown at lower temperature at 800 °C have large deviation from the real values since they do not behave as an ambipolaric linear-dispersed conductor, indicating that the Equation (4.4) and (5.1) are practically invalid. It is also noted that the parameters extracted by the fitting method are only valid when mobility and contact resistance are assumed to be constant in a hole and electron transport region and, thus, independent from the gate-electric field. The real mobility is, however, affected by the gate and highest near the Dirac point (but not in the carrier puddle region) while lowest in highest carrier concentration, far from Dirac point.

All TLM structures were measure at V_{bias}= 0.1 V to produce the relation between total resistance (R_{total}) and the channel length (d). The different gate voltages, such as, $V_{BG} = V_{Dirac}$, V_{Dirac} - 30 V, V_{Dirac} - 60 V, and V_{Dirac} - 150 V were also applied at the same time. The all plots for the samples are shown in Figure 31. Once $2R_C$ is known, sheet resistance can also be calculated from the relation of $R_{total} = \rho_{sh}(d/Z) + 2R_C$, where ρ_{sh} is the sheet resistance in the channel. The $2R_C$ and ρ_{sh} obtained from TLM measurement are presented in Table 3. The values of sheet resistance are the mean values of those extracted from the 4-different channels. It is noted that the extraction of the contract resistance for the sample grown below 850 °C by the use of TLM is meaningless since channel resistance is much higher than the contact resistance, where $2R_C$ is, thus, estimated almost to zero.

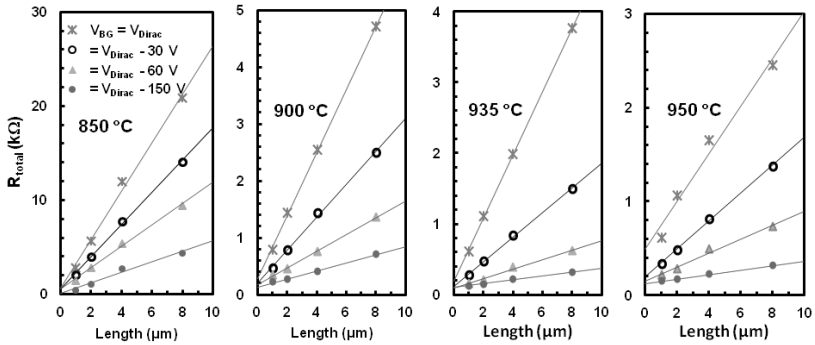

Figure 31. Total resistances (symbols) with the different back-gate voltages (V_{BG}) along the channel length for the graphene samples grown at different temperatures. The all measurements were carried out at room temperature.

The results in Table 3 show that both contact resistance and sheet resistance are lower with the higher growth temperature. It indicates that graphene quality is improved from minimizing the crystal defects at higher temperature. Note that the reason the contact resistance of the device for 950 °C is slightly higher than that for 935 °C may be due to the different level of impurities on graphene which can be induced during the device fabrication process. As shown in previous study [122] contact resistance were maximized when the V_{BG} approaches the Dirac point. In this experiment, the lowest sheet resistance, 260 Ω/□, was found on graphene grown at 950 °C with the V_{BG}= V_{Dirac} - 150 V (n ~1 × 10^{13} cm^{-2}). When comparing parameters extracted by the curve-fit (Table 2) to those measured through TLM (Table 3), the both values for $2R_C$ are similar for the samples grown above 900 °C.

Table 3. Contact resistance (2Rc) and sheet resistance obtained from TLM measurement. The values of sheet resistance are the mean values with the errors for the 4-different channels.

Growth Temp.	$2R_C$ (kΩ)				Sheet resistance (kΩ/□)			
(V_{BG} =)	V_D-150 V	V_D-60 V	V_D-30 V	V_D	V_D-150 V	V_D-60 V	V_D-30 V	V_D
850 °C	~0	~1	~1	~1	5.7 ± 1	8.9 ± 1.7	14.8 ± 2.2	23.4 ± 5.5
900 °C	0.18	0.19	0.20	0.22	0.51 ± 0.15	1.43 ± 1.6	2.89 ± 0.18	5.79 ± 0.26
935 °C	0.10	0.10	0.12	0.20	0.27 ± 0.03	0.64 ± 0.08	1.72 ± 0.09	4.39 ± 0.08
950 °C	0.12	0.14	0.20	0.51	0.26 ± 0.04	0.78 ± 0.09	1.44 ± 0.08	2.26 ± 0.78

It is well known that the TLM is only valid when carrier transports in the interface of metal-graphene contact are entirely diffusive. It indicates that graphene should behave as a linear resistive material and the carrier mean-free path in the contact should be smaller than metal-graphene coupling length (see

detail in the section 4.4.1). At room temperature, the carriers in graphene are expected to travel diffusively [55]. In addition, each of the contact resistances should be equal for valid TLM analysis. As shown in Figure 31, the linear fit of total resistances along the channel length implies that resistances on the contacts of the 5 terminals are almost identical. Owing to the zero bandgap of graphene, the metal-graphene contacts are typically expected to be ohmic.

6. Fabrication and characterization of graphene field-effect devices

Recently, exploiting graphene field-effect transistor (GFET) [7], [10] various analog device functions such as the frequency mixer [124]–[126] have been demonstrated. Such devices are expected to have a significant role in radio frequency (RF) electronics. Recent development of process for cost-effective synthesis of graphene in larger scale by CVD [43], [44], [127], [128] enables wafer-scale integrated circuits (ICs). This is viable because fabrication of graphene-based device is compatible with conventional semiconductor technology. Despite of the existence of the off-state current, graphene is still attractive as a material for logic components since it can be easily doped by chemicals or an external electric field. For instance, a device performing as an inverter can be achieved with two complementary GFETs as demonstrated at low temperature (3 K and 77 K) [14]–[18] as well as at room temperature [19]–[23], [Publication 2]. Recent GFETs have further achieved cascading inverter operations with the reasonable levels of voltage gain [21], [22] by employing ultra thin gate dielectric.

Beyond the transistor functions, a device utilizing characteristics of carrier transport in 2-DEG has been also proposed and demonstrated. It is intriguing because the device utilizes the nonlinear effect typically arising in 2-dimensional regime and, thus, is not strongly affected from the zero bandgap nature. The phenomena have been already well-established in the previous studies using heterojunctions of III-V semiconductor [24]–[29]. Recently, nonlinear behaviors exhibiting like an electrical rectification have been demonstrated using exfoliated [36]–[38], [Publication 3] and SiC graphene [39], [40] in three-terminal junctions (TTJ) structure.

In this chapter, room-temperature graphene field-effect devices operating as an inverter as well as rectifier are introduced. Complementary GFETs achieved by associating the separated local gates present the device ability to function as a

highly tunable inverter. Nonlinear behavior in 2-dimensional regime is demonstrated; exhibiting rectification. This is realized through three-terminal T-branch junction (TBJ) device. Instead of ballistic-limited nanoscale structure, the devices having tens of micrometer scale is presented in experiment for diffusive operation. Diffusive device gives more freedom in design and fabrication and is, accordingly, beneficial for practical applications.

6.1 Local gate controlled graphene field-effect device performing as an inverter

A complementary configuration in GFETs can be achieved by either current-induced cleaning of one of the graphene channels [15] or by directly applying a high voltage to the power source (V_{DD}) of the device [16], [17]. In the former, the Fermi level shift is caused by removal of (ambient) contamination, and the latter exploits the effect of charge coupling between the gate and channel. However, to maintain the difference in charge concentrations between two transistors, a rather high V_{DD} needs to be applied since the charge coupling is strongly effective when $V_{DS} \geq 2V_{GS}$ [129], where V_{DS} and V_{GS} are the potential difference from the drain to source and the gate to source, respectively. On the other hand, a complementary function can be also achieved by the asymmetric dielectric layer (thickness) for the top gate to realize a different level of charge coupling between two transistors [18]. In this kind of configuration, however, the difference in doping levels of two transistors is strongly dependent on the asymmetric insulator thickness. For practical applications, a device operating at low supply voltage V_{DD} should be considered to reduce power consumption due to the existence of off-state current. Therefore, a device with the individual control of the doping for each of the channels through the separated local gates will be effective as the device can operate in low V_{DD}. The tunable function enables the device to be switchable between inverter (p-n FETs) and voltage control resistor operation (n-p FETs).

6.1.1 Device fabrication

Two separate Al electrodes for the local backgates were first patterned on the Si/SiO_2 substrate. The electrodes were isolated by a 25-nm-thick Al_2O_3 layer which was completed through atomic layer deposition (ALD). A single-layer graphene film synthesized on the Cu foil by PTCVD [Publication 4] was transferred onto the Al_2O_3 layer. Next, graphene channels were defined by O_2 plasma

and followed by 2/45 nm of Ti/Au contacts on graphene. For a topgate dielectric, a 25-nm-thick Al_2O_3 layer was deposited by ALD on the graphene channels. A thin Al film (nominally 1.0 nm) was used as a seeding for Al_2O_3 growth on graphene. The Ti/Au (2/45 nm) metal fingers for the top-gate were finally formed. An optical microscope image (top view) and a cross-sectional schematic of the final structure of two GFETs are shown in Figure 32 (a) and (b). Length and width of the graphene channel are 2 μm and 54 μm, respectively. As shown in Figure 32(c), two GFETs are connected in series as in a conventional logic gate inverter (such as the complementary metal-oxide semiconductor, CMOS). For the device operation, the source in FET_1 was connected to the power supply (V_{DD}), whereas FET_2 (V_{SS}) was grounded. Back-gates 1 (BG_1) and 2 (BG_2) were connected to a voltage supply to control the channel doping.

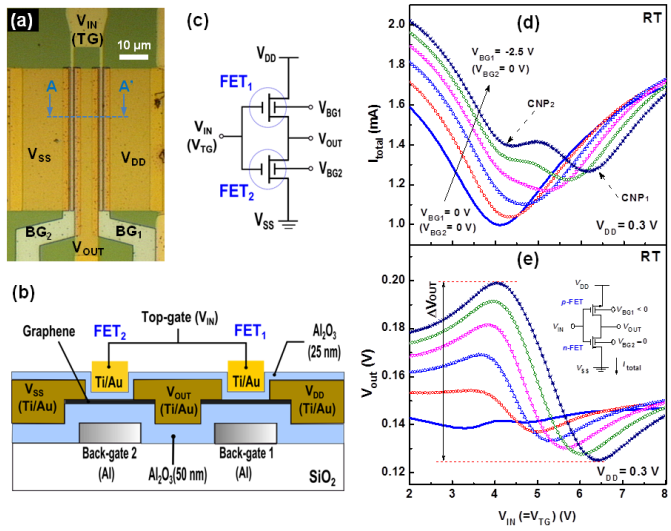

Figure 32. (a) Optical microscope image of the complementary graphene inverter. The length and width of a single channel is 2 μm and 54 μm, respectively. The active channel length under the top-gate (TG) is 1 μm. (b) Cross-sectional schematic of the device depicted along the A-A' line denoted in (a). (c) Equivalent circuitry for the inverter operation. (d-e) DC characteristics of the inverter measured at room temperature: (d) Total current (I_{total}) flowing through the device and (e) voltage transfer curves showing output voltage (V_{OUT}) as a function of input (V_{IN} = V_{TG}) with 0.3 V of the operating voltage (V_{DD}). Different colours with symbols in the curves indicate a different back-gate voltage of BG_1 (V_{BG1}, from 0 to -2.5 V) at a fixed voltage of BG_2 (V_{BG2}= 0V). Solid lines without symbol denote the results at V_{BG1} = V_{BG2} = 0 V. The CNPs for the FET_1 and the FET_2 at V_{BG1} = -2.5 V (and V_{BG2} = 0 V) are indicated by dashed arrows in (a).

6.1.2 Device characteristics

In device operation, low V_{DD} (0.3 V) compared to the range of input voltage (ΔV_{IN} = 6 V) was applied to minimize the channel doping effect (causing the

Dirac point shift) due to the potential difference between the gate voltage (V_G) and channel bias voltage (V_{DD}). Figure 32(d) shows the total current through the device (I_{total}) as a function of the input voltage (V_{IN}) with the various local back-gate voltages (V_{BG}). The charge neutrality point (CNP), the Dirac point, is found at about V_{IN} = 4 V without V_{BG}. The single CNP for two FETs in series indicates that the doping levels of both channels are nearly identical. The PMMA residues and moisture are expected to result in slight p-type doping of the graphene channel [11], [130]. As expected from the previous studies [12], [13], when negative V_{BG} is applied for the FET_1 (for example, V_{BG1} = -1 V), the CNP split in two due to the shift of the doping level of the FET_1. At V_{BG1} = -2.5 V, the CNP of the FET_1 is further shifted, but both of the FETs are in the p-type region. At V_{BG1}= -2.5 V and V_{BG2}= 0 V, the CNPs for the FET_1 and FET_2 (CNP_1 and CNP_2) are found around 4.3 V and 6.3 V of the input, respectively. This implies that the device configuration of the FETs is p-n by the wider CNPs split. The CNP_2 can be further shifted towards the n-doping region by applying a positive V_{BG2}. It is noted that the total on/off ratio of the device is decreased when the two CNPs are further split apart. Figure 32(e) shows the voltage transfer curve, *i.e.* the output characteristics of the device as a function of the input voltage. The output voltage in this configuration can be considered as $V_{OUT} = V_{DD} / (1+R_{FET1}/R_{FET2})$, where R_{FETi} is the total resistance of a single transistor. With the CNPs split by applying negative V_{BG1}, output inversion for the input occurs as in a typical p-n FET inverter. In device performance, it is normally expected that the output voltage is larger than $V_{DD}/2$ when the V_{TG} is in low input status due to $R_{FET1} < R_{FET2}$ (and vice-versa when V_{TG} is in a high input status). As seen in Figure 32(e), a wider CNP split causes larger ΔV_{OUT} ($\Delta V_{OUT} = V_{OUT}^{Max} - V_{OUT}^{Min}$), which results in an enhancement of the voltage gain |A| (= $|dV_{OUT}/dV_{IN}|$) at the same time. |A| can be practically improved further by utilizing the thinner dielectric layers. It is beneficial for the device to operate with low V_{DD}, because complementary configuration can be achieved by external electrostatic doping. As a result for an inverter, at V_{DD}= 0.3 V, ΔV_{OUT} increased from -5 to 80 mV by applying V_{BG1}= -2.5 V (V_{BG2}= 0 v) although the gain |A| is low as 0.04 as seen in Figure 32 (d-e). Inversion characteristics of the device with the p-n type (V_{BG1}= -2.0 V, V_{BG2}= 0 V) were further analyzed with higher V_{DD}. Figure 33(a) shows the characteristics of the inverter device with various steps of V_{DD} (from 0.1 to 4 V). |A| and ΔV_{OUT} were increased as a function of V_{DD} as seen in the Figure 33. It shows that the device performance can be improved in the low V_{DD} region through enhancement of voltage gain by applying the local back-gate, as seen in Figure 33(b). One major benefit of the utilized device structure is that the ratio of $\Delta V_{OUT}/V_{DD}$ is practically invariable at ~25 %, regardless of the level of V_{DD}, implying that the

doping of the channel is not strongly affected by the bias voltage V_{DD} but determined dominantly by the back-gate bias. However, the back-gate effect is minimized at high V_{DD}, for example, in the region of $V_{DD} > V_{BG}$, due to the additional charge coupling dominated from the potential gap between V_{DS} and V_{GS}.

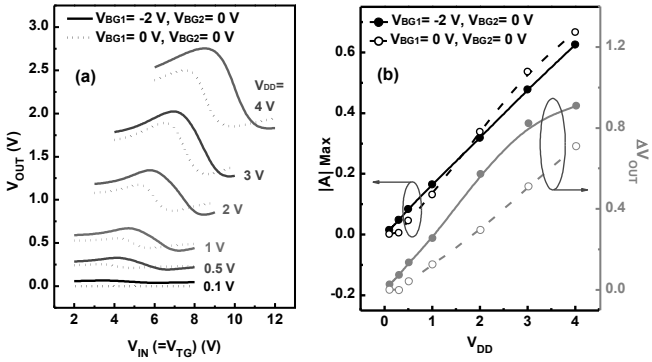

Figure 33. (a) DC voltage transfer characteristics of the inverter device at V_{BG1} = -2.0 V and V_{BG2} = 0 V (p-n FETs configuration) with various operating voltage V_{DD} (from 0.1 to 4 V). (b) The maximum voltage gain $|A|_{Max}$ (left axis) and ΔV_{OUT} (right axis) as a function of V_{DD}. The dashed lines denote the device characteristics with zero back-gate biases.

6.2 Three terminal junction graphene rectifier

Charge carrier transport in a 2-dimensional electron gas (2-DEG) has been widely studied for the past decades to exploit its nonlinear properties arising in the ballistic regime [24]–[34], [131], [132]. Utilizing three-terminal junction (TTJ) devices, the nonlinear characteristics which exhibit as an electrical rectification has been demonstrated. Ballistic nanoscale TTJs are typically fabricated through TBJ structures as the center branch and structural symmetry are conveniently achieved in device fabrication. Rectification arises at the center of the channel due to the conductance difference between the left and right channels when two terminals are anti-symmetrically biased (the so-called *push-pull application*). It is because of the change of chemical potentials at the contacts by the biased voltage, which results in the shift of the potential symmetry point in the channel [33]. The nonlinear ballistic behavior can be generally explained by Landauer-Büttiker formalism [25], [33], [34].

For the nanoscale TBJ in III-V semiconductors, when the scale increases, the rectification is receded as expected due to a further shifting of the channel to-

wards diffusive regime [31], [131]. However, the rectification has been observed when the push-pull voltage (V_o) increases to the high enough values even at the micrometer-scale junctions [131]. At the high V_o, for example, $V_o > 1$ V, the process can be understood so that the carriers associated with phonons are thermally emitted, losing their velocity during travelling and they, consequently, can be accumulated near anode (a positive-biased contact in electron region and vice-versa in hole region). The accumulation yields high resistivity resulting in the stronger voltage drop in the channel [131], [133], enabling rectification even in the long-channel diffusive regime. This indicates that the sign of the potential shift is strongly dependent on the type of charge carriers. In TTJ, consequently, positive output is generally expected in the hole region (as a positive rectification) and negative in the electron region (as a negative rectification) [41]. Conventional III-V semiconductor based TBJ devices [30]–[32] show negative rectifications as they have only electrons as charge carriers. Exceptionally, rectification whose sign is determined by the dimension and geometry of the junction scale has also been reported [133]: unexpectedly the rectification is changed from negative to positive when channel width of the TBJ is over ~250 nm (but no more than few micrometers). The origin of geometry dependent rectification has not been confirmed, but may be associated with non-identical potentials at the contacts [133] [Publication 3]. Nevertheless, the sign of rectification is predetermined by physical device parameters and is not controllable during device operation. Graphene based devices, on the other hand, exhibit both positive and negative rectifications by the gate field control [36]–[38], [Publication 3].

6.2.1 Nanoscale TBJ on exfoliated graphene

For ballistic transport the graphene TBJs are typically fabricated in nanoscale (channel width ~ 50- 300 nm) [36]–[41]. As it has crystallized single grain structure, exfoliated graphene is preferentially utilized for the TBJ. In this experiment, the nanoscale TBJ was fabricated on mechanically-exfoliated single-layer graphene which was prepared on a SiO_2/Si substrate. The p-doped silicon substrate was used as a global back-gate contact in electrical measurements. 5/45 nm of Ti/Au metal contact were formed by e-beam evaporation. Afterwards, the TBJ was defined by O_2 plasma etching. Length and width of the constricted channel between the right and left were 600 and 200 nm, and for the center branch 300 nm and 100 nm, respectively. All device patterns at the fabrication steps were completed using conventional e-beam lithography technique. The device of TBJ fabricated is shown in the inset of Figure 34 (a).

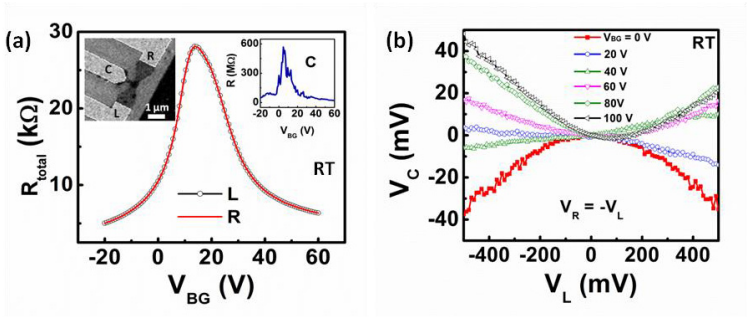

Figure 34. (a) Total resistance (R_{total}) as a function of the back-gate voltage (V_{BG}) when only V_L is applied (V_R= 0 V). The resistance curves for the left (L) and right terminal (R) are overlapping. The inset in the upper right corner shows the resistance of the center terminal. A SEM image of the TBJ structure is shown in the upper left corner. (b) Voltages measured at the center branch as a function of the push-pull bias voltage (V_L =V_0, V_R= -V_0) with the various back-gate voltages.

The device was configured with the voltage sources for left and right terminals and output for center terminal. In device analysis, the TBJ device was first characterized by measuring the total resistance (R_{total}) as a function of the backgate voltage (V_{BG}) as seen in Figure 34(a). The Dirac point (V_{Dirac}) was observed at near 16 V of the back-gate. Next, to investigate the behavior of the TBJ the device was electrically floated by applying a push-pull application while the output voltage (V_C) at the center branch was monitored. According to the classical resistive transport, the electrical potential at the center point of the channel is expected to be zero in a push-pull configuration ($V_L = V_o$ and $V_R = -V_o$, where V_o is the bias voltage). However, a certain level of the output V_C was observed in this TBJ device regardless of the sign of bias voltage as shown in Figure 34(c). To examine further behaviors related to the charge carrier type and concentration, the device was operated with various gate voltages. As seen in Figure 34(b), symmetric rectified V_C curves as a function of V_o were detected. The negative output arose for the holes and positive output for the electrons while it becomes almost zero near the Dirac point. The rectification reaches around 4% for the total input.

The rectifications in graphene TBJ are obvious even at room temperature. However, the polarity of rectification is opposite from those appearing at conventional III-V semiconductor based TBJs. The origin of the nonlinear behavior of this TBJ can be deduced from the metal-graphene interaction at the contact. Regarding the metal-graphene interaction, theoretical calculations have shown that graphene is chemisorbed on titanium (Ti) surface and this strong binding interaction perturbs the electronic band structure of graphene

significantly. Consequently, graphene under the metal would be n-type [122]. However, the works along with many other experimental results [134]–[137] show p-doping of graphene with Ti. The difference between the model and experimental results might arise from the fact that the contaminants, e.g., moisture, oxide, or residue of resist, at the metal-graphene interface modify the work functions and alter the interaction [138]. Nevertheless, when Ti and graphene are put into contact, p-doping of graphene under the metal is realized, *i.e.* the electrons on graphene are transferred to the metal. Since the density of states of graphene is much smaller, the Fermi level of graphene is significantly changed (downshifted). As an equilibrium state is reached by the charge transfer, a dipole layer with a finite width is formed creating a potential step ΔV at the interface as shown in Figure 35(a).

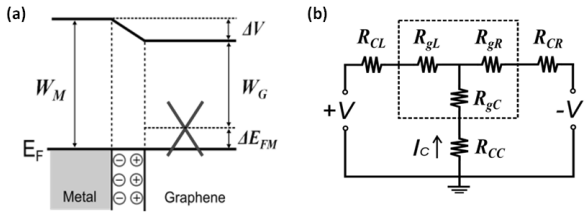

Figure 35. (a) Schematic of the energy band diagram for the metal-graphene interface. W_M and W_G represent the workfunction of metal (titanium) and graphene, respectively. ΔV is the built-in potential difference and ΔE_{FM} is the Fermi level shift of graphene under the metal. (b) Simplified equivalent circuitry for the p-doped graphene TBJ device operation. R_{CL}, R_{CR} and R_{CC} denote the contact resistance in the left, right and center terminal, respectively. R_{gL}, R_{gR} and R_{gC} in the dashed box are resistances of each of the graphene channels.

When the bias voltage is applied, it is expected that carrier transport from metal to graphene and graphene to metal are not equal due to the potential step, ΔV. For p-doped graphene, probability of electron transmission from metal to graphene can be slightly higher than that from graphene to metal. Therefore, TBJ shows always positive current flow through the center branch with a push-pull bias application regardless of the sign of the bias voltage since total contact resistance in left (R_{CL}) and right (R_{CR}) are not equal. For n-doped graphene, behavior of charge carriers transferring though the metal-graphene interfacial barrier is altered, *i.e.* transmission from graphene to metal is slightly higher than that from metal to graphene. Figure 35(b) shows simplified equivalent circuit for the p-doped graphene TBJ operation. Note that graphene in each of the channels is simply considered as linear resistive component (R_{gL}, R_{gR} and R_{gC}) as described in Figure 35(b). Additionally, the metal-graphene contact at the center terminal does not play a significant role due to relatively small potential difference between the center point of the L-R channel and the

terminal C, implying that R_{CC} is not affected by the push-pull bias application. Therefore, the center branch can be considered to act merely as a probe.

6.2.2 Microscale TBJs on CVD graphene

Although nanoscale TBJs are very intriguing from an academic point of view and are promising for nanoelectronics, ballistic operations are impractical for flexible and transparent application owing to the strict nanoscale size requirements. In lithographically patterned nanostructures like nano-ribbons, carrier mobility is rather degraded [139], [140] due to additional scattering events associated with the imperfect edges. Temperature and substrate induced scattering also limit the device viability. Moreover, mobility is further degraded in the short channels by the high bias induced doping effect [141], [142]. Accordingly, the graphene nano-TBJs have showed ~ 5-12% maximum efficiency (V_{OUT}/V_{IN}) at room temperature [37]–[40]. In addition, the nanoscale devices display rectification curves that are asymmetric, which lowers the average value of the waveform.

Large-scale graphene prepared by CVD [42]–[44], [127] has the potential to deliver true monolithic integrated circuits (ICs) as one continuous single-layer graphene film can be utilized as a channel, gate, interconnect, and even as passive components such as resistors and planar waveguides [143]. All-graphene architecture would also significantly reduce the number of graphene-metal interfaces. Therefore, it is worth studying the behavior of devices fabricated utilizing CVD graphene for practical applications.

Field-effect transistors were fabricated with graphene synthesized by PTCVD [Publication4]. To assess the three-terminal based operation, the devices were first structured with a metal as the center probe crossing the whole channel as shown in Figure 36(a) and (b). CVD graphene was utilized also as a gate electrode to replace the typically used metal electrode. Resistivity of the gate is not significant here since only direct current (DC) is employed through the gate in the rectifier device characterization, but for high frequency applications the gate resistivity needs to be considered to avoid time delay of the signal. Channel length and width are 28 μm and 54 μm, respectively. The channel length is used to refer to the whole graphene channel between left and right metal terminals. The width of the center metal probe is 0.5 μm. For device operation the left (L) and right (R) terminals were utilized for the input bias, and the center terminal (C) for the output signal detection (as shown in Figure 36(a)). To identify electrical properties of the graphene channel, the right terminal was biased (and

the left was grounded) and the current flowing through the whole channel was monitored while the gate field was varied. As depicted in the inset of Figure 36(c), the configuration is similar for inverter operation [21] [Publication 2] as one terminal is connected to power supply (V_{DD}) and the other is grounded (GND). Figure 36(c) shows measured total resistance (R_{total}) as a function of the topgate voltage (V_G), presenting that the channel layer is slightly p-doped. Through the curve-fitting to the measured data [123], carrier mobility (μ) and intrinsic carrier density (n_o) for the channel were extracted as ~2250 cm²/Vs and ~6 ×10¹¹ cm⁻², respectively.

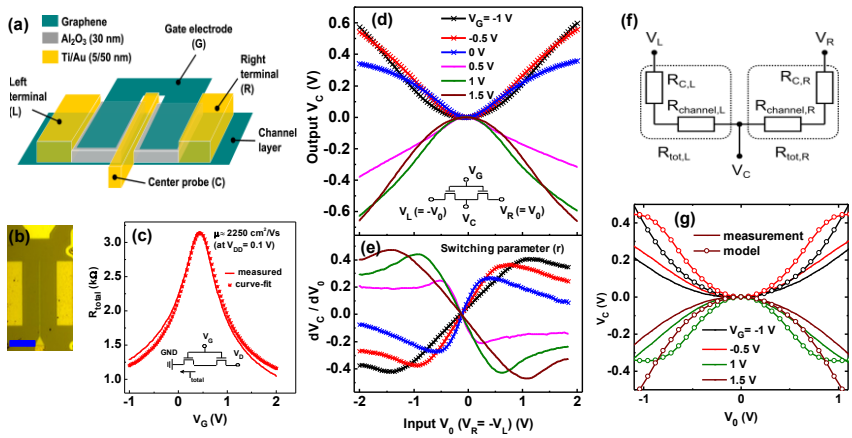

Figure 36. (a) Schematic and (b) optical image of a three-terminal graphene field-effect device. Scale bar is 20 μm. (c) Total resistance as a function of the gate voltage. Plots with the symbol are the values fitted to the measured values (solid line). (d-g) Rectifier operation: (d) output voltages detected at the center probe for push-pull input bias V_0 under the different gate fields. V_0 is equivalent to V_R when the anti-symmetric input V_L is applied to the other terminal. (e) Switching parameters r ($=dV_C/dV_0$) corresponding to the voltage transfer curves in (d). Lines with symbols denote the outputs detected in the hole transport region. (f) Circuit diagram used to model the rectification characteristics. (g) Comparison of measured (solid line) and calculated (solid lines with symbols) rectification curves. Diagrams in the panels depict electrical configuration for each measurements.

For nonlinearity analysis, the electrical configuration of the channel was setup for push-pull application (V_L= -V_R). The schematic of the electrical configuration is shown in the inset of Figure 36(d). During push-pull voltage sweep, various gate voltages from -1 to 1.5 V were applied. Figure 36(d) shows the output voltages detected at the center branch with different gate voltages in the push-pull application. The output V_C clearly increases when the input $|V_o|$ (V_R = V_o and V_L= -V_o) is increased and is unidirectional regardless of the sign of the input, exhibiting electrical rectification. Moreover, the output levels and signs are strongly dependent on the carrier type. In the region of -1 V<V_o<1 V the outputs are maximized at V_G= -0.5 V (hole transport region) for positive rectification and

at V_G= 1 V (electron transport region) for negative rectification, respectively. In contrast, in the higher drain-source bias region, for example, V_o> ±1 V at V_G= -0.5 V and 1 V, the output starts to saturate as the curvature becomes non-parabolic, which we attribute to the degradation of the conductivity of graphene in the high-field bias regime due to charge trapping in SiO_2 [141], [142]. The rectification characteristics are evaluated with a switching parameter r (= dV_C/dV_o) as it relates to the efficiency, reveals the saturation points, and displays if the rectification has a parabolic nature. The results in Figure 36(e) show that the parameter r is increased linearly with the bias V_o in the range of -1 V< V_o< 1 V. The linear range corresponds perfectly to the parabolic rectification curve ($V_C \propto V_o^2 \rightarrow r \propto 2V_o$). Maximum $|r|$, about 0.45, is observed at around V_o= ±1 V. By further increasing the gate electric field, the point of $|r|_{Max}$ is shifted toward the higher V_o region without significant change in the magnitude. It indicates that the V_C is maximized with lowest carrier density near the Dirac point (V_{Dirac}), although it becomes almost zero at Dirac point. The results are intriguing when considering that rectification is achieved while using an invasive metal center probe to detect the center potential (V_C). In traditional nanoscale T-branch devices the rectification is explained typically through the ballistic junction effect associated with the center branch, which is not valid here as there is no such T-branch junction. Furthermore, device having a dimensions of tens of micrometers on SiO_2/Si operates in diffusive regime at room temperature.

To understand the rectification characteristics of large scale CVD graphene device a diffusive model is employed to explain, instead of ballistic (or quasi-ballistic) theory applied for the nanojunction rectifiers. In the case of thin gate dielectrics the effective electric field is affected by the source-drain voltage [129], [144]. The gate is floating during push-pull application and, consequently, the channel is associated with the self-gating from the biases with the magnitude of ±V_o. Therefore, for the push-pull bias input the effective gate voltages for the left and right channels can be expressed as

$$V_{eff,L} = V_G - V_{Dirac} + V_0 \tag{6.1}$$

$$V_{eff,R} = V_G - V_{Dirac} - V_0 \tag{6.2}$$

where V_{Dirac} is the gate voltage at the Dirac point. Considering the parallel plate capacitor model (see Equation 2.11), the induced carrier concentration is defined as $n_{ind,i} = \alpha V_{eff,i}$ (i= L or R), where $\alpha = \varepsilon_0 \varepsilon_r / te$. This shows that the carrier concentration is symmetric in the left and right channels only at the Dirac point, whereas applied gate bias ($V_G - V_D \neq 0$) results in asymmetric

carrier concentration, and, consequently, asymmetric conductivity between the left and right channel. For simplicity, it is assumed in the model that i) conductivity minimum (σ_{min}) and mobility (μ) are invariable to the drain-source bias, ii) the carrier transport between the left and right channel is symmetric, and iii) the metal contacts are identical. From Equation (4.4), the model depicted in Figure 36(f) can be expressed as

$$V_C = V_0 \left(R_{tot,L} - R_{tot,R}\right)/\left(R_{tot,L} + R_{tot,R}\right) \tag{6.3}$$

The calculated rectification characteristics obtained from Equation (6.3) are very similar to experimental results as can be observed in Figure 36(g). The small deviation is expected to arise from the shift of the Dirac point due to increased input bias (the effect of drain-source bias on the channel conductivity is shown in Figure 37).

In a graphene channel in which the intrinsic carrier concentration is negligible ($n_0 \ll n_{ind}$) the channel resistance is primarily determined by the field-effect ($R_{channel} \propto n_{ind} \propto V_{eff}$). In such case, the output voltage has a parabolic dependence on the input voltage ($V_C \propto V_0^2$) and, consequently, the switching parameter shows linear dependence as noted above ($r \propto V_o$) in Figure 36. In a device where the intrinsic carrier concentration is significant, the graphene channel has a diminished field-effect resulting in hindered rectification performance. For significantly high n_o ($n_o >> n_{ind}$), the output voltage would show linear dependence on the input voltage ($V_C \propto V_o$).

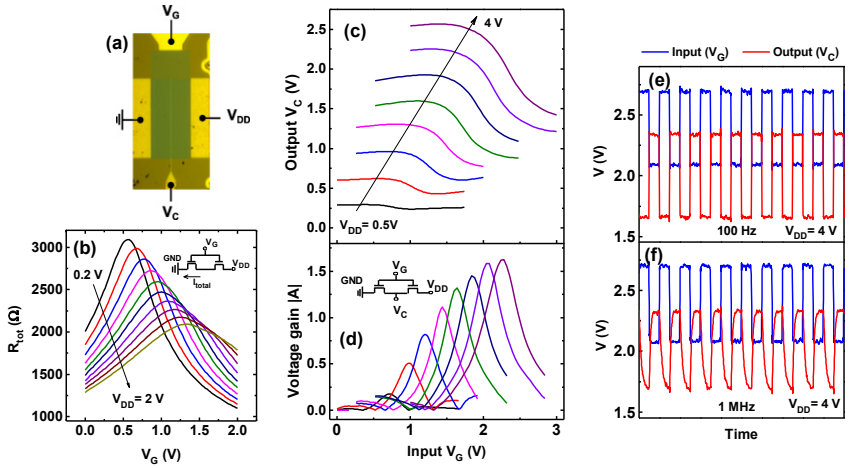

Figure 37. Inverter operations of the 28-μm-channel device (for Figure 36 in the main text). (a) Optical image of the device indicating electrical configuration. (b) Total resistance versus the gate voltage with different V_{DD}. (c) DC transfer voltage characteristics from V_{DD}= 0.5 to 4 V and (d) corresponding output gains. (e-f) Outputs at V_{DD}= 4 V for the

digital waveforms of the input signals at 100 Hz and 1 MHz. Insets in (b) and (d) depict the electrical diagram.

To further demonstrate the viability of the field-effect device, the structure was configured as one terminal is connected to the power source (V_{DD}) and the other to the ground (GND) as shown in Figure 37(a). In the measurements V_G is the input and V_C is the output. R_{tot} as a function of V_G is shown in Figure 37(b). When the V_{DD} increases, the Dirac point is shifted along the V_G and the plotted curve is broaden due to splitting the Dirac point into two (as discussed for the inverter functionality in the section 6.1) [Publication 2]. The maximum voltage gain |A| (= $|dV_C/dV_G|$) was 1.63 at V_{DD}= 4 V. The gain |A| is proportional to the V_{DD} but starts to saturate when V_{DD} reaches around 4 V as seen in Figure 37(c) and (d). Figure 37 (e-f) shows the digital waveforms operating at 100 Hz and 1 MHz, respectively, measured at the highest gain point for V_{DD}= 4 V. The input and output signals are not perfectly matched due to the intrinsic shift of the Dirac point (V_{Dirac} ~ 0.4 V).

To investigate the three-terminal junction behavior, the invasive metal center probe was replaced to a patterned graphene as depicted in Figure 38. The structure is conceptually similar to the TBJ devices [37]–[40] but its scale is tens of micrometers instead of nanometers. The dimensions of the channel are the same as in the device in Figure 36 (28 µm in length and 54 µm in width). The graphene center branch is 2 µm wide and 3 µm long. Raman map of the 2D-band shown in Figure 38(c) clearly identifies that all of the functional areas in the TBJ device are composed of uniform single-layer graphene.

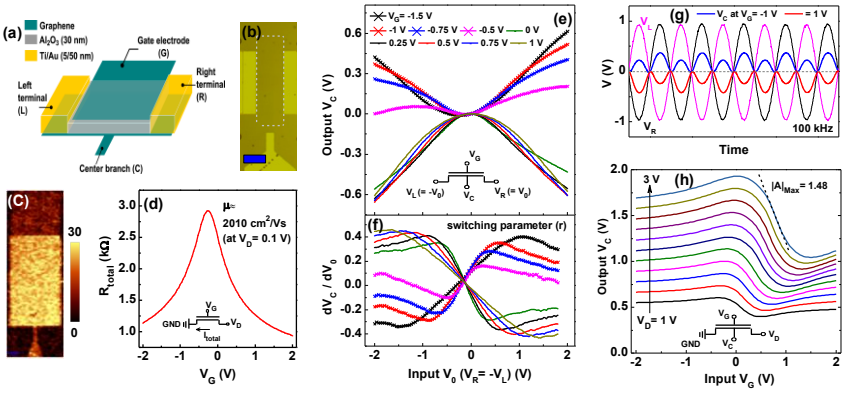

Figure 38. Characteristics of the all-graphene three-terminal TBJ with a channel width of 54 µm. (a) Schematic and (b) optical image of the TBJ. The scale bar is 20 µm. (c) Raman map of the 2D-band of the area indicated by the white-dashed box in (b). (d) Total resistance as a function of the gate voltage. (e-g) Rectifier operation: (e) output voltages detected at the center branch for push-pull input application under the different gate fields (V_0= V_R= -V_L). (f) Switching parameter *r* (=dV_C/dV_0) corresponding to the rectification curves in (e). (g) AC characteristics of the TBJ device for the 100 kHz push-pull inputs (V_0= V_L= -V_R) under two different DC gate fields. The sinusoids

in blue and red are the outputs (V_C) in hole (V_G= -1 V) and electron region (V_G= 1 V), respectively. (h) Inverter operation: DC transfer characteristics with different supply voltages (from V_D= 1 to 3 V). The diagrams in the panels depict the electrical configuration for each of the measurements.

In the device analysis, the Dirac point was observed at V_G ~-0.25 V (slightly n-doped) and the extracted mobility (μ) was ~2010 cm²/Vs as can be seen in Figure 38(d). In rectifier operation, the device has the same characteristics as the device with invasive metal center branch: positive rectification in the hole and negative rectification in the electron transport region. The highly symmetric rectification curves are also observed near the Dirac point (but not in the carrier puddle region which is here considered roughly in -0.5 V< V_G< 0 V) (Figure 38(e)) and the parameter r is saturated to about ±0.45 (Figure 38(f)). The results are in a good agreement with a theoretical study explaining behavior in graphene TBJs [41]. Figure 38(g) further shows full wave rectifications at the center branch without critical time delay for 100 kHz of AC input. The sign of the rectification wave is simply switched by changing the carrier type through the electrostatic control as expected. The sinusoids in blue and red in Figure 38(g) denote the outputs (V_C) in the region of -1 V< V_o< 1 V at V_G= -1 V (hole) and 1 V (electron), respectively.

Operating the same device as an inverter, the maximum voltage gain ($|A|_{Max}$) at V_D= 3V was about 1.5 as shown in Figure 38(h). It is also similar to the device with invasive metal center probe in Figure 36. Considering the device performances as a rectifier and inverter, the results point out that the graphene center branch performs adequately as a signal probe like a metal despite its much larger resistance compared to metal. This emphasizes that graphene T-branch channel is a viable device concept enabling novel circuit architectures. Most of all, it allows the minimization of interfaces in circuitry while pursuing all-graphene IC.

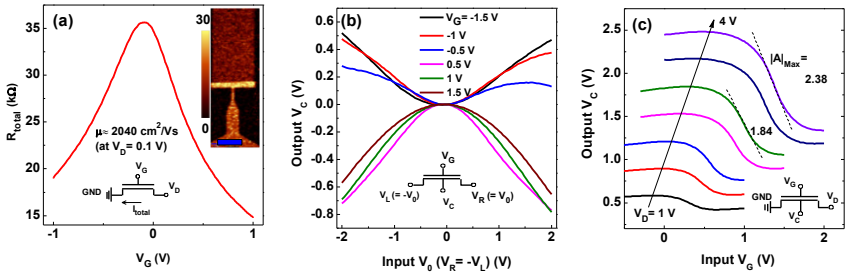

Figure 39. Characteristics of a device with 4 μm channel. (a) Total resistance as a function of the gate voltage (inset: Raman map of 2D-band for the area between L-R). The scale in the map is 20 μm. (b) Rectifier: output V_C for the push-pull voltage V_0 with the different gate voltages. (c) Inverter: output V_C for the gate voltage V_G. All diagrams in the panels depict the electrical configuration for each of the measurements.

It is intriguing that prominent rectifications is observed at room temperature in the CVD graphene-based TBJs having the scale of tens of micrometers. So far rectification has been considered to be enhanced in nanometer scale TBJs due to possible high mobility and the fringing field effect [41]. To study the scaling of the channel width, a set of devices with varying the width from 4 to 54 μm was prepared. Figure 39 shows the characteristics of the device having a width of 4 μm. The Dirac point is observed at about V_G= 0 V and the extracted mobility is ~2040 cm²/Vs. For push-pull application the device performance is slightly enhanced: $|r|_{Max}$ is ~ 0.5 at V_G= 1 V in the region of -1 V<V_o< 1 V. For the inverter operation $|A|_{Max}$ of 1.84 and 2.38 is noted at V_D = 3 V and 4 V, respectively. Although the best overall performance, *i.e.* the highest values of $|r|$ and $|A|$ were observed at W/L= 4/28 μm, no significant trend affecting the device performance is found. The effect of the channel width scaling to the TBJ performance is shown in Figure 40. Furthermore, in this experiment, the mobilities were mostly found in the range of 2000-3000 cm²/Vs with no observed correlation with the microscale channel width. Therefore, in the diffusive transport regime, the performance of the device is maximized when the channel is long enough to avoid the performance degradation due to the high source-drain bias.

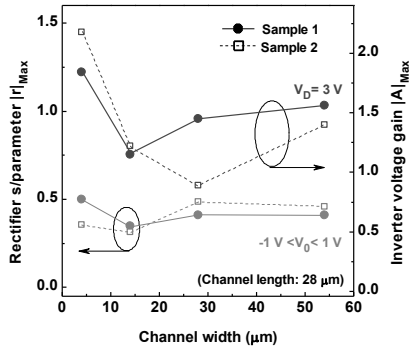

Figure 40. Device characteristics versus channel width (4, 14, 28, and 54 μm). Absolute values of the switching parameter maximum for rectifiers in the range of -1 V< V_0 <1 V and voltage gain maximum for inverter at V_D= 3 V. Channel length is 28 μm for all devices.

The results are remarkable compared to previous reports on nanoscale graphene TTJs or TBJs [37]–[40] when considering that here the much larger channel device is fabricated using photo-thermal CVD graphene having a small grain size (only few micrometers). Table 4 compares the TBJ rectifying performance with the previously reported graphene devices.

Table 4. Comparison of the rectification characteristics of graphene TTJ/TBJ devices reported in previous studies (N/A: not applicable, EG: exfoliated graphene from natural graphite, EPG: epitaxial graphene on SiC, and CVD: chemical vapour deposition of graphene on Cu).

Ref.	Graphene material	Scale *W*/*L* (μm)	V_0	V_G	Rectification		Temp.
					$\|r\|_{Max}$	V_C/V_0 (Max.)	
[36]	EG	~0.2/0.2	0.1 V	±7 V	-	~2%	77 K
[37]	EG	0.2/1.0	0.1 V	-6 ~ 7 V	~0.2	~15%	RT
[38]	EG	0.3/0.45	0.05 V	-3 ~ 2 V	~0.14	~13%	RT
[39]	EPG	0.03/0.5	2 V	N/A	0.4	23%	RT
[40]	EPG	0.02/0.4	1.5 V	N/A	0.4	23%	RT
Here	CVD	4/28	2 V	-1.5 ~ 1.5 V	0.5	38%	RT

From the findings on the single microscale TBJ (as demonstrated in Figure 39), a cascading structure utilizing two TBJs was further fabricated as illustrated in Figure 41. Two TBJs are separated by 30-nm-thick ALD Al_2O_3. The graphene output electrode of the first TBJ (on the top layer) is vertically aligned to function as the gate for the channel of the second TBJ (on the bottom). Both devices are patterned from a continuous CVD graphene film so that the center branch of the top-TBJ extends to the gate electrode for the bottom TBJ. The optical and Raman mapping image for the cascaded structure are shown in Figure 41(a) and (b). Raman map confirms that the center output (graphene) of the top-TBJ is overlapped only in the channel of the bottom TBJ. When measuring the device, the common push-pull input (V_o) was simultaneously applied to the cascaded device structure as depicted in Figure 41(c). Figure 41(d) shows the independently monitored output from the top-TBJ (V_{OUT1}) and the bottom-TBJ (V_{OUT2}). Relatively weak and asymmetric positive rectification was detected from the first TBJ device, indicating that the channel of the device is p-type. In contrast, very distinct and highly symmetric negative rectification (nearly a V shaped) was observed from the second TBJ device. For V_{OUT2}, switching parameter r saturates to about 0.4 at V_o > 0.5 V and efficiency reaches ~ 18% (V_C/V_o ~36%). It is obvious that the bottom-TBJ is stimulated through the gate voltage generated by the top-TBJ and, consequently, shows clear and stable rectification performance. The cascading device structure presents the possibility to design novel graphene devices based on self-gating effect, *i.e.* without employing the external gate bias. This could be applied, for example, as two terminal full-wave rectifier as an alternative to conventional semiconductor diodes such as Schottky diodes [145] which have very high efficiency in rectification but generate only half-wave rectification with a single device.

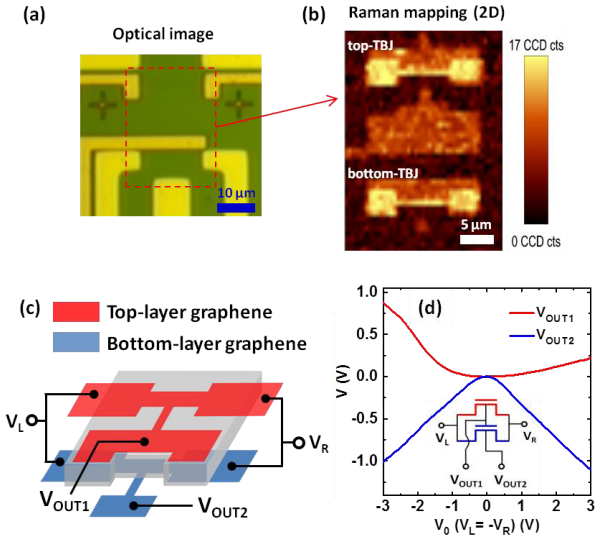

Figure 41. Cascaded two TBJ device structure and characteristics. (a) Optical image and (b) Raman 2D mapping image. The length and width of the confined TBJ channel are 8.4 and 1.2 μm and for the center branch 0.6 and 2.4 μm, respectively. (a) Illustration of the thin-film circuit in which all-graphene devices are in two separate layers. The output graphene electrode of the first TBJ on the top layer is vertically aligned on the top of the channel of the TBJ on the bottom layer. (c) Schematic of the cascaded TBJs with electrical configuration. (d) Output voltages of top-TBJ (V_{OUT1}) and bottom-TBJ (V_{OUT2}) for the common push-pull input voltage V_0. The inset shows the diagram of electrical configuration.

7. Summary and outlook

7.1 Summary

Graphene is a promising material for future electronics. Tremendous research efforts on graphene since its first discovery in 2004 have revealed its extraordinary physical properties. It is surprising that extremely high carrier mobility is viable at room temperature in a 2D plane. Moreover, single-layer graphene is mechanically the strongest material ever found and, accordingly, can be utilized for various applications in micro-electromechanical systems.

In this thesis, photo-thermal CVD method was developed by investigating the process parameters. Specifically, the effect of the growth temperature on the graphene layer quality was intensively examined. From Raman and SEM analysis uniform single-layer graphene was identified to be synthesized in temperature of 935-950 °C. The TLM analysis confirmed that electrical properties were strongly dependent on growth temperature, which is parallel in the Raman pre-examinations. The lowest sheet resistance (260 Ω/sq) was observed in the sample grown at temperature of 950 °C. From the investigations PTCVD was demonstrated to have an ability to produce the crystallized uniform layer rapidly.

Utilizing high quality single-layer graphene synthesized by PTCVD, a local gate controlled complementary graphene device was fabricated and its highly tunable and switchable functions between inverter and voltage controlled resistor were demonstrated. For this performance, two GFETs fabricated on separate backgate electrodes were regulated individually by modulating each of the back-gate voltages, which results in the shift of electrostatic doping of the FET. As an inverter, the transferred output voltage was increased as the charge neutrality points were further split by applying individual back-gate biases. It is beneficial for the device to operate with low V_{DD}, since complementary configuration can be effectively achieved by an external electrostatic doping. As a result, at V_{DD}=

0.3 V, the ΔV_{OUT} increased from -5 to 80 mV by applying the V_{BG1}= -2.5 V (V_{BG2}= 0 v) although the gain |A| is as low as 0.04.

Graphene field-effect devices were further characterized to examine nonlinear behaviors. The nonlinear characteristics exhibiting as an electrical rectification was demonstrated utilizing three-terminal graphene junctions. The rectification was realized at the center of the channel when two terminals were configured in a push-pull application. Utilizing GFET-based TBJ having tens of micrometer scale, prominent room temperature devices performing as a rectifier as well as an inverter were eventually demonstrated. To achieve the all-graphene device structure, the both channel and gate were fabricated using the same single-layer CVD graphene. Associated with the gate field, highly tunable and switchable full-wave rectifications for 100 kHz AC input was achieved. When considering the previous nanoscale TBJs as an rectifier (V_{OUT}/V_{IN}= 5~11%), the results obtained from the microscale thin-film devices shown here (~ 18%) are remarkable because the microscale TBJs operates in diffusive transport regime at room temperature. This finding may open new possibilities for practical applications as the nanoscale for ballistic transport is not necessarily required to achieve rectifier characteristics. The same structure, on the other hand, can be utilized as a logic inverter by changing the electrical configuration. The highest output performance was observed at the longest and narrowest channel (W/L= 4/28 μm), which displayed the switching parameter as $|r|_{Max}$ ~ 0.5 and inverter voltage gain as $|A|_{Max}$ ~ 2.4 at V_D= 4 V. Finally, a cascaded device structure using two identical microscale TBJs where the output of the first TBJ is utilized as a gate input for the second TBJ was introduced. The measured output of the cascaded structure showed very prominent rectification without any external gate. This is a significant step to realize the possibility of layer-by-layer device architecture for graphene based monolithic ICs, overcoming zero-bandgap limit. Altogether, the all-graphene thin-film structure will be useful for transparent and flexible electronic applications.

7.2 Outlook in graphene technology

Without a doubt, graphene will open new possibilities for future device technology. Recent breakthroughs achieved on wafer-scale synthesis of single-crystalline graphene by CVD is expected to lead to real device applications in near future. Although the zero bandgap is still remained as the most critical obstacle for logic device applications, graphene is continuously considered as an innovative material for future technology. A graphene based transparent

electrode is attractive for optoelectronics, which is the most feasible feature because transparent-conductive property can be utilized by avoiding from the critical bandgap limit. A large scale ultra thin alumina-graphene membrane can be effectively applied for the functional devices as a sensor or microphone because its function does not critically depend on the bandgap as well as crystal defects of graphene. Multilayer graphene has another possibility for mechanically functioning applications, for example, a wearable device exploiting elastic-strong feature of graphene. Extremely sensitive behavior in doping from external chemicals or molecules (or biomolecues) allows graphene to be utilized as an efficient chemical (bio) sensor.

References

[1] K. S. Novoselov, A. K. Geim, S. V Morozov, D. Jiang, Y. Zhang, S. V Dubonos, I. V Grigorieva, and A. A. Firsov, "Electric field effect in atomically thin carbon films.," *Science*, vol. 306, no. 5696, pp. 666–669, 2004.

[2] A. K. Geim and K. S. Novoselov, "The rise of graphene.," *Nat. Mater.*, vol. 6, no. 3, pp. 183–91, Mar. 2007.

[3] J. C. Meyer, A. K. Geim, M. I. Katsnelson, K. S. Novoselov, T. J. Booth, and S. Roth, "The structure of suspended graphene sheets.," *Nature*, vol. 446, no. 7131, pp. 60–3, Mar. 2007.

[4] C. Lee, X. Wei, J. W. Kysar, and J. Hone, "Measurement of the elastic properties and intrinsic strength of monolayer graphene.," *Science*, vol. 321, no. 5887, pp. 385–8, Jul. 2008.

[5] M. Peplow, "Graphene: The quest for supercarbon.," *Nature*, vol. 503, no. 7476, pp. 327–9, Nov. 2013.

[6] J. Baimova and E. Korznikova, "Review on crumpled graphene: unique mechanical properties," *Rev. Adv. Mater. Sci.*, vol. 39, pp. 69–83, 2014.

[7] F. Schwierz, "Graphene transistors.," *Nat. Nanotechnol.*, vol. 5, no. 7, pp. 487–96, Jul. 2010.

[8] L. Liao, Y.-C. Lin, M. Bao, R. Cheng, J. Bai, Y. Liu, Y. Qu, K. L. Wang, Y. Huang, and X. Duan, "High-speed graphene transistors with a self-aligned nanowire gate.," *Nature*, vol. 467, no. 7313, pp. 305–8, Sep. 2010.

[9] N. Petrone, I. Meric, J. Hone, and K. L. Shepard, "Graphene field-effect transistors with gigahertz-frequency power gain on flexible substrates.," *Nano Lett.*, vol. 13, no. 1, pp. 121–5, Jan. 2013.

[10] J. Lee, T.-J. Ha, H. Li, K. N. Parrish, M. Holt, A. Dodabalapur, R. S. Ruoff, and D. Akinwande, "25 GHz embedded-gate graphene transistors with high-k dielectrics on extremely flexible plastic sheets.," *ACS Nano*, vol. 7, no. 9, pp. 7744–50, Sep. 2013.

[11] J. W. Suk, W. H. Lee, J. Lee, H. Chou, R. D. Piner, Y. Hao, D. Akinwande, and R. S. Ruoff, "Enhancement of the electrical properties of graphene grown by chemical vapor deposition via controlling the effects of polymer residue.," *Nano Lett.*, vol. 13, no. 4, pp. 1462–7, Apr. 2013.

[12] J. R. Williams, L. Dicarlo, and C. M. Marcus, "Quantum Hall effect in a gate-controlled p-n junction of graphene.," *Science*, vol. 317, no. 5838, pp. 638–41, Aug. 2007.

[13] F. Xia, D. B. Farmer, Y.-M. Lin, and P. Avouris, "Graphene field-effect transistors with high on/off current ratio and large transport band gap at room temperature.," *Nano Lett.*, vol. 10, no. 2, pp. 715–8, Feb. 2010.

[14] R. Sordan, F. Traversi, and V. Russo, "Logic gates with a single graphene transistor," *Appl. Phys. Lett.*, vol. 94, no. 7, p. 073305, Feb. 2009.

[15] F. Traversi, V. Russo, and R. Sordan, "Integrated complementary graphene inverter," *Appl. Phys. Lett.*, vol. 94, no. 22, p. 223312, Jun. 2009.

[16] S.-L. Li, H. Miyazaki, A. Kumatani, A. Kanda, and K. Tsukagoshi, "Low operating bias and matched input-output characteristics in graphene logic inverters.," *Nano Lett.*, vol. 10, no. 7, pp. 2357–62, Jul. 2010.

[17] S.-L. Li, H. Miyazaki, H. Hiura, C. Liu, and K. Tsukagoshi, "Enhanced logic performance with semiconducting bilayer graphene channels.," *ACS Nano*, vol. 5, no. 1, pp. 500–6, Jan. 2011.

[18] S.-L. Li, H. Miyazaki, M. V Lee, C. Liu, A. Kanda, and K. Tsukagoshi, "Complementary-like graphene logic gates controlled by electrostatic doping.," *Small*, vol. 7, no. 11, pp. 1552–6, Jun. 2011.

[19] A. El Moutaouakil, H.-C. Kang, H. Handa, H. Fukidome, T. Suemitsu, E. Sano, M. Suemitsu, and T. Otsuji, "Room Temperature Logic Inverter on Epitaxial Graphene-on-Silicon Device," *Jpn. J. Appl. Phys.*, vol. 50, no. 7, p. 070113, Jul. 2011.

[20] E. Kim, N. Jain, Y. Xu, and B. Yu, "Logic Inverter Implemented with CVD-Assembled Graphene FET on Hexagonal Boron Nitride," *IEEE Trans. Nanotechnol.*, vol. 11, no. 3, pp. 619–623, May 2012.

[21] L. G. Rizzi, M. Bianchi, A. Behnam, E. Carrion, E. Guerriero, L. Polloni, E. Pop, and R. Sordan, "Cascading wafer-scale integrated graphene complementary inverters under ambient conditions.," *Nano Lett.*, vol. 12, no. 8, pp. 3948–53, Aug. 2012.

[22] E. Guerriero, L. Polloni, M. Bianchi, A. Behnam, E. Carrion, L. G. Rizzi, E. Pop, and R. Sordan, "Gigahertz integrated graphene ring oscillators.," *ACS Nano*, vol. 7, no. 6, pp. 5588–94, Jun. 2013.

[23] D. Schall, M. Otto, D. Neumaier, and H. Kurz, "Integrated Ring Oscillators based on high-performance Graphene Inverters.," *Sci. Rep.*, vol. 3, p. 2592, Jan. 2013.

[24] C. Beenakker and H. van Houten, “Billiard model of a ballistic multiprobe conductor,” *Phys. Rev. Lett.*, vol. 63, no. 17, pp. 1857–1860, Oct. 1989.

[25] H. Xu, “Theory of nonlinear ballistic transport in quasi-one-dimensional constrictions,” *Phys. Rev. B*, vol. 47, no. 23, pp. 15630–15637, Jun. 1993.

[26] A. Song, A. Lorke, A. Kriele, J. Kotthaus, W. Wegscheider, and M. Bichler, “Nonlinear Electron Transport in an Asymmetric Microjunction: A Ballistic Rectifier,” *Phys. Rev. Lett.*, vol. 80, no. 17, pp. 3831–3834, Apr. 1998.

[27] R. Fleischmann and T. Geisel, “Mesoscopic Rectifiers Based on Ballistic Transport,” *Phys. Rev. Lett.*, vol. 89, no. 1, p. 016804, Jun. 2002.

[28] S. de Haan, A. Lorke, J. . Kotthaus, M. Bichler, and W. Wegscheider, “Quantized transport in ballistic rectifiers: sign reversal and step-like output,” *Phys. E Low-dimensional Syst. Nanostructures*, vol. 21, no. 2–4, pp. 916–920, Mar. 2004.

[29] K. Hieke and M. Ulfward, “Nonlinear operation of the Y-branch switch: Ballistic switching mode at room temperature,” *Phys. Rev. B*, vol. 62, no. 24, pp. 16727–16730, Dec. 2000.

[30] I. Shorubalko, H. Q. Xu, I. Maximov, P. Omling, L. Samuelson, and W. Seifert, “Nonlinear operation of GaInAs/InP-based three-terminal ballistic junctions,” *Appl. Phys. Lett.*, vol. 79, no. 9, p. 1384, Aug. 2001.

[31] D. Wallin, I. Shorubalko, H. Q. Xu, and A. Cappy, “Nonlinear electrical properties of three-terminal junctions,” *Appl. Phys. Lett.*, vol. 89, no. 9, p. 092124, Sep. 2006.

[32] S. Bollaert, A. Cappy, Y. Roelens, J. S. Galloo, C. Gardes, Z. Teukam, X. Wallart, J. Mateos, T. Gonzalez, B. G. Vasallo, B. Hackens, L. Berdnarz, and I. Huynen, “Ballistic nano-devices for high frequency applications,” *Thin Solid Films*, vol. 515, no. 10, pp. 4321–4326, Mar. 2007.

[33] H. Q. Xu, “Electrical properties of three-terminal ballistic junctions,” *Appl. Phys. Lett.*, vol. 78, no. 14, p. 2064, Apr. 2001.

[34] A. Jordan and M. Büttiker, “Gap theory of rectification in ballistic three-terminal conductors,” *Phys. Rev. B*, vol. 77, no. 7, p. 075334, Feb. 2008.

[35] J. Mateos, B. G. Vasallo, D. Pardo, T. Gonzalez, J. Galloo, S. Bollaert, Y. Roelens, and A. Cappy, “Microscopic modeling of nonlinear transport in ballistic nanodevices,” *IEEE Trans. Electron Devices*, vol. 50, no. 9, pp. 1897–1905, Sep. 2003.

[36] A. Jacobsen, I. Shorubalko, L. Maag, U. Sennhauser, and K. Ensslin, “Rectification in three-terminal graphene junctions,” *Appl. Phys. Lett.*, vol. 97, no. 3, p. 032110, Jul. 2010.

[37] S. Fadzli Abd Rahman, S. Kasai, and A. Manaf Hashim, “Room temperature nonlinear operation of a graphene-based three-branch

nanojunction device with chemical doping," *Appl. Phys. Lett.*, vol. 100, no. 19, p. 193116, May 2012.

[38] X. Yin and S. Kasai, "Graphene-based three-branch nano-junction (TBJ) logic inverter," *Phys. status solidi*, vol. 10, no. 11, pp. 1485–1488, Nov. 2013.

[39] R. Göckeritz, J. Pezoldt, and F. Schwierz, "Epitaxial graphene three-terminal junctions," *Appl. Phys. Lett.*, vol. 99, no. 17, p. 173111, Oct. 2011.

[40] B. Händel, B. Hähnlein, R. Göckeritz, F. Schwierz, and J. Pezoldt, "Electrical gating and rectification in graphene three-terminal junctions," *Appl. Surf. Sci.*, vol. 291, pp. 87–92, Feb. 2014.

[41] P. Butti, I. Shorubalko, U. Sennhauser, and K. Ensslin, "Finite element simulations of graphene based three-terminal nanojunction rectifiers," *J. Appl. Phys.*, vol. 114, no. 3, p. 033710, Jul. 2013.

[42] X. Li, W. Cai, J. An, S. Kim, J. Nah, D. Yang, R. Piner, A. Velamakanni, I. Jung, E. Tutuc, S. K. Banerjee, L. Colombo, and R. S. Ruoff, "Large-area synthesis of high-quality and uniform graphene films on copper foils.," *Science*, vol. 324, no. 5932, pp. 1312–4, Jun. 2009.

[43] S. Bae, H. Kim, Y. Lee, X. Xu, J.-S. Park, Y. Zheng, J. Balakrishnan, T. Lei, H. R. Kim, Y. Il Song, Y.-J. Kim, K. S. Kim, B. Ozyilmaz, J.-H. Ahn, B. H. Hong, and S. Iijima, "Roll-to-roll production of 30-inch graphene films for transparent electrodes.," *Nat. Nanotechnol.*, vol. 5, no. 8, pp. 574–8, Aug. 2010.

[44] L. Gao, G.-X. Ni, Y. Liu, B. Liu, A. H. Castro Neto, and K. P. Loh, "Face-to-face transfer of wafer-scale graphene films.," *Nature*, vol. 505, no. 7482, pp. 190–4, Jan. 2014.

[45] P. Wallace, "The Band Theory of Graphite," *Phys. Rev.*, vol. 71, no. 9, pp. 622–634, May 1947.

[46] J. McClure, "Band Structure of Graphite and de Haas-van Alphen Effect," *Phys. Rev.*, vol. 108, no. 3, pp. 612–618, Nov. 1957.

[47] J. W. McClure, "Theory of Diamagnetism of Graphite," *Phys. Rev.*, vol. 119, no. 2, pp. 606–613, Jul. 1960.

[48] H. W. Kroto, J. R. Heath, S. C. O'Brien, R. F. Curl, and R. E. Smalley, "C60: Buckminsterfullerene," *Nature*, vol. 318, no. 6042, pp. 162–163, Nov. 1985.

[49] S. Iijima, "Helical microtubules of graphitic carbon," *Nature*, vol. 354, no. 6348, pp. 56–58, Nov. 1991.

[50] F. Léonard, *The Physics of Carbon Nanotube Devices*. Elsevier, 2009.

[51] M. Terrones, A. R. Botello-Méndez, J. Campos-Delgado, F. López-Urías, Y. I. Vega-Cantú, F. J. Rodríguez-Macías, A. L. Elías, E. Muñoz-

Sandoval, A. G. Cano-Márquez, and J.-C. Charlier, “Graphene and graphite nanoribbons: Morphology, properties, synthesis, defects and applications,” *Nano Today*, vol. 5, no. 4, pp. 351–372, Aug. 2010.

[52] X. Chen, F. Tian, C. Persson, W. Duan, and N. Chen, “Interlayer interactions in graphites.,” *Sci. Rep.*, vol. 3, p. 3046, Jan. 2013.

[53] J.-T. Wang, C. Chen, and Y. Kawazoe, “New carbon allotropes with helical chains of complementary chirality connected by ethene-type π-conjugation.,” *Sci. Rep.*, vol. 3, p. 3077, Jan. 2013.

[54] F. Jean-Noel and G. Mark Oliver, “Introduction to the Physical Properties of Graphene,” 2008.

[55] J. Chen, “Diffusive Charge Transport in Graphene.” 2009.

[56] S. Reich, J. Maultzsch, C. Thomsen, and P. Ordejón, “Tight-binding description of graphene,” *Phys. Rev. B*, vol. 66, no. 3, p. 035412, Jul. 2002.

[57] “Wiley: Carbon Nanotubes: Basic Concepts and Physical Properties - Stephanie Reich, Christian Thomsen, Janina Maultzsch.” [Online]. Available: http://eu.wiley.com/WileyCDA/WileyTitle/productCd-3527403868.html. [Accessed: 10-Feb-2015].

[58] R. Saito, G. Dresselhaus, and M. Dresselhaus, “Trigonal warping effect of carbon nanotubes,” *Phys. Rev. B*, vol. 61, no. 4, pp. 2981–2990, Jan. 2000.

[59] A. H. Castro Neto, N. M. R. Peres, K. S. Novoselov, and A. K. Geim, “The electronic properties of graphene,” *Rev. Mod. Phys.*, vol. 81, no. 1, pp. 109–162, Jan. 2009.

[60] S. Das Sarma, S. Adam, E. H. Hwang, and E. Rossi, “Electronic transport in two-dimensional graphene,” *Rev. Mod. Phys.*, vol. 83, no. 2, pp. 407–470, May 2011.

[61] A. Bostwick, T. Ohta, T. Seyller, K. Horn, and E. Rotenberg, “Quasiparticle dynamics in graphene,” *Nat. Phys.*, vol. 3, no. 1, pp. 36–40, Dec. 2006.

[62] M. I. Katsnelson, K. S. Novoselov, and A. K. Geim, “Chiral tunnelling and the Klein paradox in graphene,” *Nat. Phys.*, vol. 2, no. 9, pp. 620–625, Aug. 2006.

[63] K. Banerjee, “Nonlinear behavior of three terminal graphene junctions,” Master’s Thesis, Aalto University, 2011.

[64] Y. Wu, Y. Lin, A. A. Bol, K. A. Jenkins, F. Xia, D. B. Farmer, Y. Zhu, and P. Avouris, “High-frequency, scaled graphene transistors on diamond-like carbon.,” *Nature*, vol. 472, no. 7341, pp. 74–8, Apr. 2011.

[65] Y.-M. Lin, C. Dimitrakopoulos, K. A. Jenkins, D. B. Farmer, H.-Y. Chiu, A. Grill, and P. Avouris, “100-GHz transistors from wafer-scale epitaxial graphene.,” *Science*, vol. 327, no. 5966, p. 662, Feb. 2010.

[66] C.-C. Chen, M. Aykol, C.-C. Chang, A. F. J. Levi, and S. B. Cronin, “Graphene-silicon Schottky diodes.,” *Nano Lett.*, vol. 11, no. 5, pp. 1863–7, May 2011.

[67] H. Yang, J. Heo, S. Park, H. J. Song, D. H. Seo, K.-E. Byun, P. Kim, I. Yoo, H.-J. Chung, and K. Kim, “Graphene barristor, a triode device with a gate-controlled Schottky barrier.,” *Science*, vol. 336, no. 6085, pp. 1140–3, Jun. 2012.

[68] D. Sinha and J. U. Lee, “Ideal graphene/silicon Schottky junction diodes.,” *Nano Lett.*, vol. 14, no. 8, pp. 4660–4, Aug. 2014.

[69] T. Roy, M. Tosun, J. S. Kang, A. B. Sachid, S. B. Desai, M. Hettick, C. C. Hu, and A. Javey, “Field-effect transistors built from all two-dimensional material components.,” *ACS Nano*, vol. 8, no. 6, pp. 6259–64, Jun. 2014.

[70] H. Tian, Z. Tan, C. Wu, X. Wang, M. A. Mohammad, D. Xie, Y. Yang, J. Wang, L.-J. Li, J. Xu, and T.-L. Ren, “Novel field-effect Schottky barrier transistors based on graphene-MoS2 heterojunctions.,” *Sci. Rep.*, vol. 4, p. 5951, Jan. 2014.

[71] T. Georgiou, R. Jalil, B. D. Belle, L. Britnell, R. V Gorbachev, S. V Morozov, Y.-J. Kim, A. Gholinia, S. J. Haigh, O. Makarovsky, L. Eaves, L. A. Ponomarenko, A. K. Geim, K. S. Novoselov, and A. Mishchenko, “Vertical field-effect transistor based on graphene-WS2 heterostructures for flexible and transparent electronics.,” *Nat. Nanotechnol.*, vol. 8, no. 2, pp. 100–3, Feb. 2013.

[72] V. P. Pham, K. N. Kim, M. H. Jeon, K. S. Kim, and G. Y. Yeom, “Cyclic chlorine trap-doping for transparent, conductive, thermally stable and damage-free graphene.,” *Nanoscale*, vol. 6, no. 24, pp. 15301–8, Dec. 2014.

[73] Y. Kim, J. Park, J. Kang, J. M. Yoo, K. Choi, E. S. Kim, J.-B. Choi, C. Hwang, K. S. Novoselov, and B. H. Hong, “A highly conducting graphene film with dual-side molecular n-doping.,” *Nanoscale*, vol. 6, no. 16, pp. 9545–9, Aug. 2014.

[74] A. D. Smith, F. Niklaus, A. Paussa, S. Vaziri, A. C. Fischer, M. Sterner, F. Forsberg, A. Delin, D. Esseni, P. Palestri, M. Östling, and M. C. Lemme, “Electromechanical piezoresistive sensing in suspended graphene membranes.,” *Nano Lett.*, vol. 13, no. 7, pp. 3237–42, Jul. 2013.

[75] Q. Zhou and A. Zettl, “Electrostatic graphene loudspeaker,” *Appl. Phys. Lett.*, vol. 102, no. 22, p. 223109, Mar. 2013.

[76] Y. Yang, A. M. Asiri, Z. Tang, D. Du, and Y. Lin, “Graphene based materials for biomedical applications,” *Mater. Today*, vol. 16, no. 10, pp. 365–373, Oct. 2013.

[77] C. Berger, Z. Song, T. Li, X. Li, A. Y. Ogbazghi, R. Feng, Z. Dai, A. N. Marchenkov, E. H. Conrad, P. N. First, and W. A. de Heer, "Ultrathin Epitaxial Graphite: 2D Electron Gas Properties and a Route toward Graphene-based Nanoelectronics," *J. Phys. Chem. B*, vol. 108, no. 52, pp. 19912–19916, Dec. 2004.

[78] C. Berger, Z. Song, X. Li, X. Wu, N. Brown, C. Naud, D. Mayou, T. Li, J. Hass, A. N. Marchenkov, E. H. Conrad, P. N. First, and W. A. de Heer, "Electronic confinement and coherence in patterned epitaxial graphene.," *Science*, vol. 312, no. 5777, pp. 1191–6, May 2006.

[79] W. A. de Heer, C. Berger, X. Wu, P. N. First, E. H. Conrad, X. Li, T. Li, M. Sprinkle, J. Hass, M. L. Sadowski, M. Potemski, and G. Martinez, "Epitaxial graphene," *Solid State Commun.*, vol. 143, no. 1–2, pp. 92–100, Jul. 2007.

[80] Z. Song, *Fabrication and Characterization of Nanopatterned Epitaxial Graphene Films for Carbon Based Electronics*. Georgia Institue of technology (ISBN: 1109871538), 2006.

[81] P. Mélinon, B. Masenelli, F. Tournus, and A. Perez, "Playing with carbon and silicon at the nanoscale.," *Nat. Mater.*, vol. 6, no. 7, pp. 479–90, Jul. 2007.

[82] Y.-M. Lin, C. Dimitrakopoulos, K. A. Jenkins, D. B. Farmer, H.-Y. Chiu, A. Grill, and P. Avouris, "100-GHz transistors from wafer-scale epitaxial graphene.," *Science*, vol. 327, no. 5966, p. 662, Feb. 2010.

[83] J. Baringhaus, M. Ruan, F. Edler, A. Tejeda, M. Sicot, A. Taleb-Ibrahimi, A.-P. Li, Z. Jiang, E. H. Conrad, C. Berger, C. Tegenkamp, and W. A. de Heer, "Exceptional ballistic transport in epitaxial graphene nanoribbons.," *Nature*, vol. 506, no. 7488, pp. 349–54, Feb. 2014.

[84] C.-M. Seah, S.-P. Chai, and A. R. Mohamed, "Mechanisms of graphene growth by chemical vapour deposition on transition metals," *Carbon N. Y.*, vol. 70, pp. 1–21, Apr. 2014.

[85] M. Batzill, "The surface science of graphene: Metal interfaces, CVD synthesis, nanoribbons, chemical modifications, and defects," *Surf. Sci. Rep.*, vol. 67, no. 3–4, pp. 83–115, Mar. 2012.

[86] C. Mattevi, H. Kim, and M. Chhowalla, "A review of chemical vapour deposition of graphene on copper," *J. Mater. Chem.*, vol. 21, no. 10, p. 3324, Feb. 2011.

[87] X. Li, W. Cai, L. Colombo, and R. S. Ruoff, "Evolution of graphene growth on Ni and Cu by carbon isotope labeling.," *Nano Lett.*, vol. 9, no. 12, pp. 4268–72, Dec. 2009.

[88] Q. Yu, J. Lian, S. Siriponglert, H. Li, Y. P. Chen, and S.-S. Pei, "Graphene segregated on Ni surfaces and transferred to insulators," *Appl. Phys. Lett.*, vol. 93, no. 11, p. 113103, Sep. 2008.

[89] A. E. Karu, "Pyrolytic Formation of Highly Crystalline Graphite Films," *J. Appl. Phys.*, vol. 37, no. 5, p. 2179, Jun. 1966.

[90] S. Helveg, C. López-Cartes, J. Sehested, P. L. Hansen, B. S. Clausen, J. R. Rostrup-Nielsen, F. Abild-Pedersen, and J. K. Nørskov, "Atomic-scale imaging of carbon nanofibre growth.," *Nature*, vol. 427, no. 6973, pp. 426–9, Jan. 2004.

[91] A. Reina, X. Jia, J. Ho, D. Nezich, H. Son, V. Bulovic, M. S. Dresselhaus, and J. Kong, "Large area, few-layer graphene films on arbitrary substrates by chemical vapor deposition.," *Nano Lett.*, vol. 9, no. 1, pp. 30–5, Jan. 2009.

[92] K. S. Kim, Y. Zhao, H. Jang, S. Y. Lee, J. M. Kim, K. S. Kim, J.-H. Ahn, P. Kim, J.-Y. Choi, and B. H. Hong, "Large-scale pattern growth of graphene films for stretchable transparent electrodes.," *Nature*, vol. 457, no. 7230, pp. 706–10, Feb. 2009.

[93] Y. Lee, S. Bae, H. Jang, S. Jang, S.-E. Zhu, S. H. Sim, Y. Il Song, B. H. Hong, and J.-H. Ahn, "Wafer-scale synthesis and transfer of graphene films.," *Nano Lett.*, vol. 10, no. 2, pp. 490–3, Feb. 2010.

[94] S. Riikonen, A. V. Krasheninnikov, L. Halonen, and R. M. Nieminen, "The Role of Stable and Mobile Carbon Adspecies in Copper-Promoted Graphene Growth," *J. Phys. Chem. C*, vol. 116, no. 9, pp. 5802–5809, Mar. 2012.

[95] Z. Luo, S. Kim, N. Kawamoto, A. M. Rappe, and A. T. C. Johnson, "Growth mechanism of hexagonal-shape graphene flakes with zigzag edges.," *ACS Nano*, vol. 5, no. 11, pp. 9154–60, Nov. 2011.

[96] P. Y. Huang, C. S. Ruiz-Vargas, A. M. van der Zande, W. S. Whitney, M. P. Levendorf, J. W. Kevek, S. Garg, J. S. Alden, C. J. Hustedt, Y. Zhu, J. Park, P. L. McEuen, and D. A. Muller, "Grains and grain boundaries in single-layer graphene atomic patchwork quilts.," *Nature*, vol. 469, no. 7330, pp. 389–92, Jan. 2011.

[97] Q. Yu, L. A. Jauregui, W. Wu, R. Colby, J. Tian, Z. Su, H. Cao, Z. Liu, D. Pandey, D. Wei, T. F. Chung, P. Peng, N. P. Guisinger, E. A. Stach, J. Bao, S.-S. Pei, and Y. P. Chen, "Control and characterization of individual grains and grain boundaries in graphene grown by chemical vapour deposition.," *Nat. Mater.*, vol. 10, no. 6, pp. 443–9, Jun. 2011.

[98] K. Kim, Z. Lee, W. Regan, C. Kisielowski, M. F. Crommie, and A. Zettl, "Grain boundary mapping in polycrystalline graphene.," *ACS Nano*, vol. 5, no. 3, pp. 2142–6, Mar. 2011.

[99] A. W. Cummings, D. L. Duong, V. L. Nguyen, D. Van Tuan, J. Kotakoski, J. E. Barrios Vargas, Y. H. Lee, and S. Roche, "Charge transport in polycrystalline graphene: challenges and opportunities.," *Adv. Mater.*, vol. 26, no. 30, pp. 5079–94, Aug. 2014.

[100] W. Kim, J. Riikonen, S. Arpiainen, O. Svensk, C. Li, and H. Lipsanen, "Growth of CVD graphene on copper by rapid thermal processing," *MRS Proc.*, vol. 1451, pp. 27–32, Jul. 2012.

[101] M. P. Levendorf, C. S. Ruiz-Vargas, S. Garg, and J. Park, “Transfer-free batch fabrication of single layer graphene transistors.,” *Nano Lett.*, vol. 9, no. 12, pp. 4479–83, Dec. 2009.

[102] J. Kwak, J. H. Chu, J.-K. Choi, S.-D. Park, H. Go, S. Y. Kim, K. Park, S.-D. Kim, Y.-W. Kim, E. Yoon, S. Kodambaka, and S.-Y. Kwon, “Near room-temperature synthesis of transfer-free graphene films.,” *Nat. Commun.*, vol. 3, p. 645, Jan. 2012.

[103] Y. Wang, Y. Zheng, X. Xu, E. Dubuisson, Q. Bao, J. Lu, and K. P. Loh, “Electrochemical delamination of CVD-grown graphene film: toward the recyclable use of copper catalyst.,” *ACS Nano*, vol. 5, no. 12, pp. 9927–33, Dec. 2011.

[104] F. Banhart, J. Kotakoski, and A. V Krasheninnikov, “Structural defects in graphene.,” *ACS Nano*, vol. 5, no. 1, pp. 26–41, Jan. 2011.

[105] Y. Wang, D. C. Alsmeyer, and R. L. McCreery, “Raman spectroscopy of carbon materials: structural basis of observed spectra,” *Chem. Mater.*, vol. 2, no. 5, pp. 557–563, Sep. 1990.

[106] R. R. Nair, P. Blake, A. N. Grigorenko, K. S. Novoselov, T. J. Booth, T. Stauber, N. M. R. Peres, and A. K. Geim, “Fine structure constant defines visual transparency of graphene.,” *Science*, vol. 320, no. 5881, p. 1308, Jun. 2008.

[107] P. Blake, E. W. Hill, A. H. Castro Neto, K. S. Novoselov, D. Jiang, R. Yang, T. J. Booth, and A. K. Geim, “Making graphene visible,” *Appl. Phys. Lett.*, vol. 91, no. 6, p. 063124, Aug. 2007.

[108] L. Gao, W. Ren, F. Li, and H.-M. Cheng, “Total color difference for rapid and accurate identification of graphene.,” *ACS Nano*, vol. 2, no. 8, pp. 1625–33, Aug. 2008.

[109] I. Jung, M. Pelton, R. Piner, D. A. Dikin, S. Stankovich, S. Watcharotone, M. Hausner, and R. S. Ruoff, “Simple Approach for High-Contrast Optical Imaging and Characterization of Graphene-Based Sheets,” *Nano Lett.*, vol. 7, no. 12, pp. 3569–3575, Dec. 2007.

[110] K. Kim, S. Coh, L. Z. Tan, W. Regan, J. M. Yuk, E. Chatterjee, M. F. Crommie, M. L. Cohen, S. G. Louie, and A. Zettl, “Raman Spectroscopy Study of Rotated Double-Layer Graphene: Misorientation-Angle Dependence of Electronic Structure,” *Phys. Rev. Lett.*, vol. 108, no. 24, p. 246103, Jun. 2012.

[111] L. M. Malard, M. A. Pimenta, G. Dresselhaus, and M. S. Dresselhaus, “Raman spectroscopy in graphene,” *Phys. Rep.*, vol. 473, no. 5–6, pp. 51–87, Apr. 2009.

[112] A. C. Ferrari, J. C. Meyer, V. Scardaci, C. Casiraghi, M. Lazzeri, F. Mauri, S. Piscanec, D. Jiang, K. S. Novoselov, S. Roth, and A. K. Geim, “Raman Spectrum of Graphene and Graphene Layers,” *Phys. Rev. Lett.*, vol. 97, no. 18, p. 187401, Oct. 2006.

[113] A. C. Ferrari, “Raman spectroscopy of graphene and graphite: Disorder, electron–phonon coupling, doping and nonadiabatic effects,” *Solid State Commun.*, vol. 143, no. 1–2, pp. 47–57, Jul. 2007.

[114] D. Graf, F. Molitor, K. Ensslin, C. Stampfer, A. Jungen, C. Hierold, and L. Wirtz, “Spatially resolved Raman spectroscopy of single- and few-layer graphene.,” *Nano Lett.*, vol. 7, no. 2, pp. 238–42, Feb. 2007.

[115] C. Cong, T. Yu, R. Saito, G. F. Dresselhaus, and M. S. Dresselhaus, “Second-order overtone and combination Raman modes of graphene layers in the range of 1690-2150 cm(-1).,” *ACS Nano*, vol. 5, no. 3, pp. 1600–5, Mar. 2011.

[116] R. Rao, R. Podila, R. Tsuchikawa, J. Katoch, D. Tishler, A. M. Rao, and M. Ishigami, “Effects of layer stacking on the combination Raman modes in graphene.,” *ACS Nano*, vol. 5, no. 3, pp. 1594–9, Mar. 2011.

[117] K. Sato, J. S. Park, R. Saito, C. Cong, T. Yu, C. H. Lui, T. F. Heinz, G. Dresselhaus, and M. S. Dresselhaus, “Raman spectra of out-of-plane phonons in bilayer graphene,” *Phys. Rev. B*, vol. 84, no. 3, p. 035419, Jul. 2011.

[118] J. Yan, Y. Zhang, P. Kim, and A. Pinczuk, “Electric Field Effect Tuning of Electron-Phonon Coupling in Graphene,” *Phys. Rev. Lett.*, vol. 98, no. 16, p. 166802, Apr. 2007.

[119] S. Pisana, M. Lazzeri, C. Casiraghi, K. S. Novoselov, A. K. Geim, A. C. Ferrari, and F. Mauri, “Breakdown of the adiabatic Born-Oppenheimer approximation in graphene.,” *Nat. Mater.*, vol. 6, no. 3, pp. 198–201, Mar. 2007.

[120] C. Casiraghi, S. Pisana, K. S. Novoselov, A. K. Geim, and A. C. Ferrari, “Raman fingerprint of charged impurities in graphene,” *Appl. Phys. Lett.*, vol. 91, no. 23, p. 233108, Dec. 2007.

[121] D. K. Schroder, *Semiconductor Material and Device Characterization*, 3rd Editio. Wiley.

[122] F. Xia, V. Perebeinos, Y. Lin, Y. Wu, and P. Avouris, “The origins and limits of metal-graphene junction resistance.,” *Nat. Nanotechnol.*, vol. 6, no. 3, pp. 179–84, Mar. 2011.

[123] S. Kim, J. Nah, I. Jo, D. Shahrjerdi, L. Colombo, Z. Yao, E. Tutuc, and S. K. Banerjee, “Realization of a high mobility dual-gated graphene field-effect transistor with Al[sub 2]O[sub 3] dielectric,” *Appl. Phys. Lett.*, vol. 94, no. 6, p. 062107, Feb. 2009.

[124] H. Wang, A. Hsu, J. Wu, J. Kong, and T. Palacios, “Graphene-Based Ambipolar RF Mixers,” *IEEE Electron Device Lett.*, vol. 31, no. 9, pp. 906–908, Sep. 2010.

[125] Y.-M. Lin, A. Valdes-Garcia, S.-J. Han, D. B. Farmer, I. Meric, Y. Sun, Y. Wu, C. Dimitrakopoulos, A. Grill, P. Avouris, and K. A. Jenkins, “Wafer-scale graphene integrated circuit.,” *Science*, vol. 332, no. 6035, pp. 1294–7, Jun. 2011.

[126] S.-J. Han, A. V. Garcia, S. Oida, K. A. Jenkins, and W. Haensch, “Graphene radio frequency receiver integrated circuit.,” *Nat. Commun.*, vol. 5, p. 3086, Jan. 2014.

[127] J. Ryu, Y. Kim, D. Won, N. Kim, J. S. Park, E.-K. Lee, D. Cho, S.-P. Cho, S. J. Kim, G. H. Ryu, H.-A.-S. Shin, Z. Lee, B. H. Hong, and S. Cho, “Fast synthesis of high-performance graphene films by hydrogen-free rapid thermal chemical vapor deposition.,” *ACS Nano*, vol. 8, no. 1, pp. 950–6, Jan. 2014.

[128] S. Rahimi, L. Tao, S. F. Chowdhury, S. Park, A. Jouvray, S. Buttress, N. Rupesinghe, K. Teo, and D. Akinwande, “Toward 300 mm Wafer-Scalable High-Performance Polycrystalline Chemical Vapor Deposited Graphene Transistors.,” *ACS Nano*, vol. 8, no. 10, pp. 10471–9, Oct. 2014.

[129] Y. Wu, D. B. Farmer, W. Zhu, S.-J. Han, C. D. Dimitrakopoulos, A. A. Bol, P. Avouris, and Y.-M. Lin, “Three-terminal graphene negative differential resistance devices.,” *ACS Nano*, vol. 6, no. 3, pp. 2610–6, Mar. 2012.

[130] J. Moser, A. Barreiro, and A. Bachtold, “Current-induced cleaning of graphene,” *Appl. Phys. Lett.*, vol. 91, no. 16, p. 163513, Oct. 2007.

[131] J. Mateos, B. G. Vasallo, D. Pardo, T. Gonzalez, E. Pichonat, J.-S. Galloo, S. Bollaert, Y. Roelens, and A. Cappy, “Nonlinear Effects in T-Branch Junctions,” *IEEE Electron Device Lett.*, vol. 25, no. 5, pp. 235–237, May 2004.

[132] J. Mateos, B. G. Vasallo, D. Pardo, T. Gonzalez, J. Galloo, S. Bollaert, Y. Roelens, and A. Cappy, “Microscopic modeling of nonlinear transport in ballistic nanodevices,” *IEEE Trans. Electron Devices*, vol. 50, no. 9, pp. 1897–1905, Sep. 2003.

[133] L. Hiller and J. Pezoldt, “AlGaN/GaN Three-Terminal Junction Devices for Rectification and Transistor Applications on 3C-SiC/Si Pseudosubstrates,” *IEEE Trans. Electron Devices*, vol. 60, no. 10, pp. 3047–3052, Oct. 2013.

[134] B. Huard, N. Stander, J. Sulpizio, and D. Goldhaber-Gordon, “Evidence of the role of contacts on the observed electron-hole asymmetry in graphene,” *Phys. Rev. B*, vol. 78, no. 12, p. 121402, Sep. 2008.

[135] K. Nagashio and A. Toriumi, “Density-of-States Limited Contact Resistance in Graphene Field-Effect Transistors,” *Jpn. J. Appl. Phys.*, vol. 50, no. 7, p. 070108, Jul. 2011.

[136] X. Du, I. Skachko, A. Barker, and E. Y. Andrei, “Approaching ballistic transport in suspended graphene.,” *Nat. Nanotechnol.*, vol. 3, no. 8, pp. 491–5, Aug. 2008.

[137] J. B. Oostinga, H. B. Heersche, X. Liu, A. F. Morpurgo, and L. M. K. Vandersypen, “Gate-induced insulating state in bilayer graphene devices.,” *Nat. Mater.*, vol. 7, no. 2, pp. 151–7, Feb. 2008.

[138] P. A. Khomyakov, A. A. Starikov, G. Brocks, and P. J. Kelly, “Nonlinear screening of charges induced in graphene by metal contacts,” *Phys. Rev. B*, vol. 82, no. 11, p. 115437, Sep. 2010.

[139] R. Murali, “Impact of Size Effect on Graphene Nanoribbon Transport,” *IEEE Electron Device Lett.*, vol. 31, no. 3, pp. 237–239, Mar. 2010.

[140] M. Y. Han, J. C. Brant, and P. Kim, “Electron Transport in Disordered Graphene Nanoribbons,” *Phys. Rev. Lett.*, vol. 104, no. 5, p. 056801, Feb. 2010.

[141] I. Meric, C. R. Dean, A. F. Young, N. Baklitskaya, N. J. Tremblay, C. Nuckolls, P. Kim, and K. L. Shepard, “Channel length scaling in graphene field-effect transistors studied with pulsed current-voltage measurements.,” *Nano Lett.*, vol. 11, no. 3, pp. 1093–7, Mar. 2011.

[142] H.-Y. Chiu, V. Perebeinos, Y.-M. Lin, and P. Avouris, “Controllable p-n junction formation in monolayer graphene using electrostatic substrate engineering.,” *Nano Lett.*, vol. 10, no. 11, pp. 4634–9, Nov. 2010.

[143] P.-Y. Chen, H. Huang, D. Akinwande, and A. Alù, “Graphene-Based Plasmonic Platform for Reconfigurable Terahertz Nanodevices,” *ACS Photonics*, vol. 1, no. 8, pp. 647–654, Aug. 2014.

[144] I. Meric, M. Y. Han, A. F. Young, B. Ozyilmaz, P. Kim, and K. L. Shepard, “Current saturation in zero-bandgap, top-gated graphene field-effect transistors.,” *Nat. Nanotechnol.*, vol. 3, no. 11, pp. 654–9, Nov. 2008.

[145] J. Sanz-Robinson, W. Rieutort-Louis, Y. Hu, L. Huang, N. Verma, S. Wagner, and J. C. Sturm, “Hybrid Amorphous/Nanocrystalline Silicon Schottky Diodes for High Frequency Rectification,” *IEEE Electron Device Lett.*, vol. 35, no. 4, pp. 425–427, Apr. 2014.

Aalto-DD 108/2015

ISBN 978-952-60-6317-1 (printed)
ISBN 978-952-60-6318-8 (pdf)
ISSN-L 1799-4934
ISSN 1799-4934 (printed)
ISSN 1799-4942 (pdf)

Aalto University
School of Electrical Engineering
Department of Micro- and Nanosciences
www.aalto.fi

BUSINESS +
ECONOMY

ART +
DESIGN +
ARCHITECTURE

SCIENCE +
TECHNOLOGY

CROSSOVER

DOCTORAL
DISSERTATIONS